

https://dspace.org/

Transient separation of compressible flows over convex walls.

Muritala, Adam Olatunji

2011-09-27
http://hdl.handle.net/10539/10460

Downloaded from a DSpace repository. https://dspace.org/

1.0 INTRODUCTION

1.1 Background and Motivation

Compressible flow separation is a phenomenon whereby fluid of varying density is detached from the surface of a wall due to the presence of adverse pressure gradient in the direction of the flow. The motion of the fluid particles close to the wall is retarded by this unfavourable flow condition. The flow eventually breaks away from the wall surface when the pressure gradient is strong enough to bring the wall shear stress to zero. This phenomenon is very crucial in the analysis of compressible flows over solid bodies and is fundamental in the determination of the performance of aerodynamic flow devices.

Separation can be steady or unsteady, however, the main focus of this work is the unsteady flow separation behind a diffracting shock wave. Understanding of the unsteady flow separation plays a very important role in the analysis of both internal and external aerodynamics. This phenomenon is encountered in many engineering applications especially high speed flows such as supersonic jet engines, gas transmission lines, aircraft aerodynamics (e.g. airplanes, helicopters and rockets), automobile engine inlet, flow in the exhaust nozzle of internal combustion engines, flow around the blades of turbo machines, selection of optimum profile for missiles, etc.

High speed compressible flows are characterized by shock waves. They are mechanical waves of finite amplitude propagated by coalescence of several disturbance waves over a very short period of time. There is discontinuity in the flow parameters across a thin line formed by the shock. The thickness of this line is of order of magnitude of a few molecular mean free paths, about $10^{-7} m$ for air at ambient conditions [4]. The flow is susceptible to separation when the shock wave interacts with the boundary layer near the wall surface as explained by Delery [16], or if a moving shock encounters a convex corner. The flow behaviour after separation is critical to the analysis of the pressure loads on the structure.

When a planar shock wave is propagating through a channel of varying geometry, it will experience a series of disturbance waves. If this change in wall profile is such that the angle between the shock wave front and the interaction surface is greater than 90°, the disturbances generated by the surface will affect the general behaviour (strength, shape and orientation) of the shock as well as the flow induced by the shock; this process is known as shock wave diffraction [9].

Figure 1.1 is a schematic diagram of a diffraction process on a convex wall for upstream subsonic, sonic and supersonic flows as observed by Skews [58 - 60]. A normal shock wave that is moving from left to right on a surface becomes diffracted due to sudden change in the geometry of the wall. The flow expands around the corner which leads to increase in velocity as a result of sudden drop in pressure. The location of the head of the expansion wave depends on the condition of the flow behind the incident shock. The three possible flow conditions are illustrated in Figure 1.1 as A, B and C for subsonic, sonic and supersonic flows respectively.

The first attempt to explain the diffraction of a shock wave came from Friedlander [18] who conducted a study on the diffraction of sound pulses by a semi-infinite plane. The nature of this pulse is that of a classical blast wave with a leading shock front and exponential type decay. A good background to the present work is the classical works by Skews [58-60], and the recent works by Law et al. [33] and Berezkina et al. [12&13] on shock wave diffraction over planar and curved walls. These works revealed many important flow features that need to be explained. Some of these flow features are common to all geometry but differ in behaviour as illustrated in Figure 1.2 for curved walls (EW – Head of expansion wave, OS – Oblique shock, SL – Shear layer, SS – Second shock, RC – Recompression shock, CS – Contact surface, DS – Diffracted shock wave). The motion of the flow from left to right is induced by the shock that is moving through a stationary fluid. The diffraction of the shock commences from the start of the curvature generating an expansion fan bounded upstream by the head of an expansion wave. Other flow features are propagated as the diffraction process continued downstream.

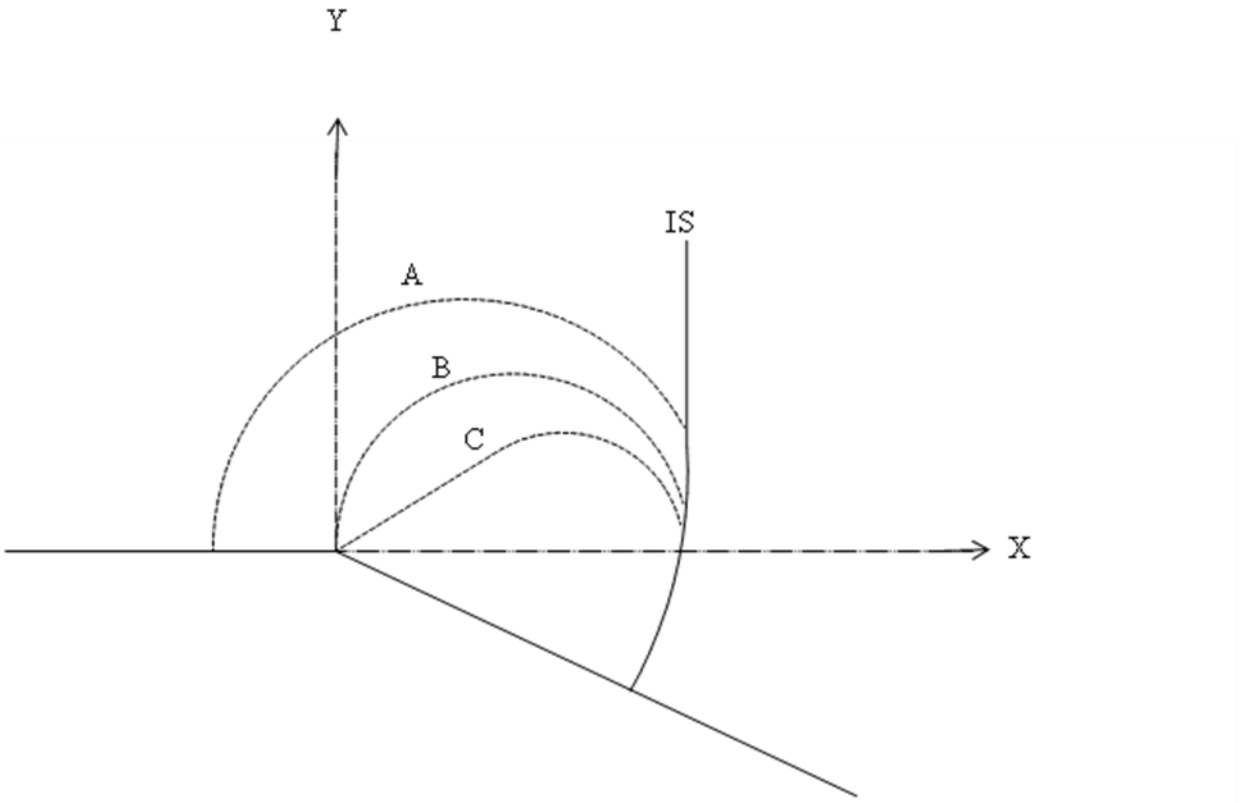

Figure 1.1: The characteristics of the flow behind the diffracting shock wave

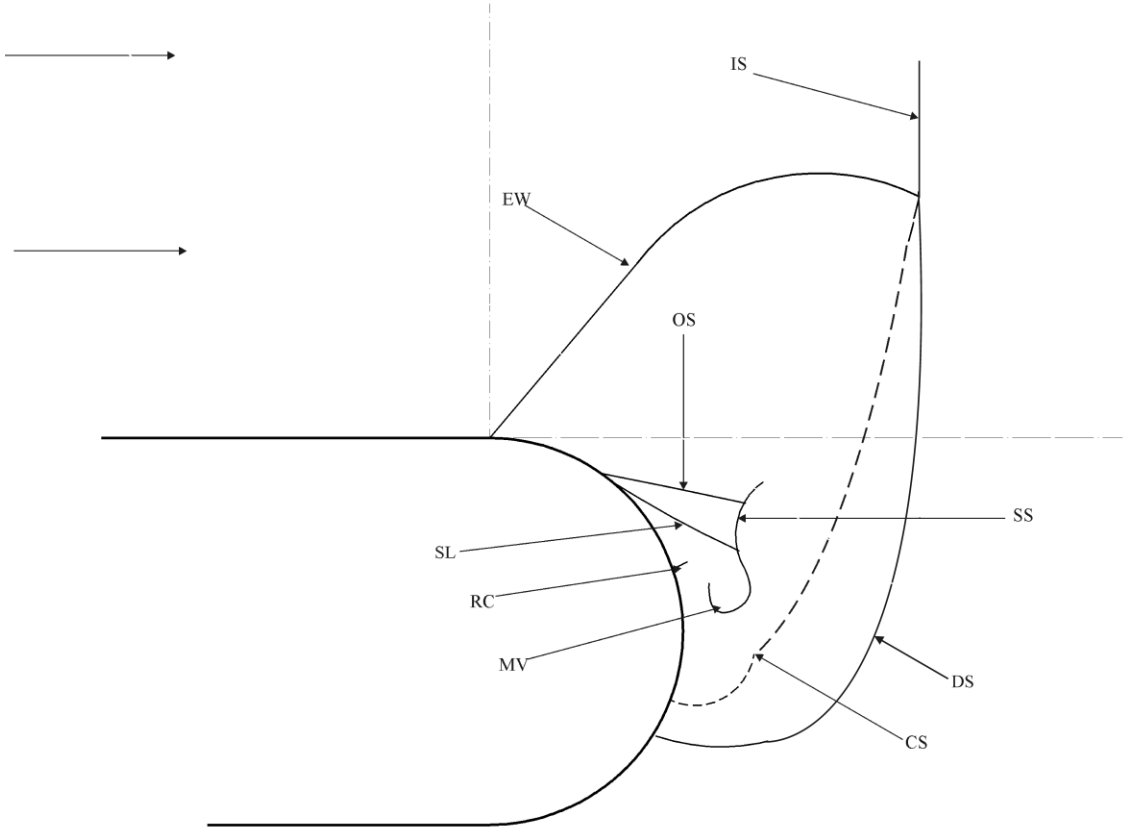

Figure 1.2: The flow features behind the diffracted shock wave on a curved wall [58]

The observations are explained as applied to this work as follows:

- Many discontinuities appeared behind the diffracted shock wave in the form of oblique shock, shear layer, second shock, and recompression shock.
- The shear layer which is defined as a line of finite discontinuity of temperature and velocity [13] evolved from the separation point and extends downstream with further diffraction of the incident shock wave.
- The position of the separation point changes as the diffraction process progresses downstream.
- For multifaceted walls the expansion generated at each corner has a significant effect on the separation shear layer formed after the corner.
- The flow behind the diffracted shock wave is complex and highly unsteady.

The analysis of the complex flow structure behind the diffracted shock wave requires a highly robust CFD (Computational Fluid Dynamics) code with optimum resolution for accurate capturing of the flow features of interest. Takayama and Inoue [63] proposed that the diffraction of a Mach 1.5 incident shock wave around a 90° convex corner be made a benchmark to measure the performance of CFD codes.

The comprehensive explanation of the complex flow structure within the perturbed region behind a diffracted shock wave is the main objective of this research. The investigation is accomplished through large scale experimentation which is complemented by numerical computations. The data obtained from the experiments combined with the numerical results are expected to give the detailed global flow behaviour behind the diffracted shock wave.

1.2 Review of Applicable Theories

Compressible flows are characterized by change in density with pressure. The extent to which the density of a fluid can change is determined by compressibility which is a property of the fluid. Detailed explanation of the theory of compressible flows is given in numerous books of gasdynamics such as Anderson [3&4] which gives some background

to this work. An important dimensionless parameter in compressible flows is the Mach number M , which is the ratio of flow velocity to local speed of sound. This is defined by Equation (1).

$$M = \frac{v}{a} \tag{1}$$

where v is the flow velocity and a is the local speed of sound.

Compressible flow can be subsonic (M < 1), transonic (0.8 < M < 1.0), sonic (M = 1), and supersonic (M > 1) as applicable to this work. At higher Mach numbers the flow deviates greatly from the ideal flow assumption that will be discussed in the later section.

1.2.1 Properties of gas

A gas is an agglomeration of numerous particles in random motion bounded together by weak intermolecular forces [4]. The internal energy of a gas is the sum of the following sources of energy: kinetic energy of individual particle, the rotational energy of the atoms, the energy enhanced by vibration of molecules and electronic energy from electrons revolving round the nucleus. For compressible flows in which pressures and temperatures are moderate, the gas is assumed to be calorically perfect. Numerous works are available in the literatures that analyzed compressible flow based on this assumption, and modifications necessary are incorporated at relatively high temperature.

The ideal perfect gas model defined by equation (2) is used for all the analysis in this work because the gas temperature is within the acceptable range.

$$P = \rho RT \tag{2}$$

where P is the pressure, ρ is the density of the gas, R is the gas constant for air and T is the temperature. White [66] has shown that for weak shock waves at ambient pressure and temperature any test gas can be assumed to be a perfect gas even with viscous effects taking into account.

1.2.2 Normal shock wave

A shock wave moving in a direction perpendicular to the direction of the flow is called a normal shock wave or conversely, when a flow is moving in a direction normal to a

stationary shock wave as illustrated in Figure 1.3. A moving normal shock wave propagating into a stationary medium is considered in this work. The gas ahead of the shock is stationary while the gas behind the shock is in motion, both referenced to the laboratory frame.

The flow at the two sides of the normal shock wave is described by conservation principles (continuity, momentum and energy equations) defined by equations (3 - 5). Assume adiabatic flow condition, and let A represents a point at the left hand side of the shock which is the region of a moving gas while B is the region of a stationary gas as shown in Figure 1.3.

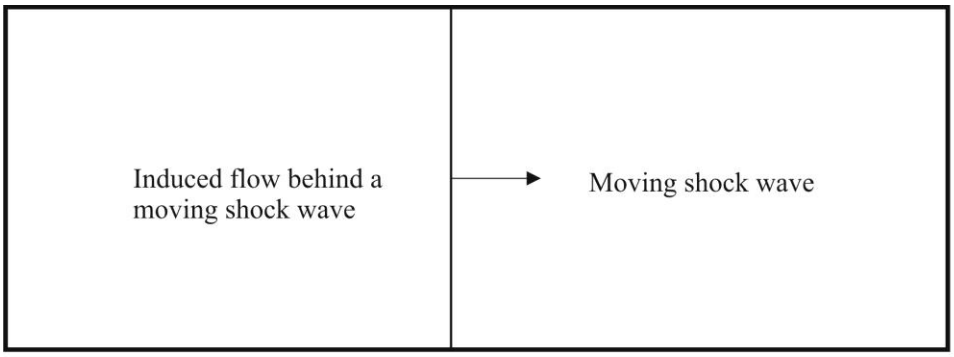

(a) A moving shock wave

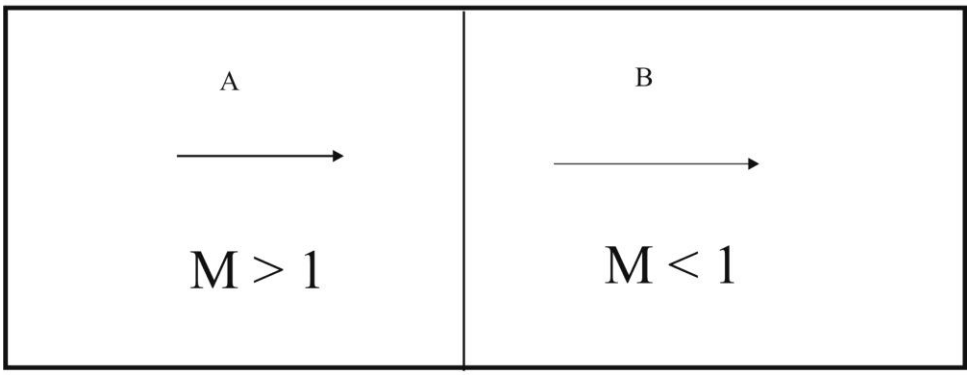

(b) A stationary shock wave

Figure 1.3: Flow around a normal (moving and stationary) shock wave

The continuity, momentum and energy equation across the shock are given as:

$$\rho_A U_A = \rho_B U_B \tag{3}$$

$$P_A + \rho_A U_A{}^2 = P_B + \rho_B U_B{}^2 \tag{4}$$

$$H_A + \frac{1}{2} U_A{}^2 = H_B + \frac{1}{2} U_B{}^2 \tag{5}$$

where ρ, U, P and H represent density, velocity, pressure and enthalpy respectively. These equations are applicable to both calorically and thermally perfect gases as well as chemically reacting flows [3].

If the velocities at both sides of the shock are eliminated in equations (3 - 5), the three equations reduce to a single equation that relates only state variables. When change in flow properties across the shock is expressed in terms of internal energy e, density ρ and pressure p, the equation across the shock wave becomes Rankine - Hugoniot equation (equation 6) which relates only thermodynamic properties. It is valid for perfect gas, real gas and chemically reacting flows [3&4].

$$e_B - e_A = \frac{1}{2}(P_A + P_B)(\frac{1}{\rho_A} - \frac{1}{\rho_B}) \tag{6}$$

When various thermodynamic relations are introduced, the relationship between the Mach numbers of the flow at the two sides of the shock is established for calorically perfect gas as stated in equation (7).

$$M_B = \frac{1 + \frac{\gamma - 1}{2} M_A{}^2}{\gamma M_A{}^2 - \frac{\gamma - 1}{2}} \tag{7}$$

where γ (ratio of specific heats) is constant, M_A is the upstream flow Mach number which is the major determinant of the properties of the shock wave and M_b is the downstream flow Mach number referenced to the stationary shock.

Other flow variables are related at both sides of the shock wave as shown in equations (8a – 8c) [3].

$$\frac{P_B}{P_A} = \frac{2\gamma M_A^{\ 2} - (\gamma - 1)}{\gamma + 1} \tag{8a}$$

$$\frac{T_B}{T_A} = \frac{[2\gamma M_A^{\ 2} - (\gamma - 1)][(\gamma - 1)M_A^{\ 2} + 2]}{(\gamma - 1)^2 M_A^{\ 2}} \tag{8b}$$

$$\frac{\rho_B}{\rho_A} = \frac{(\gamma + 1)M_A^{\ 2}}{(\gamma - 1)M_A^{\ 2} + 2} \tag{8c}$$

For a moving shock wave the major parameter that governs changes across the shock is pressure ratio defined by P_B/P_A. The strength of the shock (M_s) is given by equation (9)

$$M_s = \left(\frac{\gamma + 1}{2\gamma}\left(\frac{P_B}{P_A} - 1\right) + 1\right)^{1/2} \tag{9}$$

For an isentropic process the ratio of total to static pressure/temperature at a point in a flow as a function of the flow Mach number at that point is given by equations (10a&b) respectively.

$$\frac{P_0}{P} = \left(1 + \frac{\gamma + 1}{2} M^2\right)^{\gamma/\gamma - 1} \tag{10a}$$

$$\frac{T_0}{T} = \left(1 + \frac{\gamma - 1}{2} M^2\right) \tag{10b}$$

A uniform supersonic flow that moves over a wedge of angle θ will generate an oblique shock wave that will deflect the flow streamlines parallel to the wall surface downstream. The Mach number of the flow will decrease across the shock while density, pressure and temperature will increase. In contrast to oblique shock, a supersonic flow that encounters a convex wall will turn away from its original direction through an expansion wave. The flow streamlines will bend smoothly across the expansion fan and become parallel to the wall surface as shown in Figure 1.4.

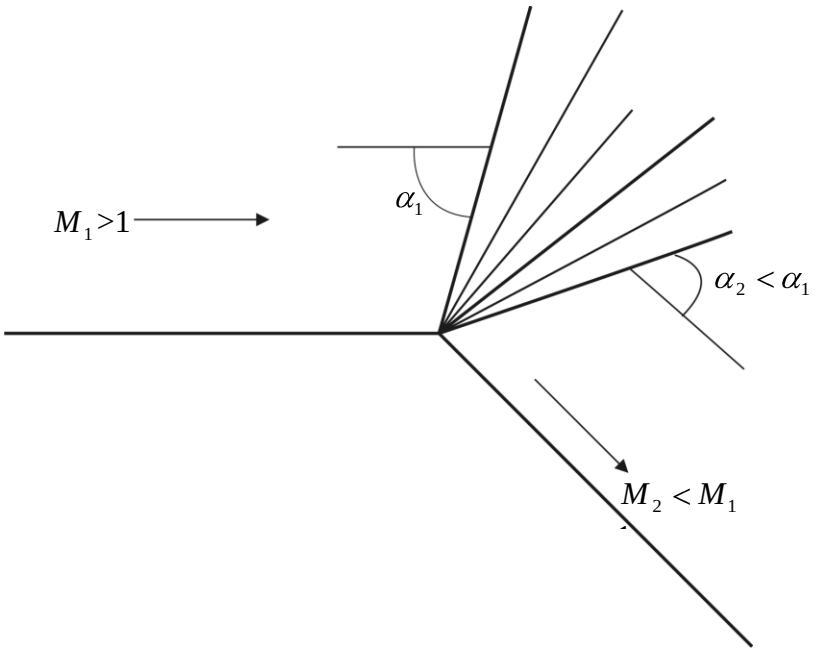

Figure 1.4: **Prandtl – Meyer expansion wave [3]**

A very good way of increasing the Mach number of a flow is to allow the flow to pass through a convex geometry that generates expansion waves. The flow velocity across these waves will increase with decrease in pressure, density and temperature. A common theory for the steady supersonic flow around a convex corner is illustrated in Figure 1.4. Further work by Ruba [53] described the whole process by a self similar solution of the Karman-Guderley equation whose analytical solution is applicable to perfect gas, real gas and chemically reacting flow.

1.2.3 Shock wave reflection

The refection of a shock wave occurs when an incident oblique shock wave impinges on a solid wall at an angle. The reflection may be regular or irregular depending on the oblique angle and the strength of the incident shock wave [10]. A regular reflection is made up of the incident and reflected shock both emanated from a point on the rigid surface as shown in Figure 1.5.

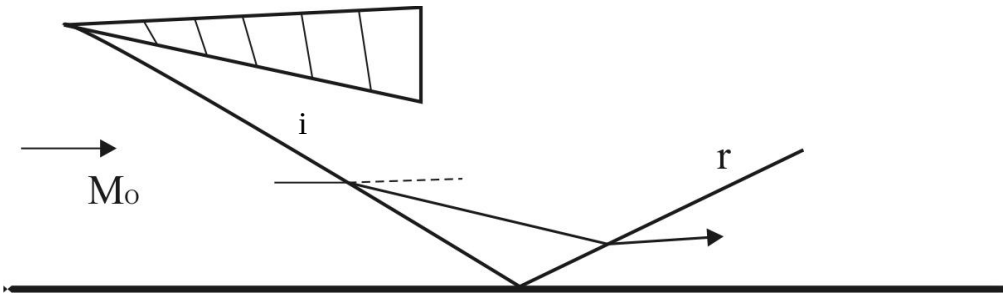

Figure 1.5: **Regular reflection from a rigid surface [10]**

Irregular reflection consists of the incident and the reflected shocks moving away from the reflecting surface. A Mach stem links the triple point of the three shock configuration with the reflecting surface as shown in Figure 1.6. This type of reflection is called "Mach reflection" named after Ernst' Mach, who first discovered this non-linear gasdynamic phenomenon in 1878 when investigating the reflection of strong shock waves.

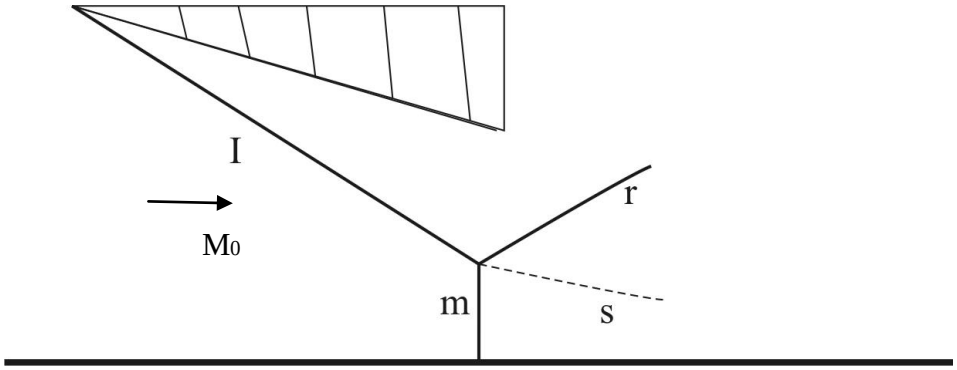

Figure 1.6: Irregular reflection from a rigid surface [10]

Irregular reflection can be further divided into Mach reflection and von-Neumann reflection [25]. The von-Neuman reflection was observed during the analysis of shock reflections that occur when the shock is sufficiently weak and the wedge angle is small [2 &41]. Barbosa and Skews [8] confirmed the von-Neuman theory of shock wave reflection transition experimentally. Other relevant works on weak shock wave reflections are reported by Ben-Dor et al. [9], Richard and Allen [51], Kobayashi et al.[29], and Sasoh et al. [54]. Analytical investigation of reflected–diffracted shock waves has been carried out by many authors such as Zakharian et al. [71], Lighthill [38], Ben–

Dor et al. [11], and Li et al. [36]. The results were in good agreement with the earlier experimental and analytical works.

The role of viscosity on weak shock wave reflection cannot be neglected as was earlier observed by Ivanov et al. [24]. It was confirmed that viscosity plays a crucial role in the vicinity of the triple point. A slip stream is formed from the intersection of the three shocks. This was motivated by entropy inequality that resulted from difference in velocity between the flows across the incident shock/Mach stem and the flow across the reflected shock wave.

1.2.4 Shock wave diffraction

Shock wave diffraction is a process in which the shape, the strength and the orientation of a planar shock changes with time as a result of the disturbances propagated from a change in wall geometry. Chester, Chisnell and Whitham have established a relationship in two dimensions between the strength of the shock and the shape of the surface on which the shock is moving [9&20]. The original incident shock is divided into three parts: undiffracted part, the diffracted part and the wall shock. Earlier work by Skews [58&60] identified these shocks and the shape of the diffracted shock was described with reference to the nature of the convex walls.

The diffraction of a shock over a convex wall is an unsteady process and the flow region adjacent to the diffracting shock undergoes a non-uniform compression which eventually generate adverse pressure gradient along the wall surface. Further work by Skews [58] identified the flow features within the perturbed region behind the diffracted shock wave especially with regard to the separation phenomenon. Other relevant works on shock wave diffraction includes Onodera [45], Klein [26], Takayama and Inoue [63], and Berezkina et al. [12], however, the experimental analysis was limited by the scale of the experimental facility.

1.2.5 Theory of the shock tube

A shock tube is a high speed gasdynamic experimental tube used for generating shock waves and gas with particular flow conditions over a very short time duration. The first known shock tube was used in France by Vieille in 1899; the diameter and the length of this tube was 22mm and 6m respectively. The tube became a high speed flow research facility around 1940 after Payman and Shepherd used it in their "bursting - diaphragm apparatus" [57].

Consider a long tube closed at both ends divided into two regions of high and low pressure by a diaphragm of a known property as shown in Figure 1.7a. By rapidly bursting the diaphragm a compressive wave is propagated towards the low pressure region while an expansion wave is propagated in the opposite direction as shown Figure 1.7b. The general design of the tube is a function of the intended application. The tube is usually long to allow for proper propagation of the shock before getting to the region where the interaction will be observed. The length of the driver section is chosen such that the reflected expansion wave does not catch up with the shock. The wall of the tube is usually designed to withstand the required high pressure in the compression chamber. The tube is aligned along a straight line to avoid distortion of the shock and the inner surface of the tube is hydraulically smooth to avoid shock attenuation.

Shock tubes are widely used to study the physical and chemical processes over a large range of flow conditions [46]. A comprehensive study of an open ended shock tube flows with a particular emphasis on the effect of pressure ratio and diaphragm position was carried out by Haselbacher et al. [19]. It was observed that if the pressure ratio is large enough to generate supersonic flow behind the slip surface, the flow at the open end relaxes from the initial conditions behind the contact surface to sonic conditions once the tail of the expansion fan arrives at the open end.

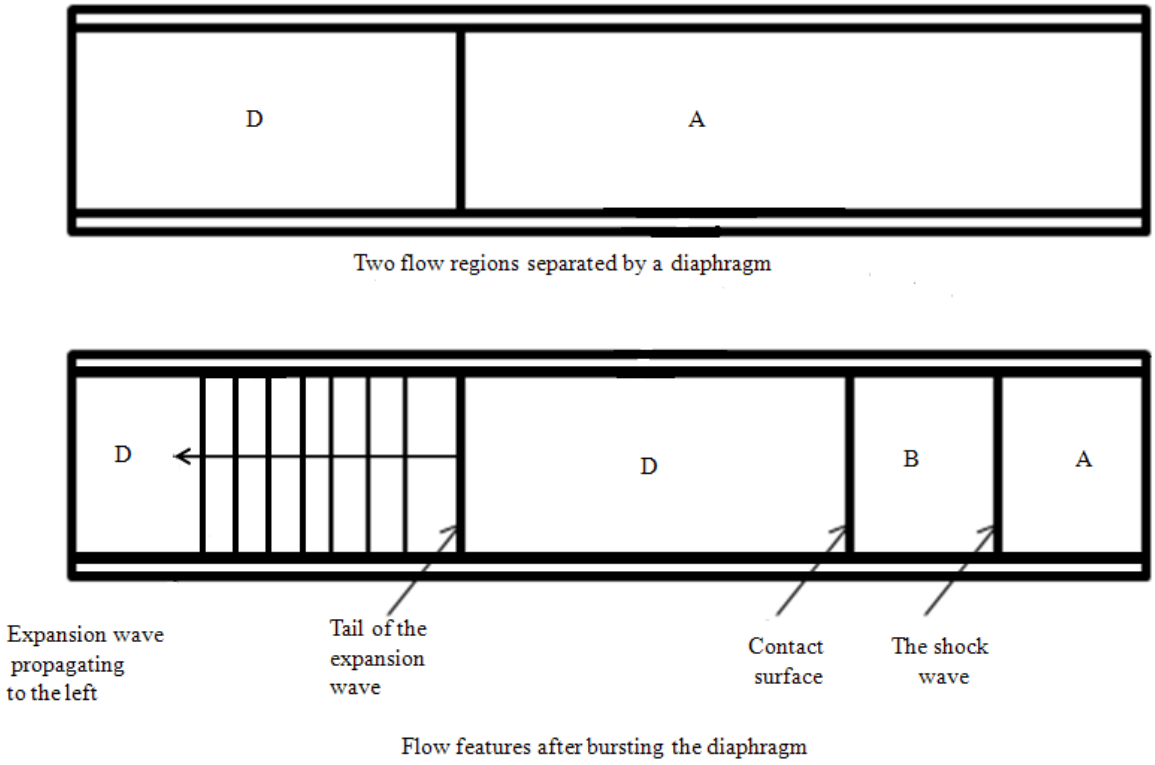

Figure 1.7: Schematic diagram of a shock tube [3]

Other types of shock tube that have been developed include diaphragmless shock tubes that make use of a piston instead of the conventional diaphragm rupture system. This is a very good tool used in gasdynamic laser experiments [50] & [35]. Other applications of shock tubes include generation of high energy beam in a range of 1 – 5 eV [44] and impact testing facility as a special wave generator to achieve high velocity, high temperature and high energy testing conditions [37]. Shock tubes have also been designed such that many functions can be carried out interchangeably in the same shock tube. A good example is a free piston compressor, shock tube, shock tunnel and gun tunnel that was designed for different applications [1]

Recent developments in the aerospace technology have called for large scale experimental investigation of supersonic and hypersonic flows. The conventional shock tubes of lower aspect ratio could not accurately predict some flow behaviour that involves shock wave especially on complex walls. Hence the development of large aspect ratio shock tubes like the one used for this research.

When the shock wave is to be propagated in the shock tube, the diaphragm is removed during very short time duration. The shock is formed from the coalescing of compression waves and the position of the shock changes with time as shown in Figure 1.8. The flow behind the shock is induced and there is a mass motion of the high pressure gas to low pressure gas.

All properties of the flow field behind the shock change with respect to distance and time after the removal of the diaphragm. This implies that the flow variables are functions of space and time ($\rho = \rho(x,t), T = T(x,t), P = P(x,t)$ and $U = U(x,t)$). Hence, the flow in the shock tube is purely unsteady. The expansion fan moves backward in the shock tube and is reflected at the closed end of the tube as shown in Figure 1.8. The reflected expansion fan travels at a high speed behind the contact surface and may eventually catch up with it. The driver section is usually designed to be long so that there will be enough distance between the shock and the reflected expansion wave.

The interface between the two gases is called the contact surface which travels at the same speed with the fluid behind the shock. Across the contact surface fluid pressure is the same, but there is a discontinuous change in entropy which results in density and temperature gradient. Experimental test time can be extended by tailoring the interface between the driver and the driven gases as studied by Anthony et al. [5] and Zekai et al. [72]. Their study shows that tailoring of contact surface delays interaction of the reflected expansion wave with the flow adjacent to the shock wave.

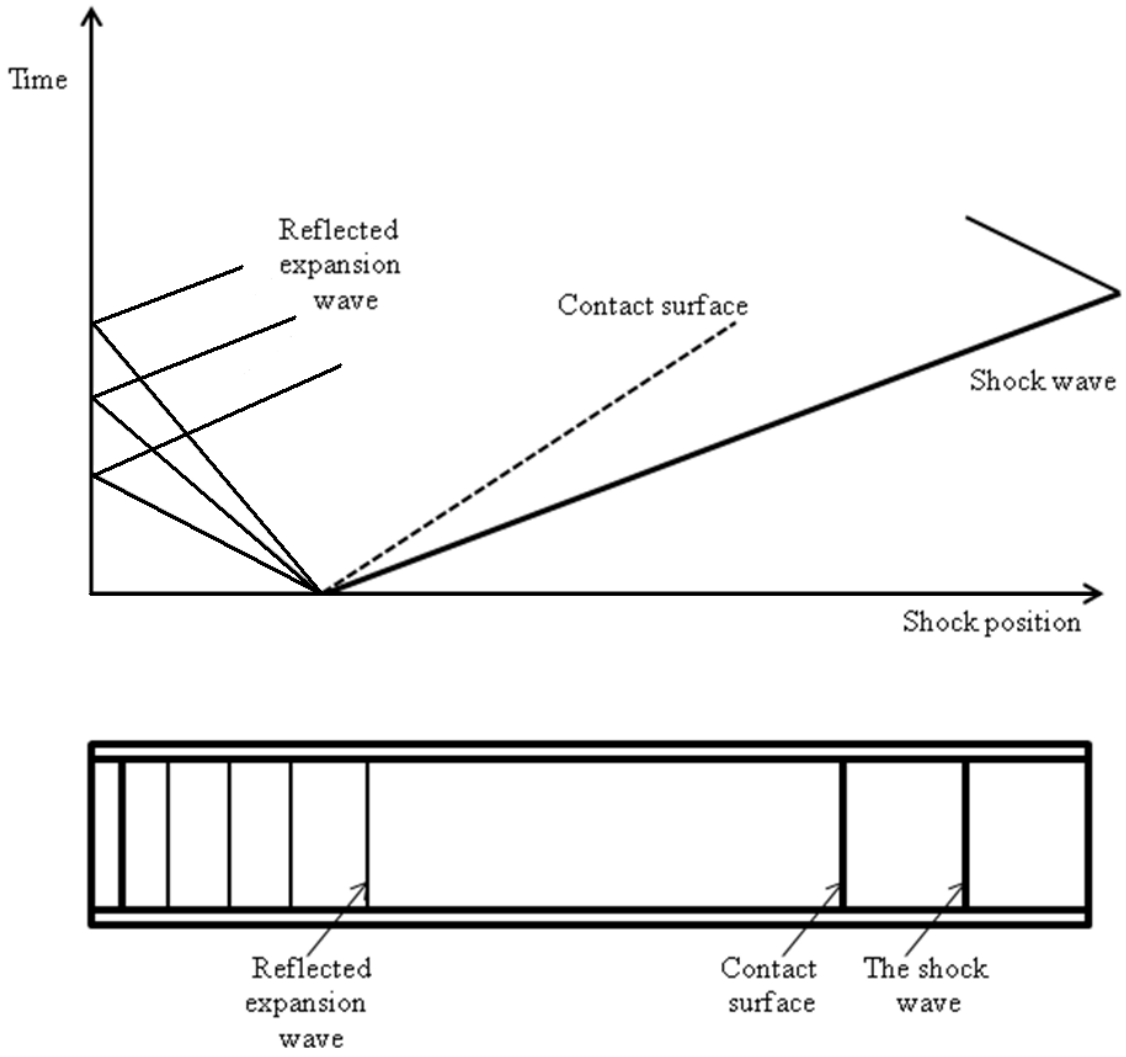

Figure 1.8: Propagation of shock wave and expansion fan in the shock tube [64]

1.4 Thesis Structure

The thesis consists of seven chapters, each of which is divided into sections and subsections to give the detailed description of the subject and for easy reading and referencing. There are four appendices which contain drawings, tables, graphs and pictures that are not very important to appear in the main report. However, these appendices are available to give detailed information about any particular subject discussed in the thesis.

Chapter one is the introduction which contains motivation and background followed by theory of compressible flows that are applicable in this work. Chapter two reviews the past work on the subject with critique in analytical, numerical and experimental works in order to identify the knowledge gap to be filled. This also helps to determine suitable methodologies to be used in capturing the flow behaviour. The later part of the chapter itemized the objectives of the study so as to clearly define the pertinent questions to be answered with regard to transient compressible flow separation on convex walls.

Chapter three focuses on the methodology used for the investigation. The numerical model employed for the analysis is explained with the computational domain used for the simulations. The large scale experimental facility is described using relevant pictures followed by layout of the apparatus with required instrumentation. The principle of operation and set-up of the schlieren visualization technique is explained. This is to draw attention to its suitability in capturing the interactions at the test area.

The analyses of the results of low incident shock Mach numbers are discussed in chapter four with a view to validate the numerical results and justify the numerical method. Chapter five gives the analysis of high Mach numbers simulation results while chapter six focuses on the discussion of various findings with reference to the theoretical work. This provides comprehensive information that enhances the proper understanding of compressible flow separation. The last chapter is devoted to conclusion and recommendation in order to expound on the need for further work in various areas that could not be covered by this work.

2.0 LITERATURE REVIEW

2.1 Introduction

The major breakthrough in explaining causes and mechanism of separation phenomenon was made by Prandtl [49] who developed the theory of boundary layers. However, the occurrence of separation in shock wave diffraction is mainly dominated by pressure rather than viscous eefects suggests that separation phenomenon is not exclusively dependent on viscosity. Prandtl's theory was based on a steady two-dimensional incompressible flow with a no slip boundary condition [55 & 31]. In this theory the flow domain around a solid body is divided into two regions; the inviscid region and a thin region called laminar boundary layer, within which the viscous effect is significant.

The drag force within the thin region around a body moving in a fluid is called skin friction drag and the flow will separate if there is a strong adverse pressure gradient to overcome this viscous force [23, 31 & 42]. Separation is usually accompanied by large energy loss due to the formation of eddies. The pressure distribution deviates greatly from the potential flow and the drag force on the surface becomes form drag. The boundary layer theory indicates separation point based on the zero skin friction but it was later noted by Sears and Tellionis [56] that point of singularities in the boundary layer equations should be used to analyze separation. However, the available numerical solution of the boundary layer equations did not show any singularity.

Two types of separation have been identified by Peacock et al. [48], there is a fixed separation in which the separation point is located at a point, and a moving separation which is time dependent. The former is a common phenomenon in incompressible flow separation while the latter is usually encountered in shock wave diffraction. When a shock diffracts over a surface the gas particles behind the shock is unevenly compressed due to unsteadiness in the process of diffraction. Different flow regimes are formed behind the diffracting shock with low pressure gas across the expansion fan. An adverse

pressure gradient is developed near the surface of the wall as the diffraction process continues.

2.2 The Perturbed Region behind a Diffracted Shock Wave

The development of a strong adverse pressure gradient behind a diffracting shock wave resulted in the local perturbation of the flow region behind the shock. This occurrence led to the formation of many flow features that develop with time. Classical works by Skews [58&60] have identified some of these flow features while investigating the diffraction of shock wave on plane walls. A series of experiments were carried out in a conventional shock tube and the observations made on the perturbed region behind the diffracted shock wave are summarized as follows:

(a) The process of shock wave diffraction was observed to be self similar for plane walls.

(b)The expansion fan behind the diffracting shock is centered for the plane walls.

(c) For the incident shock Mach numbers considered, the flow behind the diffracted shock wave separated from the walls on corner angle as low as15°.

(d) The flow behind the diffracted shock wave on a 90° wall is subsonic for incident shock Mach numbers Ms < 1.35 and supersonic for Ms > 2.0.

(e) The flow features after separation consist of a smooth shear layer that originated from the corner and extended downstream. The shear layer is terminated by a vortex which under certain condition embedded a shock described as a secondary shock.

(f) The position of the slipstream, the terminator, the contact surface and the second shock are independent of corner angle for angles greater than 75°.

The results of the further work by Skews [59] and Law et al. [32] revealed the difference between the flow behaviour behind a diffracted shock wave on plane and curved walls. The flow behaviour was self similar on plane walls while the radius of curvature and viscosity affect the flow features on curved walls. The expansion fan is not centered as earlier observed for plane walls and it was bounded downstream by a terminator.

Figure 2.1 shows the coincidence in the point of emanation of both slipstream and the oblique shock. As illustrated in the figure, the slipstream did not emanate tangentially

from the wall surface. It extended smoothly and terminated with a vortex that increases in size as the diffraction process progresses downstream. The nature of the flow within the region behind the diffracting shock is determined by the incident shock wave. Law et al. [32] observed that when the Mach number of the incident shock is less than 1.5, the Mach number of the flow behind the diffracting shock will be less than 0.6.

At higher incident shock Mach numbers the velocity of the flow behind the shock becomes high. The diffraction of the shock is accompanied by the formation of different flow regions which is motivated by non–uniform compression of the gas adjacent the diffracting shock. A weak shock wave is propagated between the upstream low pressure flow and high pressure gas downstream. This shock changes to an oblique shock due to the influence of the near wall adverse pressure gradient.

Separation occurred at a point where the oblique shock is formed on the wall followed by the evolution of the shear layer. The oblique shock is terminated by the upper portion of a second shock as illustrated in Figure 2.1 and 2.2 (FD-Flow direction, EW-Expansion wave, SL-Shear layer, OS-Oblique shock, RS-Recompression shock, SS-Second shock, DS-Diffracting shock, MV-Main vortex and CS-Contact surface).

A second shock is propagated as a result of supersonic flow along the shear layer as earlier explained by Skews [58]. This shock matched the expanded flow that is exiting the oblique shock with the compressed gas behind the diffracting shock. There is a contact surface that has its top touching the point of contact between the diffracted shock and the original incident shock. The lower part is directed to the wall and touches the wall in front of the vortex.

The near wall features in transient compressible flow on convex walls was investigated by Law et al. [32]. The viscous effect was observed to have a significant influence on the temporal development of the flow especially for wall turning angles between 10° to 50°. Hence, the self similarity that is usually assumed in the analysis of the diffraction of shock wave on plane walls cannot be generalised.

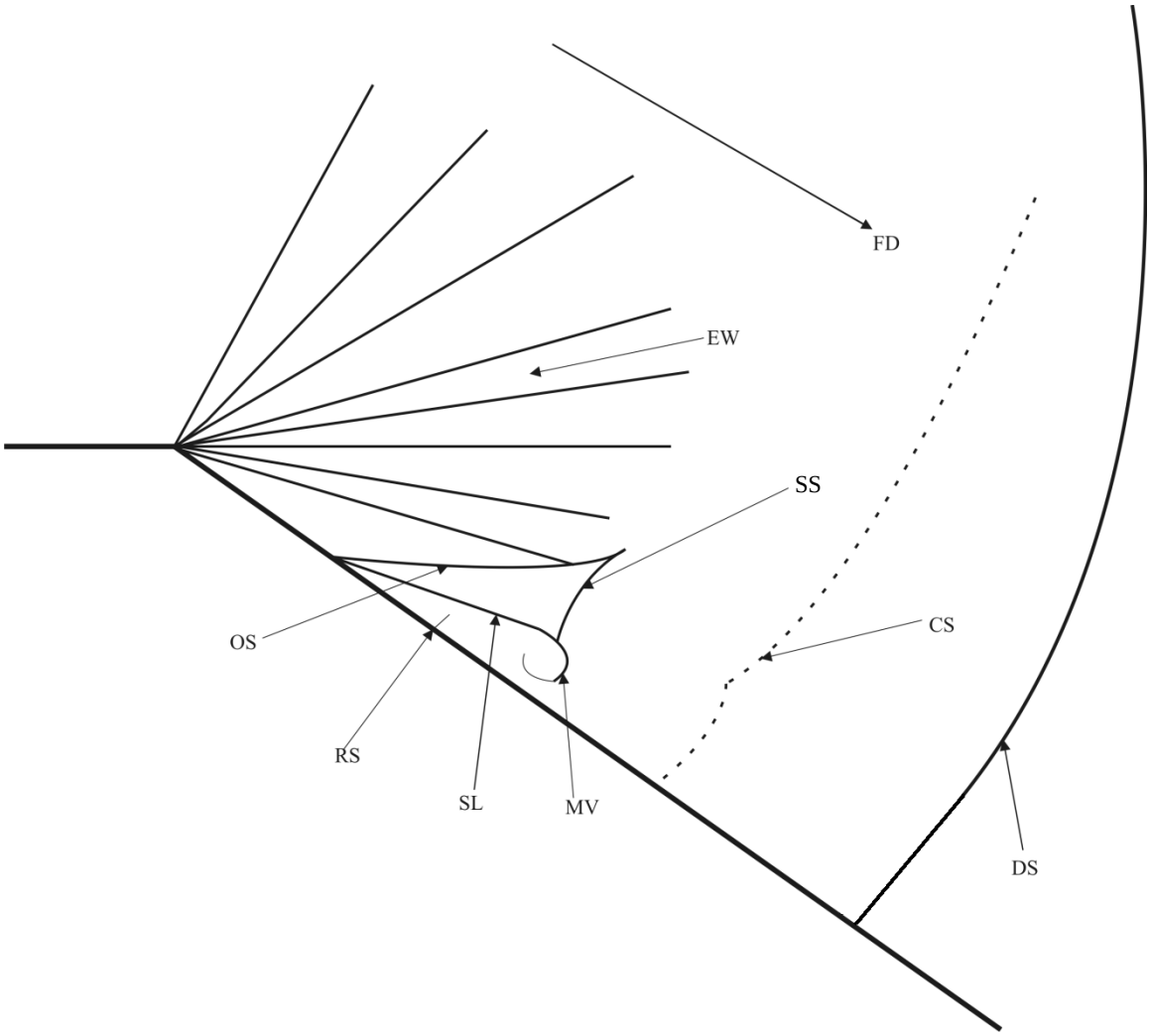

Figure 2.1: A schematic diagram of a complex flow structure on a 30° wall

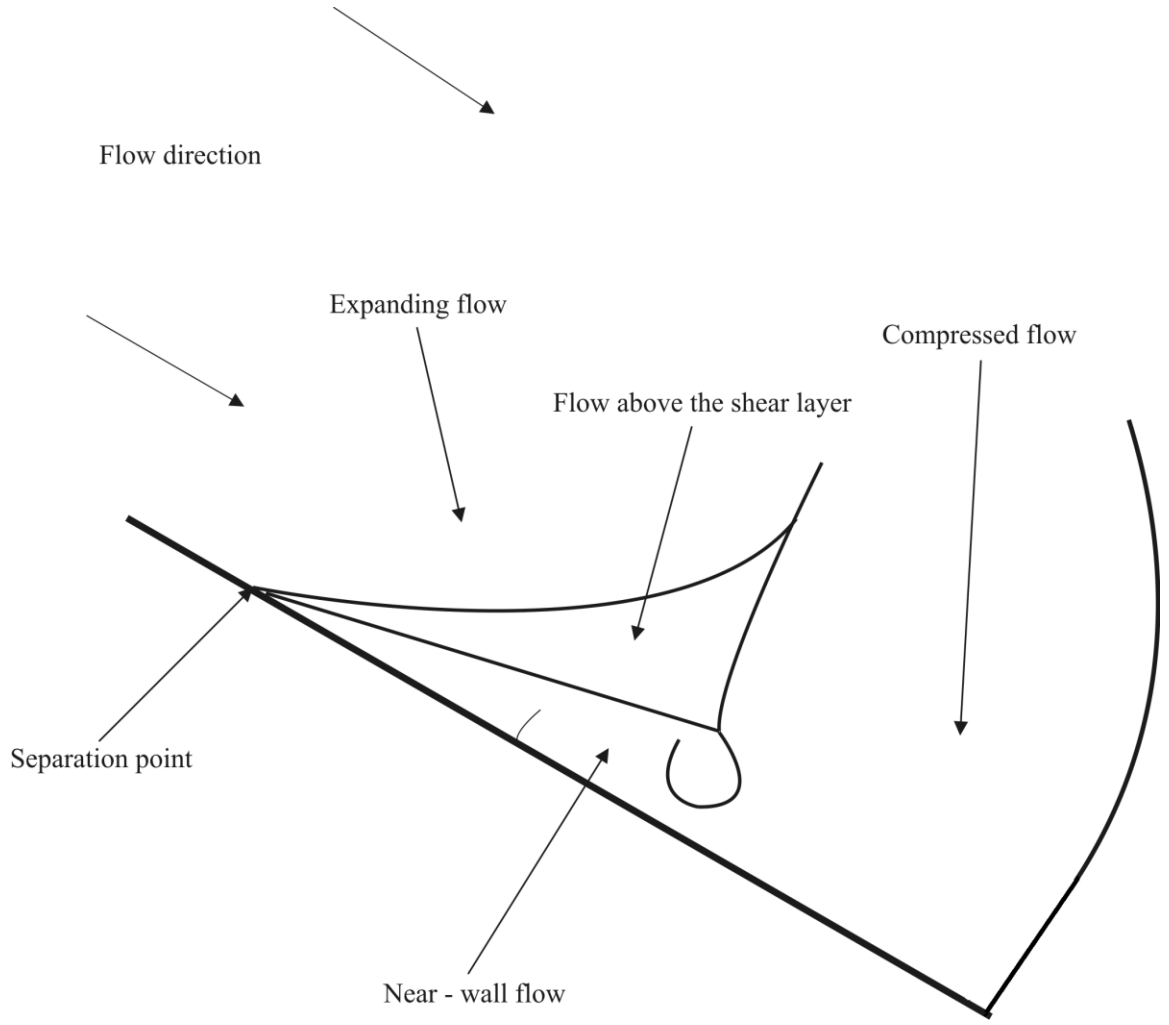

Figure 2.2: The flow behaviour downstream of the corner

Skews[59] used Whitham's method to predict the shape of the shock for both plane and curved walls at different incident shock Mach numbers. The results of this theoretical prediction were in good agreement with the experimental measurements, for convex walls consisting of a number of facets and circular arcs. The temporal changing of the shape of the shock downstream of the convex corner creates unequal compression of the gas behind the diffracting shock. This enhances the complex flow structure upstream as shown in Figures 2.3 and 2.4 (IS – Incident shock, EW - Expansion wave, SL - Shear layer, OS - Oblique shock, RS - Recompression shock, SS - Second shock, DS - Diffracting shock, MV - Main vortex and CS - Contact surface).

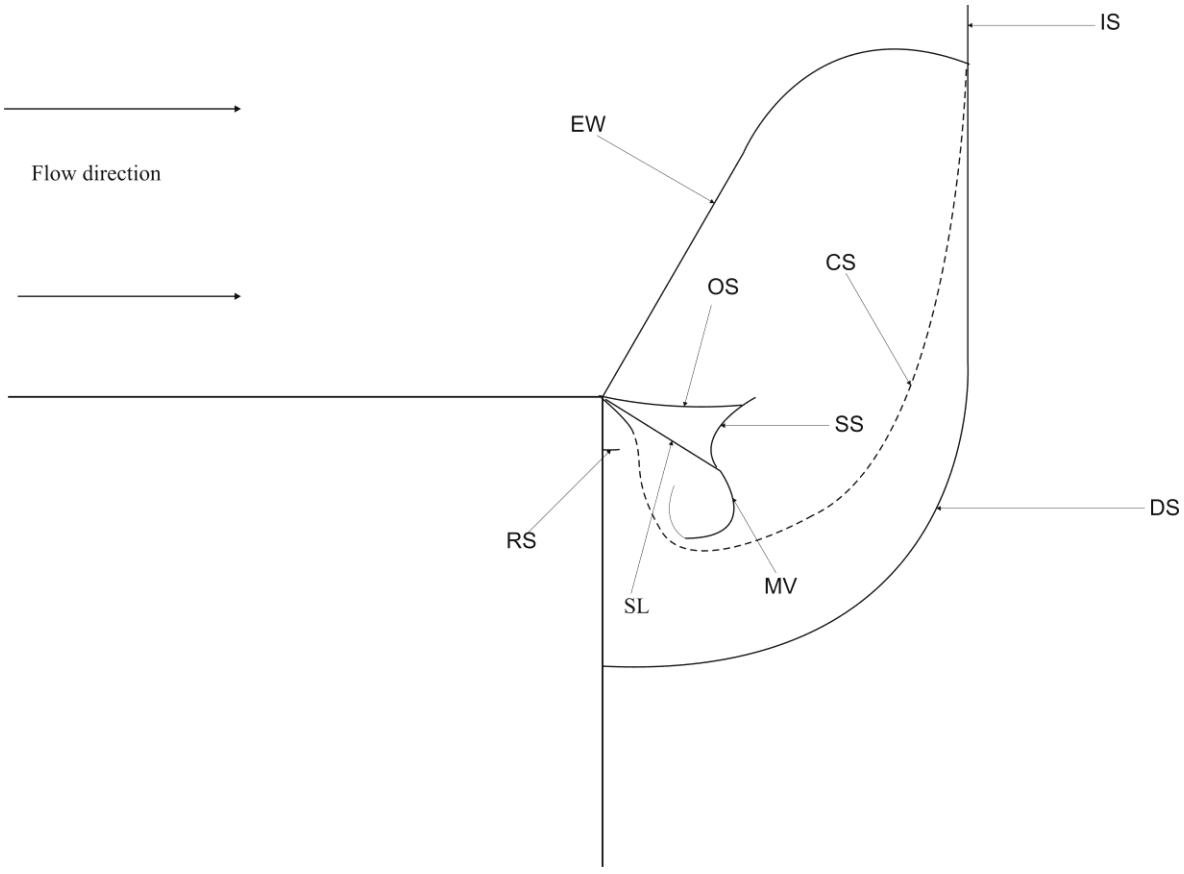

Figure 2.3: The complex flow region behind a diffracted shock on a 90° wall

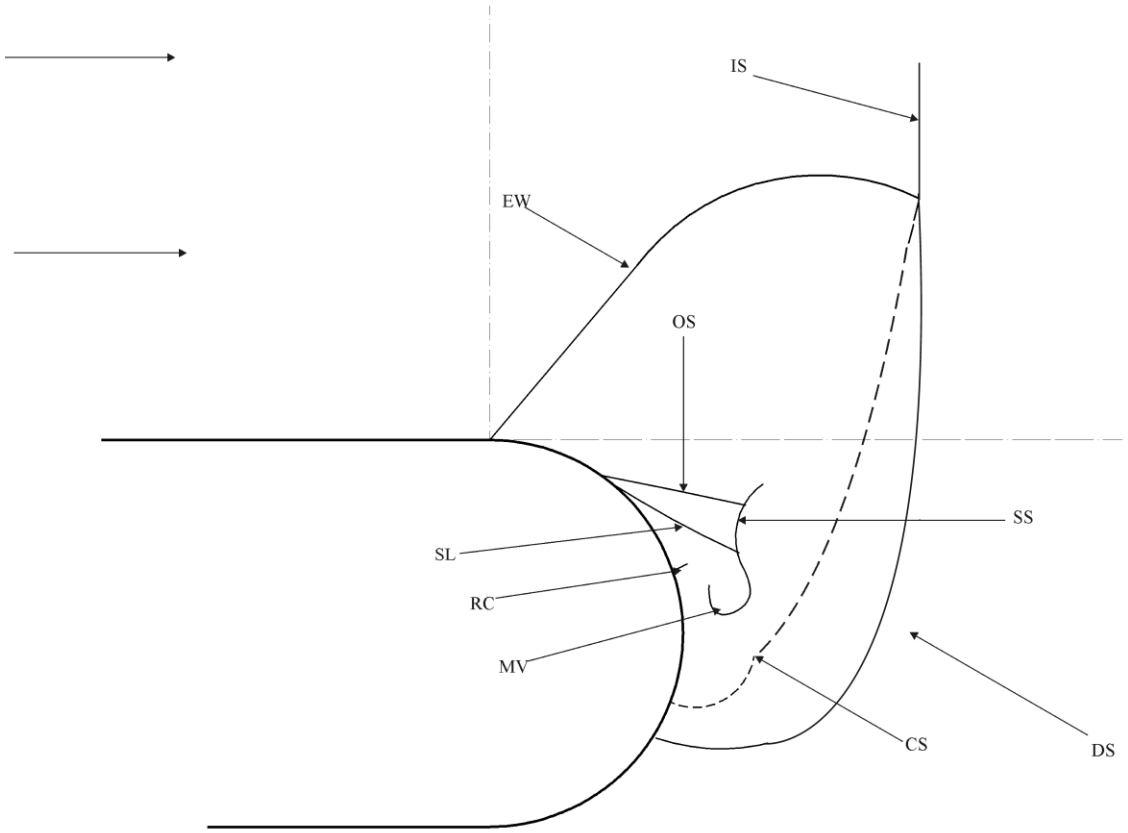

Figure 2.4: The complex flow behind a diffracted shock wave on a curved wall

The main flow features within the complex flow region shown in Figure 2.4 correspond to what have been observed for plane walls by Skews [59] and Law et al. [32]. However, the separation point moves along the arc and at higher Mach number there is a supersonic flow directed along the shear layer. The formation of the second shock is attributed to the supersonic flow along the shear layer as earlier explained on plane walls.

Skews [59] observed that the flow behind a diffracting shock of incident Mach number 1.5 on 68mm diameter wall did not separate. The boundary layer along the wall became thick especially at higher value of $\alpha M / r$ (M – Mach number, r – radius and α – a parameter to define incident shock displacement) which is the parameter that determines the position of the diffracting shock. The results also suggested possible separation of the flow at higher values of $\alpha M / r$. However, the conventional shock tube used for the experiments could not accommodate higher values of this influencing parameter.

Another important flow feature observed by Skews [59] is the behaviour of the contact surface. The lower part of the contact surface instead of being rolled up between the wall and the vortex as observed for plane walls extends past the vortex, develops a kink before meeting the wall at an acute angle. All these flow features makes the perturbed region behind the diffracted shock more complex, and requires a highly robust computational fluid dynamic (CFD) code with optimum resolution for its analysis. Takayama and Inoue [63] proposed that the diffraction of an incident shock wave Mach number 1.5 over a ninety degree convex corner be made a benchmark to measure the performance of CFD research codes.

Kleine et al. [27] investigated the diffraction of shock waves on 90° corners at different incident shock Mach numbers. A series of lambda shocks were observed along the shear layer at moderate Mach number. After further diffraction process a second shock that is facing upstream is formed when the flow along the shear layer becomes locally supersonic [59&32]. The pressure of the flow within the expansion fan becomes low while the velocity increases, the flow may become locally supersonic across the expansion fan if the incident shock Mach number is strong enough.

Skews [58], Sun and Takayama [61] and Hillier [21] observed the formation of a secondary shock that is embedded in the main vortex, and it matched the flow condition between the near wall and the flow far away from the wall surface. Parks [46] also observed this shock and related it to the early formation of a vortex behind the diffracted shock wave.

Skews [58] also noticed the formation of a recompression shock which was confirmed numerically by Hillier [21]. The recompression shock is a small shock that forms under the shear layer and it decelerates the reverse flow to match with the upstream flow at the separation point. The upstream flow around the separation point is subsonic while the reversed flow is at high velocity.

Kleine et al. [26] noticed the analogy between shock wave diffraction and flow in nozzles. The locally supersonic flow at the corner was observed to be decelerated by an almost normal shock wave (shocklet) which also interacts with the boundary layer and triggers a local flow separation. Development of this separation in front of the shock leads to the formation of another shock which is oblique in shape (shocklet). This shock is weak and decays with increase in Mach number of the flow and vanishes when the boundary layer becomes turbulent.

The nature of vortex formation behind a diffracted shock wave requires both qualitative and quantitative investigation for proper understanding of the physics of the flow behind the shock. Rott [52] proposed a single vortex model using the acoustic approximation for weak shock waves. This theory was later abandoned due to clear disagreement with experimental result of Howard and Matthews [23]. A formula was later suggested for the vortex sheet, instead of a single vortex the total rate of vorticity was determined as stated in equation (11).

$$\frac{\Gamma}{t} = \frac{V_A^{\,2}}{2} - \frac{V_B^{\,2}}{2} \tag{11}$$

Where V_A and V_B are flow velocities on either side of the slipstream.

The qualitative description of the vortex has been carried out by many researchers. Few works such as Evans and Bloor [17], and Sun and Takayama [62] have actually shed some light on the quantitative analysis of vortices behind a diffracted shock wave on simple convex walls. The production of vorticity behind a diffracted shock is commonly ascribed to the baroclinic effects but it was observed that a large portion of the total vorticity is produced by the slipstream. The baroclinic effect is negligible in shock wave diffraction.

A very important observation on the flow behind a diffracted shock wave was reported by Takayama and Inoue [63] in their bench mark numerical results. All the presentations showed early stages of the flow development except the poster submitted by Edgar and

Woodward. This work showed stages of flow development indicating breakdown of the shear layer into a vortex street, as well as multiple vortices developing on the periphery of the vortex.

Further numerical work by Sun and Takayama [62] observed early development of the flow with series of vortices along the shear layer when using Euler's equation with fine computational grids. The results obtained from the laminar Navier – Stokes solver with an incident shock Mach number 1.5 over a computational domain of 104mm x 73mm showed flow development at later times. The shear layer rolls up into a spiral vortex.

There was a slight attenuation in the flow behaviour when compared to Eulers' results and this was attributed to viscous dissipation. The turbulence model with additional dissipation was used at the same time scales. The results showed the suppression of these vortices, and there is a good agreement between the experimental results obtained from the conventional shock tube and the numerical results. The outcome of the numerical simulations and small scale experimentation in the conventional shock tubes can be summarised as follows:

- Most flow features of interest could not be distinguished clearly except at higher Mach numbers.
- The shear layer remains smooth both at low and high incident shock Mach numbers in the experimental images, however, Euler's computed result shows some vortices at early times.
- The experimental analysis could not explore the flow behaviour at later times due to the facility constraint.
- The upstream flow behaviour near the wall surface could not be captured due to the scale of the test.

A fundamental question that arises from these observations is "what happens when the scale of the experiments is significantly large?

2.3 Objectives of the present research

The present investigation aims at investigating the global flow behaviour behind a diffracting shock wave at a large scale. The study involves observation of flow interaction over a large convex surface at times significantly longer than what is obtainable in conventional shock tubes. The analysis is accomplished using both experimental and numerical analysis to investigate the transient evolution of the shear layer through the following objectives:

- The effect of large (temporal and spatial) scale experimental analysis of the flow features behind the diffracted shock will be studied for low Mach number incident shocks.
- The numerical analysis of both low and high Mach number incident shocks will be investigated.
- Analysis will be carried out on both plane (30° and 90°) and curved (200mm and 400mm diameter) convex walls.
- The influence of the incident shock on the global flow behaviour will be studied.
- The effect of wall geometry on the separation phenomenon will be investigated.
- The transient development of the unsteady shear layer will be comprehensively described.

The result of this analysis will give the detailed flow behaviour behind a diffracting shock wave and will enhance the understanding of the physics of the flow.

3.0 MATERIALS AND METHOD

3.1 Research Methodology

The objectives of this research were accomplished by both numerical and experimental analysis. The experimental design was guided by the results of the numerical simulation, and parameters of interest were determined based on their influence on the complex flow structure behind the diffracting shock. The parameters of interest are as follows: pressure, velocity, radius of curvature of the model, incident shock strength and the density of the fluid.

This chapter discusses the experimental and numerical methods used for the analysis. The numerical method consists of modelling, description and discretization of the flow domain, specification of the boundary conditions, description of the solution procedures, verification and validation of results, and processing of data. The experimental method involves model design and fabrication, description of the experimental facility and instrumentation, experimental procedures, data acquisition and flow visualization technique.

3.2 Numerical Method

The numerical method analysed the flow behaviour behind the diffracting shock wave by means of computer-based simulations. The analysis was structured around three main activities identified as follows: pre-processing, solution technique/solver and post-processing. The pre-processing covers domain description and discretization, modelling of physical phenomenon by means of governing equations with necessary assumptions, description of initial and boundary conditions. The solution of the governing equations was discussed under selection and justification of the solver. The post-processing is the generation of results in form of plots and images for proper interpretation. The numerical analysis was carried out using two commercial software; Fluent 6.3 for the simulation and Tecplot (360 R2009 R2) for image processing.

3.2.1 Pre-processing

The pre-processing involves the development of a two–dimensional geometry followed by the generation of computational grids. This was achieved using GAMBIT (a package for geometry development and grid generation). The flow domain was defined using a characteristic length chosen as the radius of the convex wall in the case of the circular arc. For other geometries the dimension of the inlet to the test section of the experimental shock tube was used as the characteristic length. This is because the simulations were carried out to mimic the large scale experiments. The maximum length of the incident shock is dependent on the inlet height.

Figure 3.1a shows the flow domain used for the simulation before the generation of cells. For the curved walls, the inlet boundary is three characteristic lengths high and about four characteristic lengths upstream of the start of the wall curvature. This was employed to allow for the damping of numerical noise arising from the impulsive starting of the flow at the inlet. The height of the outlet boundary and the distance between the curvature and the outlet boundary is about six characteristic lengths. This ensures that the interaction of interest is not affected by the flow at this boundary. The maximum dimension for both inlet and outlet were the exact dimensions of the experimental shock tube (inlet = 0.45m and outlet = 1.105m).

The geometry was drawn using various dimensions for edges which form a wireframe of a closed face. The edges AB, BC, CD, DE and EF were joined while the edge GH (i.e a semicircle of radius "r") was used to close the face. The boundary types for the simulation are pressure-inlet, pressure-outlet and no-slip walls. The meshes were generated using unstructured quadrilateral cells with the initial cell dimension of 3mm as shown in Figure 3.1b. The y^+ value of the cell nearest to the wall was set to 11.63 in the region under the shear layer so that the boundary layer could be properly resolved. This lies within the recommended value range of $5 \leq y^+ \leq 30$ specified for the k-ω turbulence models that are implemented in Fluent [66]. This is particularly important as the global flow features that are of interest are strongly influenced by this. The grids generated at

the curved region of the flow domain are shown in Figure 3.1b. The values of y^+ at other boundaries such as BC, DE and EF are greater than 11.63, but less than 100 in order not to increase the computational resources required for the simulations. It is important to note that the flow domain does not require much refining at regions far away from the wall before the start of the simulation because cells were dynamically refined during simulation. The grid adaption based on density was used to refine the cells at regions of significant density gradient. The final discretized flow domain (i.e Figure 3.1c) was imported into Fluent for further analysis.

The flow is governed by the mathematical equations based on the fundamental fluid dynamic principles; mass conservation, conservation of momentum and conservation of energy. The density and pressure are related by the perfect gas law; this is justified by the fact that the maximum temperature is well below 1000K for the incident shock Mach numbers tested. The gas is assumed to be perfect and this necessitates the use of ideal gas equation (i.e equation (2)) to relate density and pressure.

The flow governing equations are the Navier – Stokes equations, and the energy equation coupled through the density–pressure relationship. The constitutive relation expresses the shear stress terms as a function of velocity gradients; the simplified form of this relation is shown in equation (12).

$$\tau = \mu(\frac{\partial U}{\partial y}) \tag{12}$$

Where τ is the shear stress, μ is the viscosity and U is the flow velocity. This relationship is very important in explaining the separation phenomenon especially in viscous flows [56]. The flow domain around the geometry of interest can be divided into three regions based on Prandtl hypothesis: the laminar sub-layer where the fluid closest to the wall is dominated by viscous shear ($y^+ < 5$), the boundary layer where the effect of viscosity varies with distance from the adjacent surface ($5 < y^+ < 100$) and inertial dominated region in which viscous effects is not significant. The present study is largely inviscid

flow except near the wall where viscous effects play a significant role. The scope of the present analysis is limited to the region above viscous sublayer (i.e $y^+ > 5$).

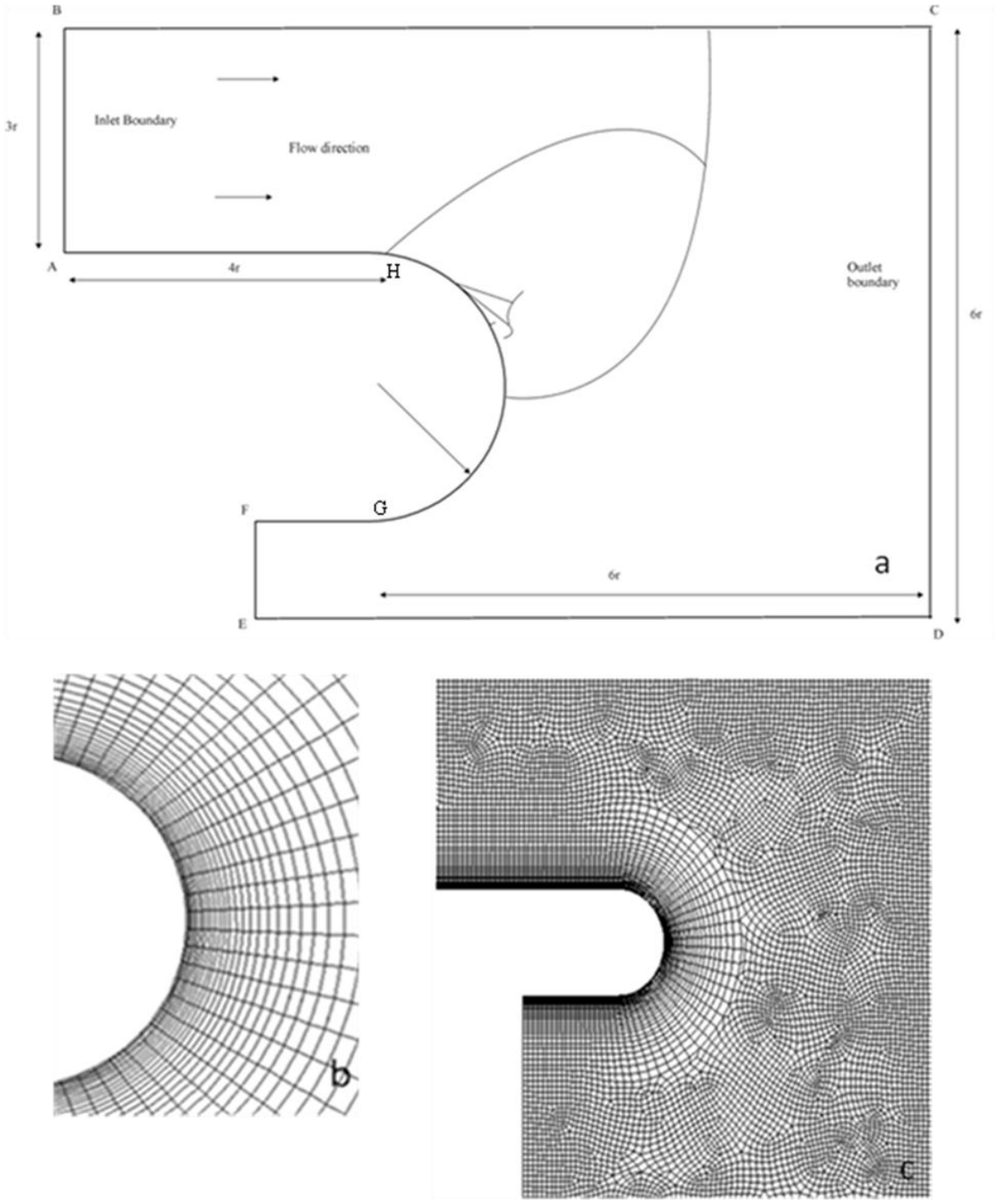

Figure 3.1: The flow domain for the numerical simulations

(a) Actual domain before discretization (b) The grids around the curvature (c) The discretized flow domain

The flow was initially modelled using both inviscid and viscous flow situations based on the earlier work by Law et al. [32] , Takayama and Inoue [63], and Sun and Takayama [62]. In these works both Eulers and Navier-Stokes solvers were used and compared to the experimental results obtained from conventional shock tubes. Law et al. [32] noted a discrepancy between the Navier-Stokes solution and the experiment regarding the shape and position of the shear layer, and attributed it to the instability in the finite volume method used by the numerical package. Other flow features such as position of the separation point and behaviour of the bulk flow field were confirmed to be in good agreement with experiment.

A specific case of incident shock Mach number 1.5 on a 90° corner wall was examined by Sun and Takayama [62] over a flow domain of 104 x 73mm. The Eulers' result with coarse computational grids did not show any instability but fine grids did. The result of a similar simulation using the Navier-Stokes equations with laminar boundary conditions showed a smooth shear layer at small times with instability developed at later times. There was also a small attenuation which was attributed to viscous dissipation resulting in damping. Further analysis using the k-ε turbulent model with additional dissipation suppressed the vortices and the results were in good agreement with published experimental results at the time.

The focus of the present investigation is flow separation. The sufficient condition for this phenomenon is the presence of an adverse pressure gradient relative to the direction of the flow, and zero shear stress at the wall [55]. For low incident shock Mach numbers, Euler's equation may not be appropriate. This is due to the significant viscous effect along the wall, and the adverse pressure gradient propagated behind the diffracting shock wave may not be strong enough to predict the separation point accurately. At high incident shock Mach numbers, Euler's equation meets the two requirements for separation as earlier observed by Law et al. [32].

The present analysis requires a model that will adequately resolve the near wall effects. It must also suppress viscous dissipation at region far away from the wall. The standard k-ε

turbulence model that was developed by Launder and Spalding [30] and the k-ω turbulence model are considered for the analysis. The k-ε turbulence model focuses on the mechanism that affects turbulent kinetic energy. It has two equations, one for k (turbulent kinetic energy) and the other equation for ε (turbulent dissipation rate) [22]. For high Reynolds number flows some wall functions for the standard k-ε turbulence model were developed based on the assumptions that the viscous effects unrealistically penetrate above the viscous sublayer. The pressure gradient is retained in order to achieve a solution which does not depend on gradient matching [34]. At low Reynolds numbers Patel et al. [47] modified the k-ε turbulence model by introducing wall damping to ensure that viscous stresses take over from the Reynolds stresses near the wall.

The k-ω turbulence model was developed to resolve the viscous effect along the wall surface [28]. Application of these turbulence models to shock separated flows have been carried out by many researchers such as Liou and Huang [39], Viegas et al. [65] and Knight [28]. The results show that the surface pressure in the separation bubbles is higher than the measured value, the skin friction is higher than what is measured downstream of reattachment, and the velocity downstream of reattachment is in excess of the experimentally measured value. Various modifications have been carried out over time to ensure the accuracy of the turbulence models [68-70].

The two turbulence models (k-ε and k-ω) were blended together by Menter [41] to form the SST k-ω turbulence model. The free stream independence of the k–ε turbulence model and the accurate prediction of the viscous effects of the flow close to the wall by the k–ω turbulence model make the SST k–ω turbulence model more suitable for the present analysis. This model looks more promising than both the k–ω and k–ε turbulence models particularly in the analysis of a separating flow, which requires adequate resolution of near wall effects without introducing unnecessary viscous dissipation outside the boundary layer. It has been confirmed accurate and more reliable for adverse pressure gradient flows [43], however, its accuracy in the analysis of shock wave diffraction is not well reported in the literature. The present investigation uses the SST k-

ω turbulence model complemented by the k-ε turbulence model for high Mach number flows.

The Reynold stresses in the equation are related to the mean velocity using the Boussinesq hypothesis [68]. This hypothesis is used in the k – ω and k – ε turbulence models because there is relatively low computational cost associated with the computation of turbulent viscosity. The Boussinesq hypothesis has two additional transport equations: for the turbulent kinetic energy (k) and either the turbulent dissipation rate ε or the specific dissipation rate ω. The turbulent viscosity is then computed in terms of k and ε.

3.2.2 The solution technique

In setting up the simulation, the 2-dimensional, coupled density based Navier-Stokes solver of Fluent 6.3 was chosen. The data were generated using equations (9&10) in section 1.22. The gradient option was cell based and the SST k - ω turbulence model was enabled in the solver. The fluid material used is air and the ideal gas law was selected to compute density. The operating condition was set at zero gauge pressure for the reference position F (Figure 3.1) defined by x = 0 and y = 0. The boundary conditions were given as total gauge pressure and the static pressure. These parameters were used in Fluent for solution initialisation to provide initial conditions at different incident shock Mach numbers. The stagnation temperature was used as input for the total temperature and the turbulent flow parameters were given according to the Fluent 6.3 prescriptions.

The solution was initialised from the inlet relative to the cell zone and the system was patched by the ambient flow conditions. The control parameter which is the Courant number was set to 1.5, and the flow discretization was set at second order upwinding in space. This higher order upwinding scheme considered the flow direction when calculating value of a parameter at the face of a cell. The convective value of a parameter was determined from neighbouring points, this minimised the discretization errors by considering wider influence. The dynamic adaption that generates grids at the instant of

the formation of important flow features was used. The adaption parameter is the density because all the flow features of interest produce significant changes in density.

A series of simulations were carried out using the boundary conditions for different incident shock Mach numbers as listed in Table 3.1. The data were computed using equations (9-10) in section 1.2.2. This is the main input into the solver from which the initial conditions were generated at all solution points. The solutions were obtained using an explicit scheme which linearized the source term by substituting the initial values. The value for the new time step was obtained from the old time step by forward marching. The value of the various parameters was obtained at the new time step using the values at the old time step. Data were generated for the set of flow conditions and stored as compressed files to save hard drive space on the computer.

Table 3.1: Simulation data

Incident shock Ms	Initial supersonic Pressure	Flow Mach number	Stagnation Pressure	Stagnation temperature
1.40	176596	0.51	210916	386.76
1.45	190445	0.56	235370	400.67
1.50	204780	0.60	262101	415.08
1.55	219600	0.65	291228	429.98
1.60	234906	0.69	322867	445.36
1.65	250698	0.73	357130	461.23
1.70	266977	0.78	394131	477.59
1.75	283741	0.80	433976	494.44
1.80	300991	0.84	476770	511.78
1.85	318727	0.87	522615	529.60
1.90	336949	0.90	571606	547.91
1.95	355657	0.93	623835	566.71
2.00	374850	0.96	679390	586.00
2.40	545893	1.16	1252446	757.90
2.60	643076	1.23	1630697	855.57
2.80	748034	1.30	2073414	961.05
2.90	803429	1.33	2319387	1016.72
2.96	838174	1.35	2477551	1051.64
2.97	842207	1.35	2496096	1055.69
2.97	845094	1.35	2509392	1058.59
3.00	860767	1.36	2581906	1074.34
3.01	863685	1.36	2595467	1077.28

The results were processed into velocity, pressure and density contour plots as well as velocity vector plots using the post processing facilities in Fluent. The numerical schlieren images used for direct comparison with the experimental results were obtained using Tecplot 360 (R2009 R2). The density gradient generated in Tecplot is similar to the experimental schlieren visualization images which will be discussed later under experimentation.

Figure 3.2 shows the four points at which pressure histories were recorded for the curved wall simulations. The points are defined as P_1, P_2, P_3 and P_4, and specified using point definition in Fluent 3.2. Each point was identified using its coordinates (x, y) referenced to point E (0, 0) in Figure 3.1. Four windows were activated in the animation menu for the four locations. The time-step for the simulation is 1μs and the total time interval of about 1500μs was considered for the pressure history. The pressure at each time-step was recorded for the total time interval and saved in four separate files during the simulation. These were compared directly with the pressure trace obtained from the experiments.

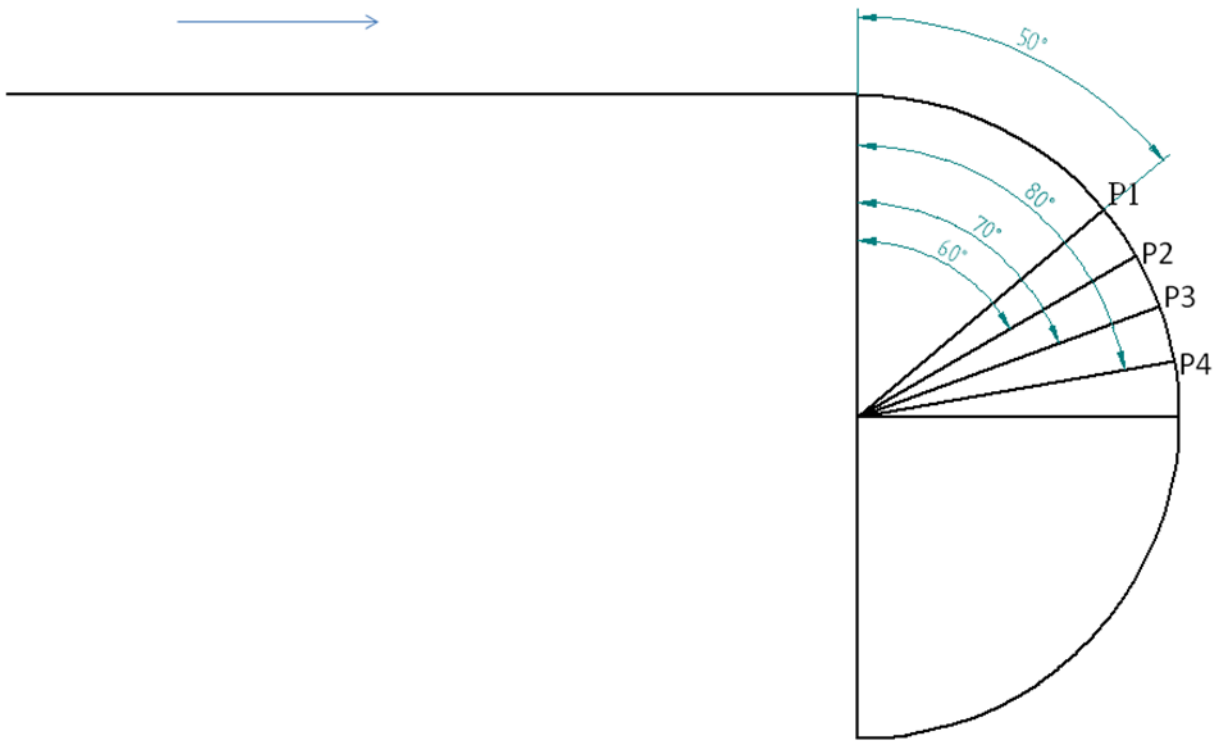

Figure 3.2: Location of points at which pressure histories were recorded

3.3 Experimental Analysis

Shock wave diffraction is an unsteady process, the flow behaviour behind the diffracting shock changes with time. In order to examine the flow features comprehensively after long times of diffraction process. The flow need to be modelled in a large scale facility. The experimental analysis requires generation of a planar shock wave that travels a significantly long distance before encounters the convex wall. The pressure across the shock is expected to be determined before the start of the diffraction process in order to compute the strength of the shock. As this shock diffracts over the surface of the model, the pressure history at four different locations need to be recorded. These pressures will be used to determine the behaviour of the shock as it diffracts over the model and to identify the time at which the separation of the flow occurs. The images of the interactions behind the diffracting shock need to be visualised for different positions of the shock. This requires setting up an optical system that can be triggered at the instant the shock wave crosses a particular region. The experiments were set up to cater for these requirements and the equipments used are: a large scale shock tube, a data acquisition system, a schlieren optical system and data logger.

3.3.1 Experimental facility

Large scale experimental analyses were conducted in a purpose built shock tube at the Flow Research Unit of the School of Mechanical, Industrial and Aeronautical Engineering, University of the Witwatersrand, South Africa. The facility has the potential of generating shock waves up to a Mach number of 3.0. However, high Mach number tests could not be attempted owing to the possibility of damaging the test section windows which were made of glass. Furthermore, the wall directly at the exit of the test section was damaged twice during the preliminary tests of the shock tube at high Mach numbers.

The shock tube consists of a 2m long cylindrical driver section (450mm diameter) bolted to the driven section of cross sectional area 0.1 x 0.45 m^2 divided into three parts of 2m

in length each, as illustrated in Figure 3.3. The overall length of the shock tube is 10m. A diaphragm pricker was fixed to one side of the tube at a region where the driver and driven section were bolted together. The diaphragm pricker was made up of a stainless steel needle, a spring and a long string. They were fitted together to form a system that was used to rupture the diaphragm that separated the high and low pressure sections. The shock was generated either by increasing the pressure in the driver section (compression chamber) or by pricking the diaphragm by means of the pricker.

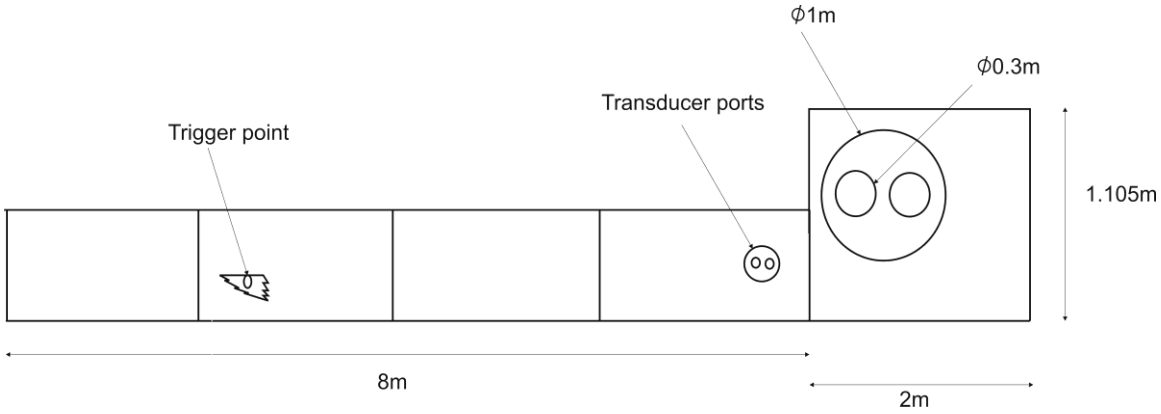

Figure 3.3: Schematic diagram of the large scale experimental shock tube

The desired thickness of the diaphragm was obtained by combining different thicknesses of polyester film sheeting to achieve the required burst pressure. This may be one or several sheets stacked together depending on the pressure required in the driver section. Table 3.2 shows the thickness of the diaphragm and the natural burst pressure for different combinations of polyester film sheets. The natural bursting of higher combination (i.e Thickness > 125μm) could not be determined in the present experiments because higher test pressures (P > 7bars) were not used.

The driver section was located at one end of the shock tube with two ports: an inlet port on top through which air was supplied into the vessel and an outlet port underneath from which the pressure of the compressed gas was measured by a pressure gauge. The driver section was positioned on a frame with wheels for free movement of the cylinder when

changing the diaphragm. A gasket was used between the driver and driven section before they were bolted together so as to ensure adequate sealing.

Table 3.2: Determination of natural bursting of mylar sheeting combinations

Diaphragm thickness (μm)	Mylar sheeting combinations (μm)	Approximate natural burst pressure (kPa)
50	50	220
100	100	370
125	25 and 100	490

The driven section consists of a long rectangular channel of length 6m divided into three equal parts (A,B and C) of dimensions 2m x 0.1m x 0.45m, bolted together as indicated in Figure 3.3. Each section has flanges at both ends, and there were three holes at both sides of the flanges bolts. The sections were joined together with a gasket between them to ensure adequate sealing against air leakage. Three bolts were used at each side of the flanges for proper gripping against vibration during testing. The three parts of the driven section were carefully aligned to avoid unwanted disturbance of the planar shock on its way to the test section. The inner surface is smooth, painted and proper setting of the gasket was ensured at various joints. The driver section was designed for a maximum pressure of 12bars but the present tests could not be extended beyond 6 bars for safe operation.

The driver section of the shock tube was operated with a control panel which consists of an inlet hose and valve, air filter and a pressure gauge. The amount of air from the pressure line that gets into the driver section through the inlet hose was controlled by the inlet valve. The air filter removes impurities that could cause premature bursting of the diaphragm while the pressure gauge measures the pressure in the driver section. The ambient temperature and pressure were measured at intervals during the experiments by a

mercury - bulb thermometer (resolution of $\pm 0.5^{o}C$) and a digital barometer (resolution of $\pm$ 1mbar) respectively.

There were two transducer ports on the driven section located close to the inlet of the test section; these ports housed the transducers that measured the pressure rise across the planar shock wave. The distance between the two transducers is 0.05m and the first port is about 0.49m from the start of the diffracting surface. The transit time between the two transducers was used to calculate the velocity of the incident shock before the start of diffraction of the shock wave on the model.

The test section has two circular glass windows of diameter 0.30m enclosed in a circular frame of diameter 1m. This is surrounded by a device that enables 360° rotation of the frame to give coverage of the whole domain, as shown in Figure 3.4. The model was fixed in the test section within the glass window such that the surface of interest was located within the field of view of the optical system.

The whole test section stands on wheels which allow for easy movement when new models are mounted in it, and for proper alignment of the test section with the rest of the shock tube. There is a muffler bolted to the exit of the test section to reduce the strength of the wave leaving the shock tube before it impacts on the blast barriers that were arranged around the muffler to lower the speed of the exiting air.

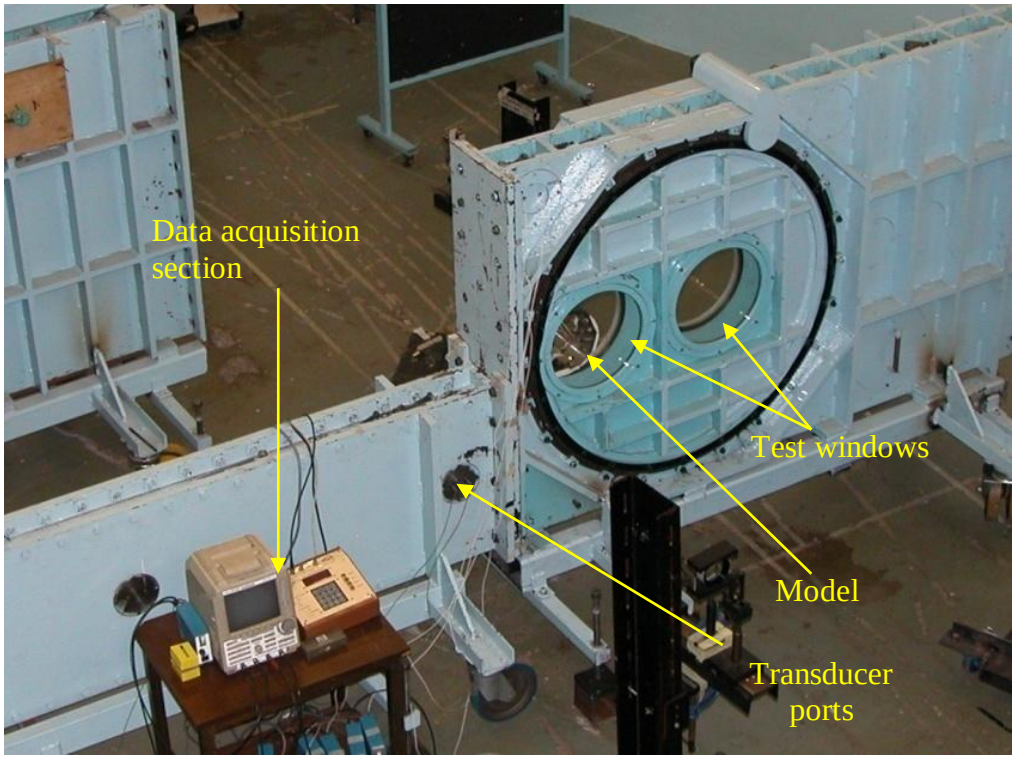

Figure 3.4: The large scale shock tube facility

The following devices in the large scale shock tube are important modifications that make the facility different from the conventional shock tube. There are two transparent glass windows of diameter 0.3m each through which the interactions behind the diffracting shock was captured. This facilitated enough space for large scale diffraction process. Any of these windows can be used, depending on position and type of the model to be examined. The present facility can allow for a diffraction time of about 1500μs depending on Mach number. This is about 10times what is obtainable in most conventionally sized shock tubes. The rotation of the circular frame of diameter 1m that encloses the glass windows facilitates wide coverage of the flow field in the test section irrespective of the orientation of the model. The fixing of the test section on an adjustable stand ensures variation of the height of the test window with respect to optical arrangement. The facility is suitable for testing of both weak and strong shock waves. One of the glass windows is divided into square grids by tiny string for estimation of the size of a flow feature of interest.

3.3.2 Instrumentation

The instrumentation consists of a time delay box, a 4 – channel Yogokawa oscilloscope (Model DL1540) that displays the pressure trace, 6 signal amplifiers (PCB Piesotronic 482 series) and 6 transducers. The specifications of various transducers used on the surface of the models are shown in Table 3.3. The two transducers on the driven section are connected to the signal amplifiers and to the oscilloscope which displays the pressure trace at each port. A sudden rise in pressure indicates the instant of shock traversing the surface of the transducers. The shock velocity is determined from the distance between the two ports and the time taken by the shock to cover the distance between the transducers.

The approximate time taken by the shock to arrive at a particular location on the model is estimated based on the shock speed earlier determined from the two transducers on the driven section. This is used to set the time delay to trigger the light source which is employed to capture the interaction of interest at different position of the diffracting shock wave. Four other transducers are used to record the pressure traces on the surface of the model and are connected to the data logger through signal amplifiers. For the curved walls the location of the transducers are designated by P_1, P_2, P_3, and P_4, and are located 50°, 60°, 70° and 80° from the inlet as shown in Figure 3.2 (section 3.2.2). The detailed drawings are shown in Appendix A.

Table 3.3: Transducer calibration constants

Serial Number	Name of the port	Transducer specification	Calibration constant
14051	P_1	113A21	3.3424 mV/kPa
5478	P_2	113A21	3.62595 mV/kPa
19619	P_3	113B21	3.33587 mV/kPa
6397	P_4	113A21	4.11910 mV/kPa

For the 30° wall nine transducer ports were made at various locations downstream of the corner vertex. Four of these ports are used during each test and the remaining holes are covered by blind plugs specially fabricated for this purpose. The surfaces of these blinds are smooth and flush with the surface of the model to avoid undesirable reflections. The transducers are arranged at different locations where the pressure trace is recorded. The specifications of the transducers are shown in Table 3.3.

3.3.3 Flow visualization technique

The flow behaviour behind the diffracting shock wave is characterized by density gradients. The schlieren flow visualization technique was used because its principle is based on the relationship between change in light intensity and the gradient of the refractive index in the fluid. It was developed more than a century ago and is attributed to Foucault (1859) and Toepler(1864) [40]. The non-uniformity in the flow field behind the diffracted shock alters the direction of a collimated beam of light passing through the flow. The deflection of the light is due to the resultant change in the refractive index of the flow as a result of density gradient.

The gradient of the refractive index in a test fluid can be obtained from the evaluation of the local change in the intensity of the light ($\frac{\Delta I}{I}$) in the schlieren image. This evaluation is expressed in a simplified form as shown in equation (32) [40].

$$\frac{\Delta I}{I} = c \int_{\xi}^{\xi_1} \frac{\partial n}{\partial y} dz \tag{32}$$

where c is a constant for the mirror or lens. $\frac{\partial n}{\partial y}$ is the gradient of the refractive index perpendicular to the knife edge which depends on the density of the fluid as shown in equation (33) [40].

$$n - 1 = k * \rho \tag{33}$$

n is the refractive index, *k* is the Gladstone-Dale coefficient which is 0.23cm^3/gm for air at standard conditions, and varies between 0.1 and 1.5 for most gases [7]. The above relationship shows that the refractive index is weakly dependent on density; hence, detection of small variation in density using the optics will require very sensitive optical system. The influence of temperature and pressure is not significant on *k* in a flow field at a moderate flow conditions as observed by Barbosa [6&7].

The Z-Type 2-Mirror schlieren arrangement is used. It consists of a light source (1μs xenon flash lamp) connected to a simple electronic switching system to produce a short duration exposure. The light is allowed to pass through a condenser lens (C), a vertical slit and is collimated by the parabolic mirrors (M_1&M_2) as shown in Figure 3.5. The focal length of the mirrors is 1.8m and they are of equal distance from the object at the schlieren field.

The collimated light is allowed to pass through the windows of the test section (flow under investigation) and brought to a focus. Some of the light is blocked at the focus by a knife-edge that was carefully positioned for the purpose. The combination of knife-edges and vertical slits produces higher sensitivity with clear images, and this made this configuration very suitable for the present application. A lens is used after the knife edge to collimate the light again before it is photographed by the camera. The camera used for the experiment is a 10Megapixel Nikon D40 digital camera, with adjustable light exposure times.

The light source of the optical system is connected to the output of the delay box. The signal from the pressure transducer was sent to the oscilloscope via the signal amplifier at the instant of passage of the shock. The oscilloscope sends the signal to the time delay box that has been armed and is waiting for the trigger. The flash lamp was triggered by the output signal of the time delay box. The Mach numbers of incident shock waves for different initial driver pressures are recorded during the preliminary experiments. The approximate incident shock Mach numbers from these preliminary studies are used to compute the trigger times.

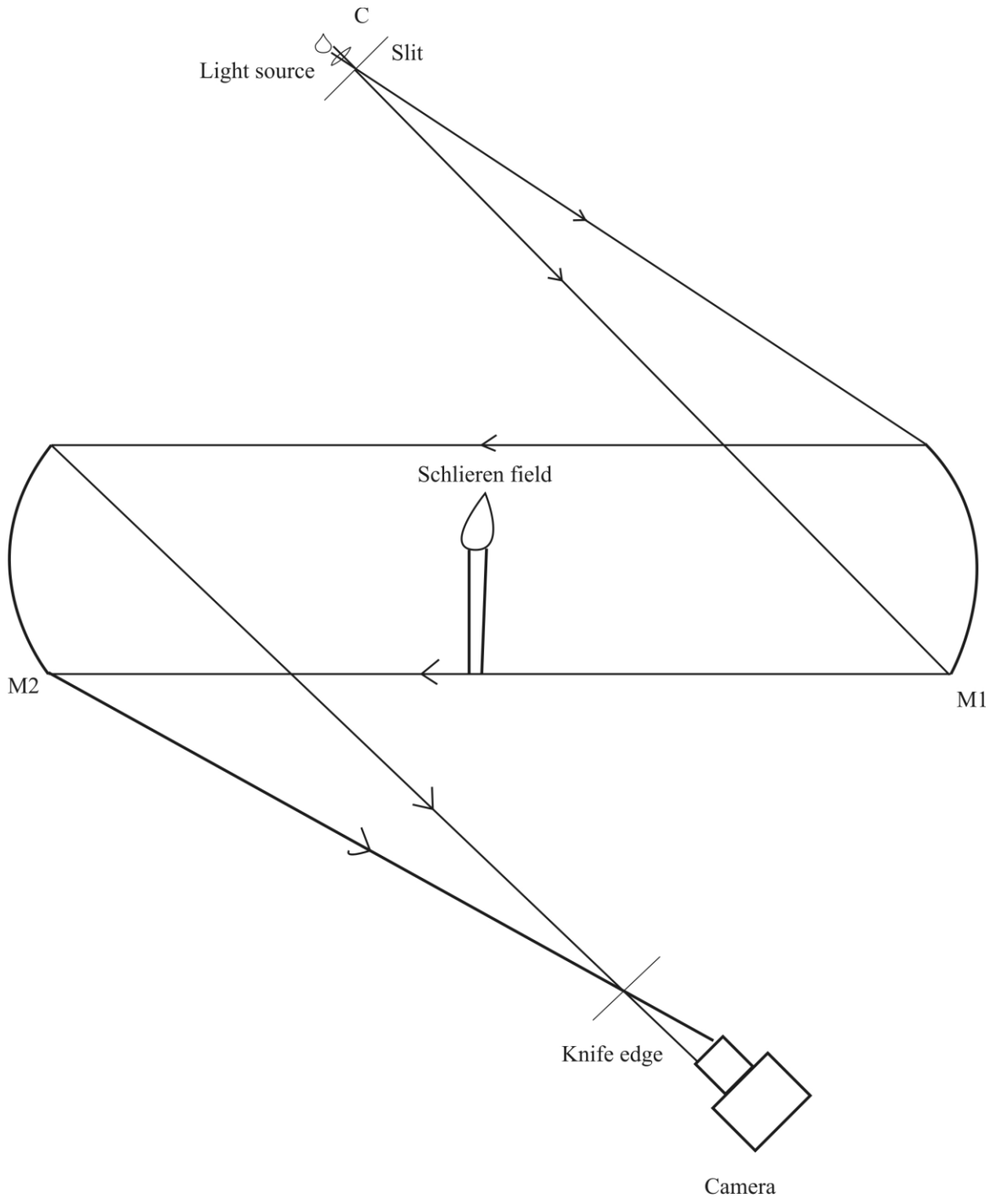

Figure 3.5: Z-configuration schlieren arrangement

3.3.4 Model design and fabrications

The models used for the tests were designed based on the maximum loading that could be generated by an incident shock at Mach 2.0 on a structure. Four models were designed and fabricated at the North West Engineering workshop. These models are 30° and 90° plane, 200mm and 400mm diameter walls. The important features of each model are the location of the transducer ports where the pressure traces were recorded and the convex angle/bend that motivated the diffraction process. Figure 3.6 shows the arrangement of these ports and their location from the centre line OA which is the line of symmetry for a 200mm diameter wall.

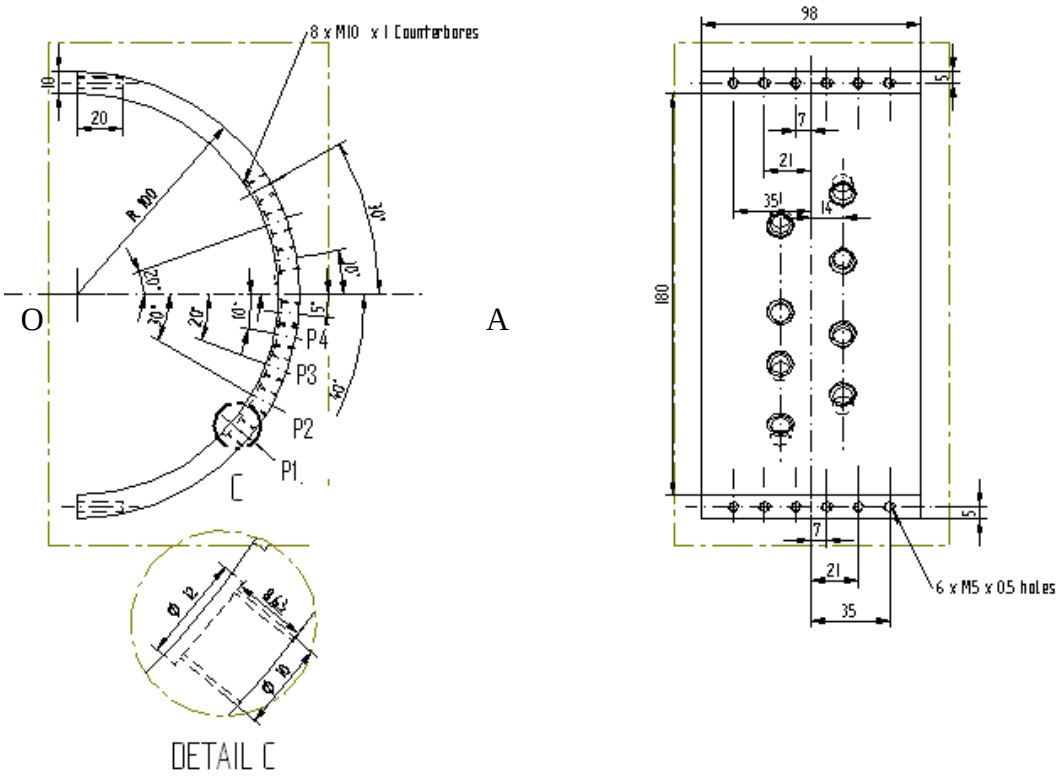

Figure 3.6: The curved model with the transducer ports

The ports were labelled P_1 – P_4 on the model with each port housing piezoelectric static pressure transducer with a known calibration constant. When the shock wave reached location P_1, a sudden rise in pressure trace was displayed by the oscilloscope confirming the passage of the shock wave. The transducers were carefully fitted into the ports with

seals to ensure no air leakage. The surface of the transducer was made flat with the surface of the model to avoid propagation of disturbances around the transducer during the experiments.

Figure 3.7 shows set up of a 200mm diameter model on the universal support. The shock wave that was propagated after the rupture of the diaphragm moved through the driven section and entered the test section. It encountered the convex bend at point A and started to diffract as it moved over the surface ABC. The sides of the model were covered with tape to avoid direct contact with the glass of the test window and to seal the contact area against air leakage. All bolted joints were locked by using two nuts tight together on every bolt. This is to ensure that bolts did not loosen due to the vibration generated in normal operation.

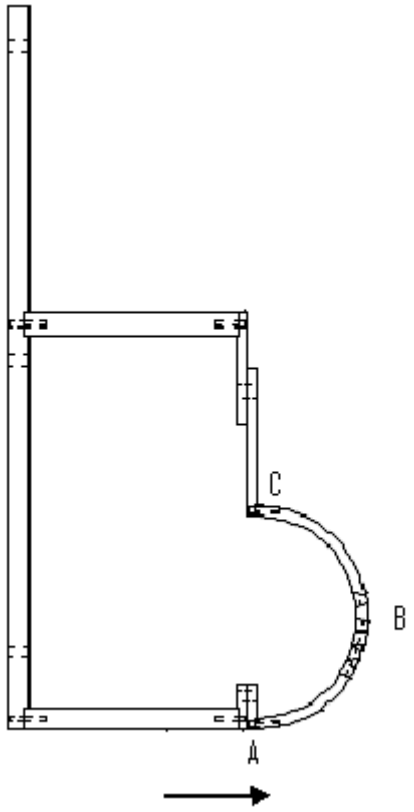

Figure 3.7: The assembly of 200mm diameter model

The assembling of the 30° model is shown in Figure 3.8, and the detailed drawing of the plate that housed all the pressure transducers is shown in Figure 3.9. Plate 1 and 3 were joined to the universal support that is fixed to the inlet plate of the test section. There are nine transducer ports with the first port located at a distance of 15mm from the end A of the plate as shown in Figure 3.9. The location of various transducer ports were specified as H_1-H_9, however, only ports H_1, H_3, H_5 and H_7 were used to record the pressure history. The unused ports were blocked by blind plugs. The shock wave entered the test section and moved over plate 1 before it encountered the convex corner at point A. Diffraction of the shock started from A and continued as the shock moves over the surface of plate 2 which is the surface of interest for this model. The shock encountered the transducer P_1 at H_1, P_2 at H_3, P_3 at H_5 and P_4 at H_7 where the pressure histories were recorded as it traversed the surface.

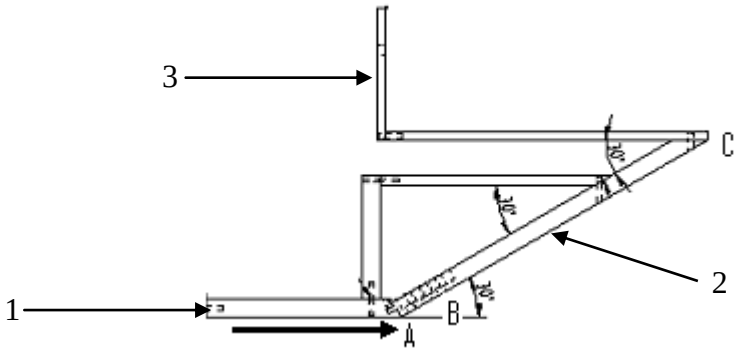

Figure 3.8: Assembly of the 30° corner model

The models that were comprehensively examined are: 30° and 90° plane-wall corners and a 200mm diameter wall. The models were designed in parts and fabricated from mild steel. The assembly of the parts were carefully done especially at joints that have significant influence on the experimental results. Among these regions are point A where the diffraction process commenced and point B which is the surface of the transducers and the blind plugs. This surface was made flat with model surface to avoid reflections that may be generated by undesirable contours. The 400mm diameter model was also fabricated; however, few tests were conducted due to limited separation. The assembly

and positioning of this model is similar to 200mm diameter wall except that it occupies more space in the test section.

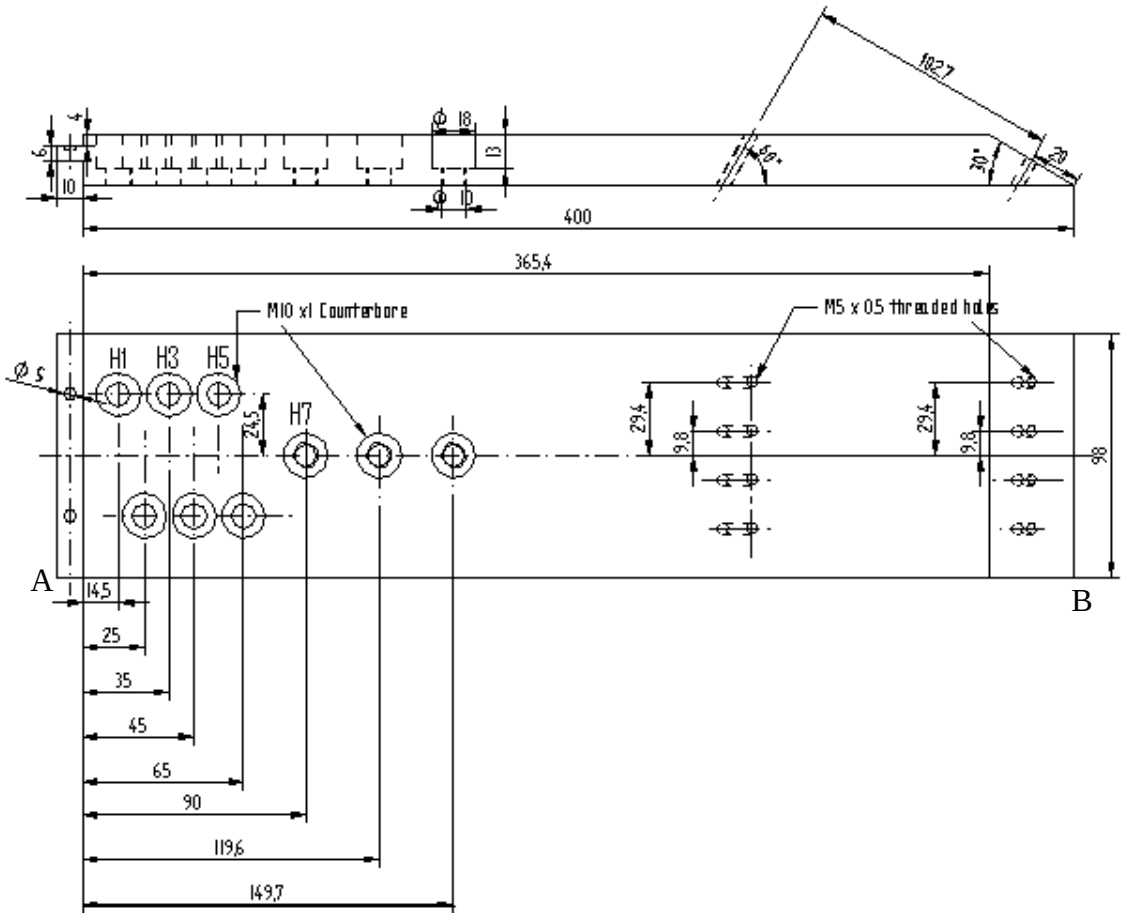

Figure 3.9: Location of the transducer ports on the 30° model

3.3.5 Experimental procedure

Experiments in the shock tube were conducted by following these step by step activities:

- Instrumentation was switched on and enough time was allowed for the system to attain steady conditions.
- The ambient pressure and temperature were recorded from the digital barometer and mercury bulb thermometer respectively.
- The xenon lamp used for the visualization was switched to the external mode.
- The schlieren optical arrangement was adjusted to ensure proper settings.
- The spring of the diaphragm trigger plunger was compressed and latched into the cocked position.
- A new diaphragm was fitted at the inlet to the driven section.
- The supply and other valves on the control panel were closed.
- The main pressure line was opened and the emergency vent was tested for possible blockage.
- The compression chamber was closed and bolted up using a pneumatic wrench.
- The oscilloscope time and voltage divisions were set to the required values.
- The trigger system was set to the required time on the delay box and armed.
- The emergency vent valve was closed
- The laboratory doors were locked using the electronic device which also switched on the warning lamp at the entrance to the shock tube laboratory.
- All the lights in the laboratory were switched off except an operator head lamp that was used to monitor the compression process.
- The inlet valve on the control panel was opened slowly for gradual compression of the driver section.
- The inlet valve was adjusted once the desired pressure has been obtained and the head lamp was switched off.
- The camera shutter which has been set to 1minute exposure was opened
- The string connected to the trigger plunger was pulled for firing.
- The camera closed automatically and the light in the laboratory was switched on

- The inlet valve remained closed while the emergency vent valve was opened.
- The pressure traces were saved from the data logger.
- The inside of the shock tube was cleaned of diaphragm fragments for the next test.

The following precautions were taken during the testing:

- Auditory protective device was used when using the pneumatic wrench and at the time of firing.
- The glass windows and the parabolic mirrors were carefully cleaned with a soft cloth to avoid scratching.
- Area around the exit of the test section is always kept clear during the test
- The inside of the shock tube is always inspected for any foreign objects before the test is conducted.
- The compression chamber was vented after each test to avoid pressure build up in the chamber.
- The camera lens cover is always used to cover the opening when not testing to avoid dust contamination.
- Regular check of all bolts on the test models is required after each test so that any bolts loosened due to vibration can be retightened.

4.0 ANALYSIS OF LOW MACH NUMBER INCIDENT SHOCKS

4.1 Introduction

This chapter analyses the numerical and experimental results of the diffraction of low Mach number incident shock waves. The analysis involves two plane convex walls (30° and 90°) and two curved convex walls (200mm and 400mm diameters). The low Mach number shocks consist of incident shock of Mach numbers $1.30 \leq M_s \leq 1.60$ with special emphasis on M_s 1.40 and 1.50.

Pressure, velocity and density contours plots which show various flow features of interest are extracted from the numerical data. These results are validated using numerical schlieren images for direct comparison with the experimental pictures. The outcome of this analysis is used as a computational guide for the analysis of high incident shock Mach numbers since large scale experimental analysis is limited to $M_s \leq 1.60$.

The major advantage of using a numerical method is the ability to generate a large amount of data due to ease at which the influencing parameters could be varied at a low cost. However, this may turn out to be a disadvantage if the user can not clearly identify the governing parameters at the beginning of the analysis. The user may be overwhelmed by the data and it becomes difficult to know how much of that data is meaningful. The four governing parameters with regard to this work are the incident shock Mach number, the shape of the convex wall, the time of the diffraction process as well as the Reynolds number.

4.2 Verification and Validation of Numerical Results

Figure 4.1 shows the flow features behind an incident shock of Mach number 3.0 that has diffracted for about 1500μs over 30° corner wall. The upper and the lower walls are well spaced, and both inlet and outlet boundaries are far enough away from the surface over which the incident shock is diffracting. The complex flow region is free from the

reflection of wave from the upper boundary, and the numerical noise resulting from the impulsive start of the flow at the inlet has dissipated before the start of the diffraction process. This preliminary simulation result shows that there is enough space between the boundaries and the complex flow region of interest.

The flow domain is illustrated in Figure 3.1. The vertical boundaries: $0.65 < y < 1.105$ and $0 < y < 1.05$ are the inlet and outlet boundaries respectively. Other edges are walls at which the no-slip boundary condition is used. The cells near the wall W_1 are fine enough to resolve the boundary layer under the shear layer. The adaptive mesh generation is used so that sufficient mesh elements will be generated at the instant of formation of any flow features of significant density gradient. The upper wall is sufficiently far away to avoid impingement of the reflected wave from the wall with the complex flow structure at the corner.

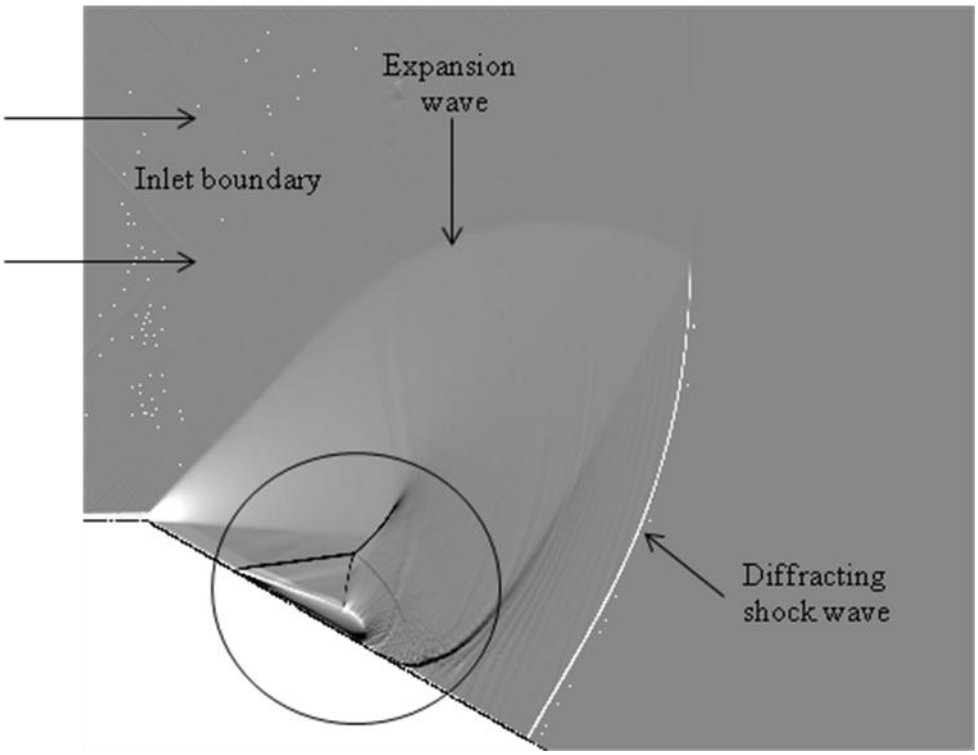

Figure 4.1: Comparison of complex flow region to the computational domain at incident shock M_s 3.0 on 30° corner wall

Figure 4.2 shows the position of separation point at incident shock Mach number 2.0 on a 200mm diameter wall for different number of meshes. This analysis ascertained the independence of solution from the mesh. The solution adaptive mesh generation is used to fix the maximum number of meshes that were considered. The separation point moves with time along the curved wall, however, the present analysis considered the position of separation point at the same instant in time. The position of separation point is defined by the angle between the separation point and a vertical line from the inlet. The solution approaches the asymptotic value of about 62.4 as the number of element tends to infinity. The approximate angle of separation at the time under consideration is 62.4 and the solution became independent of the number of elements as the number of elements reached about 1,000,000 elements. The minimum number of elements used for the simulation was 1000,000.

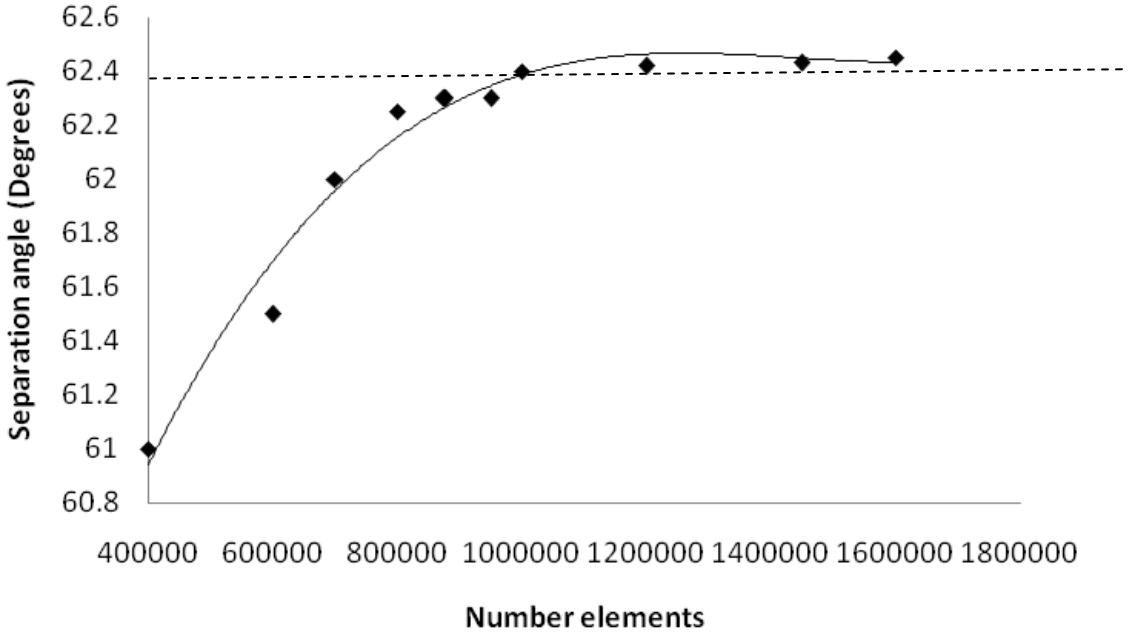

Figure 4.2: The behaviour of separation point for different number of elements at M_s 2.0 on a 200mm diameter wall

The diffraction of an incident shock Mach number 1.5 on the 90° convex wall is shown in Figure 4.3. This particular case is the benchmark proposed by Takayama and Inoue [63]

to measure the performance of CFD codes. Figure 4.3(a, b and c) are experimental images at different diffraction times and Figure 4.3(d, e and f) are results from the SST k - ω turbulence model while Figure 4.3(g, h and i) are from Navier–Stokes solver with laminar boundary conditions. The flow features of interest are: shear layer, lambda shocks (LS), the vortex, the bifurcated shocks (BS) on the vortex, and the contact surface.

The comparison of the images in Figure 4.3 is based on the length of the flow feature of interest measured at time t which is expressed in a non-dimensional form as shown in equation (34). For experimental pictures the length of the relevant flow feature is determined using the square grids positioned over the test window. Each of the grids is 50mm in dimension, and the approximate dimension of the flow features are obtained from the spacing.

The dimensionless time scale is given by τ:

$$\tau = \frac{at}{c} \qquad (34)$$

where c is the characteristic length (radius of the arc for the curved wall and inlet height of the test section for the plane walls), t is the time from the start of diffraction process to the formation of the flow feature of interest, a is the sound speed in the undisturbed region ahead of the incident shock wave.

There is good agreement in the bench mark results between the current experimental images and results of the SST k - ω turbulence model. The lambda shocks are well predicted with the bifurcated shock that is interacting with the vortex. The contact surface and vortex are also comparable with experiment. The shear layer is smoother in the SST k-ω turbulence model than in experimental pictures. The pattern by which the shear layer rolled up into a spiral vortex is the same for all the images.

The laminar Navier–Stokes images show instability along the shear layer at later times. This instability as it develops rolled up into a spiral vortex, followed by the breaking up of the shear layer into vortices as shown in Figure 4.3h&i. These developments follow a similar pattern with the Euler solutions as earlier observed by Sun and Takayama [62], except that it occurred at later times in laminar Navier–Stokes results with laminar boundary conditions.

The development of instability along the shear layer and the eventual breaking up of the shear layer into vortices in the Navier-Stokes (laminar boundary conditions) images (Fig. 4.3g, h & i) can be attributed to viscous dissipation which dominates the entire flow domain behind the diffracted shock. The viscous effect that is required in the flow is supposed to be limited to region close to the wall. The use of turbulence model with additional dissipation removes both the instability and the vortices as shown in the images of SST k-ω turbulence model in Figure 4.3e&f. The result is comparable to the experimental images at the same time scale except that the shear layer is smoother than what is shown in the experiment and this can be as a result of excess dissipation.

The results show that Navier-Stokes equations with the SST k-ω turbulence model is suitable for the analysis at incident shock Mach number 1.5. The choice of SST k-ω turbulence model is motivated by its accurate prediction of near wall effects and ability to capture free-stream behaviour at regions far from the wall.

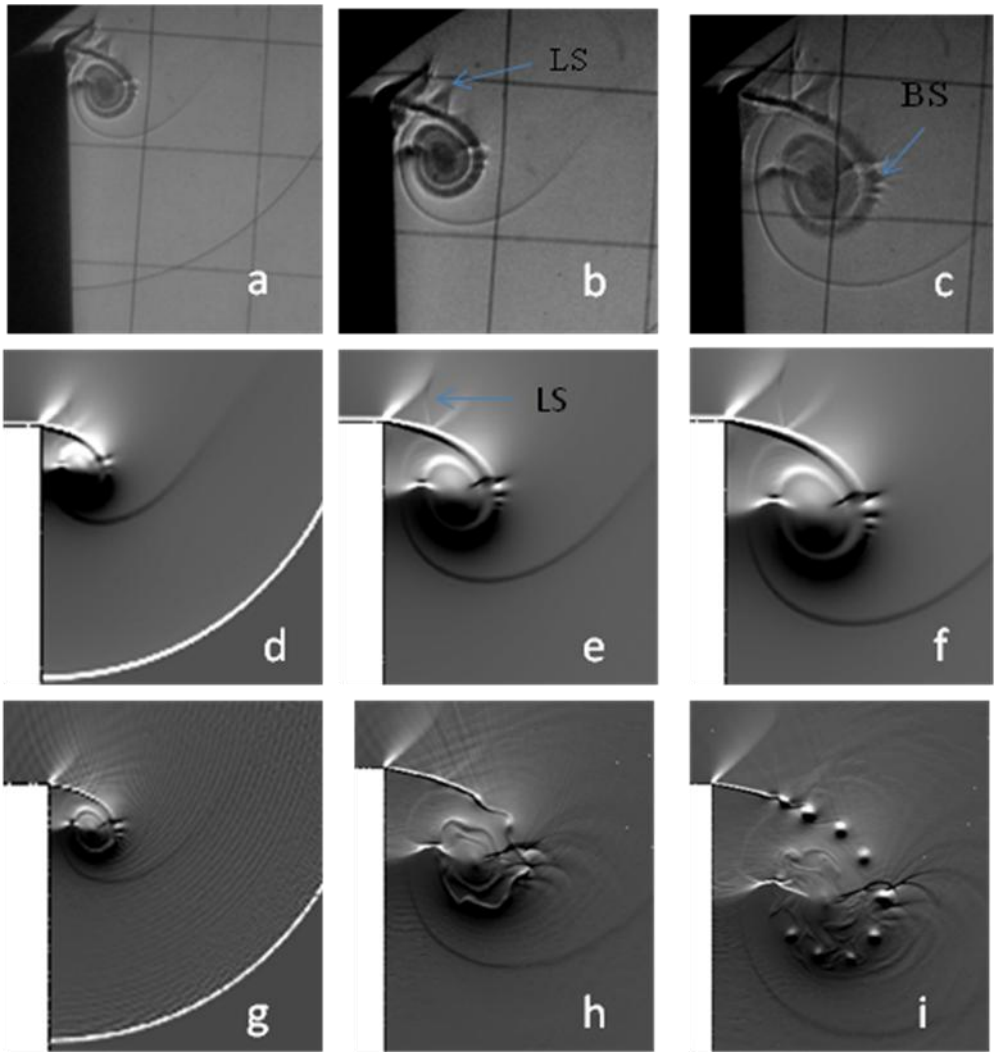

Figure 4.3: The diffraction of M_s 1.5 incident shock on a 90° wall using experimental (a, b & c), SST k-ω turbulence model (d, e &f) and laminar Navier–Stokes solver (g, h & i). Dimensionless time scale τ: (a) 0.2 (b) 0.3 (c) 0.4 (d) 0.2 (e) 0.3 (f) 0.4 (g) 0.2 (h) 0.3 (i) 0.4

4.3 Low Mach number Incident Shocks on Plane Walls

4.3.1 90° corner walls

Figure 4.4 shows the diffraction of an incident shock M_s 1.4 on a 90° corner wall. The diffraction of the incident shock at the corner was followed by flow separation. A shear layer evolved smoothly from the corner with a series of lambda shocks above it. The shear layer extends downstream and is terminated by a vortex as shown in Figure 4.4. The vortex core is not distinct at small times but at later times. The shear layer develops instabilities which break up into vortices as it rolls up into a spiral vortex. The size of the vortex increases as it is pushed downstream by the extension of the shear layer. The vortex begins to disperse when it has moved far enough from the wall surface.

The first two images shown in Figure 4.4a-b correspond to what had been obtained previously on smaller facilities. The time scale is small and the flow behind the diffracting shock has not yet fully developed, thus the shear layer is smooth with lambda shocks spread above it. Images d-i in Figure 4.4 illustrates the development of instability along the shear layer with break-up of shear layer into a chain of discrete vortices. The time scale is about five times what is obtained in conventionally sized shock tubes, there is enough time for the flow to develop while the main vortex fades away. These images show that the earlier observation of the smooth shear layer in the images obtained from conventional shock tubes is limited by the experimental scales both spatial and temporal.

The perpendicular distances between the wall and the vortex core were measured directly from the images in Figure 4.4. To measure the vertical displacement of the vortex, the distance from the vortex core to a horizontal line drawn from the corner was measured. The size of the vortex was estimated from the approximate diameter of the vortex. The measured distances were plotted against time for both numerical and experimental data as shown in Figure 4.6. There is an increase in both vertical and horizontal velocities with time, and the vortex size also showed a significant increase as the diffraction process progressed downstream.

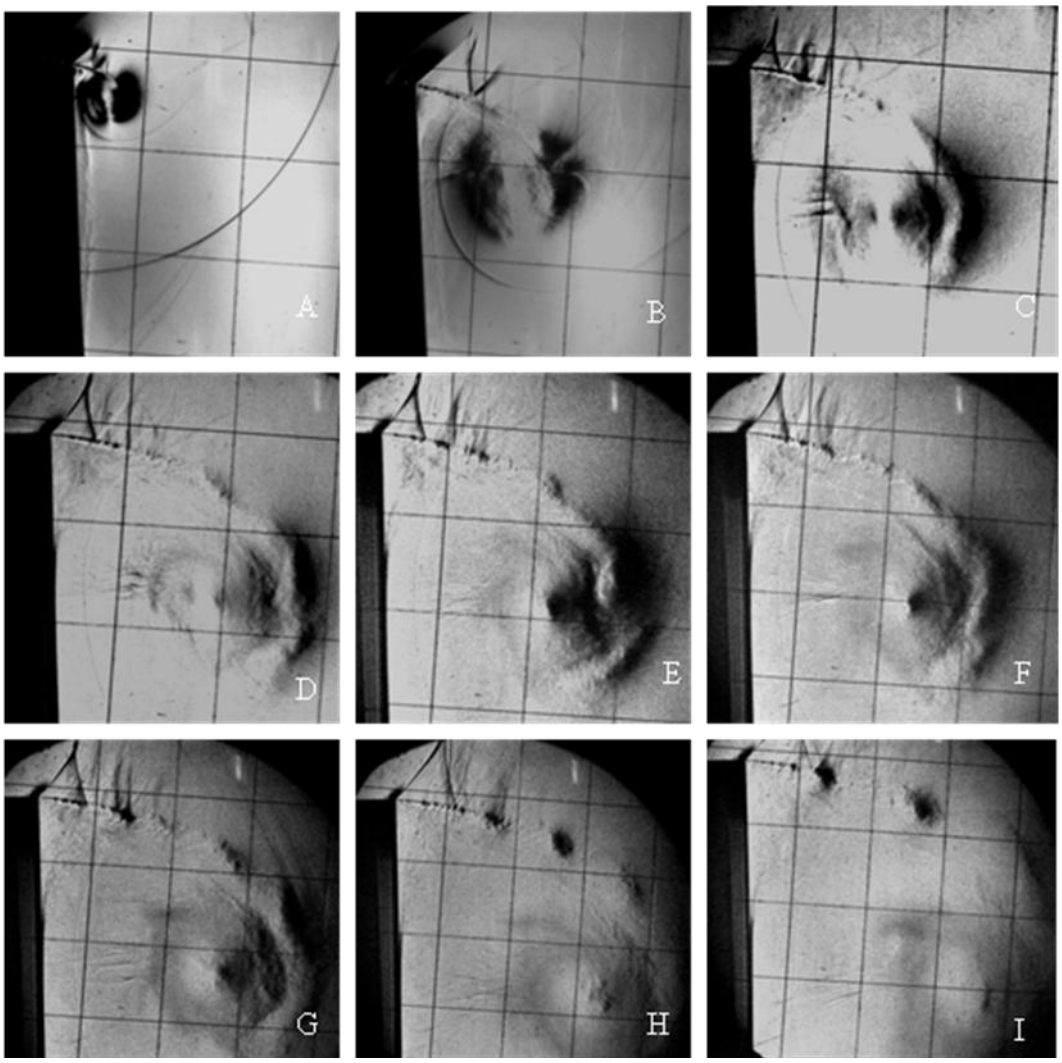

Figure 4.4: Experimental images of the flow features at incident shock Mach number 1.4 on 90°convex corner

Non-dimensional time scale τ: (a) 0.15 (b) 0.23 (c) 0.3 (d) 1.1 (e) 1.3 (f) 1.6 (g) 1.9 (h) 2.3 (i) 2.5

Figure 4.5 shows the numerical images of the diffraction of an incident Mach 1.4 shock over a 90° convex corner. These images were obtained from Reynolds Average Navier–Stokes (RANS) solver with a laminar wall model. The viscous effect is less pronounced than at Mach 1.5. The shear layer evolved smoothly from the corner as earlier observed in the experimental pictures. At later times instabilities developed along the shear layer as it rolled up into a spiral vortex. The shear layer eventually broke up into a series of vortices in the pattern of a Kelvin-Helmoltz instability.

Further analysis using the SST k-ω turbulence model shows no significant difference from what is observed at Mach number 1.5. The shear layer remains smooth from the corner throughout the diffraction process. The break-up of the shear layer into vortices is not evident. However, other flow features such as the bifurcated shocks that interact with the vortex, the lambda shocks above the shear layer and the contact surface remain the same. The instability which is evident in the experimental images and Navier-Stokes solver (with laminar boundary condition) is not evident in the SST k-ω turbulence model results. This shows that the turbulence model has excess dissipation that damps out the real flow behaviour.

There is a significant change in the size and location of the main vortex from the wall surface. The temporal variation in the perpendicular distance between the vortex core and the wall surface is labelled X in Figure 4.5. The plot of X against the dimensionless time as shown in Figure 4.6 can be used to estimate the horizontal velocity of the vortex using the slope of the graph. The total displacement of the vortex from the corner is obtained as shown in equation (35).

$$S = \sqrt{(x^2 + y^2)} \tag{35}$$

where $S, x \,\&\, y$ are the resultant displacement, horizontal and vertical distances. The plot of this displacement against time (Figure 4.7) gives the total speed of the vortex. The results show that there is no significant variation between the two numerical data, however, there is a 3% difference in the slopes when compared to experimental results.

The size of the main vortex is determined using the approximate radius "R" which is the distance between the vortex core and outer surface of the vortex. This size is obtained by computing the area of the vortex using the radius. The transient change in the size of the vortex is plotted for both experimental and numerical images as illustrated in Figure 4.8.

The numerical results using Navier-Stokes solver (with laminar boundary conditions) under-predict the size of the vortex by about 4% when compared to experiment using the slope of the graphs as a parameter of comparison. The SST k-ω turbulence model shows a variation of about 2% from the experimental result. The small variation between the experimental and numerical (SST k-ω turbulence model) results as shown in (Figures 4.6-4.8) revealed that the numerical simulation gives a good prediction of the general flow behaviour except for shear layer stability.

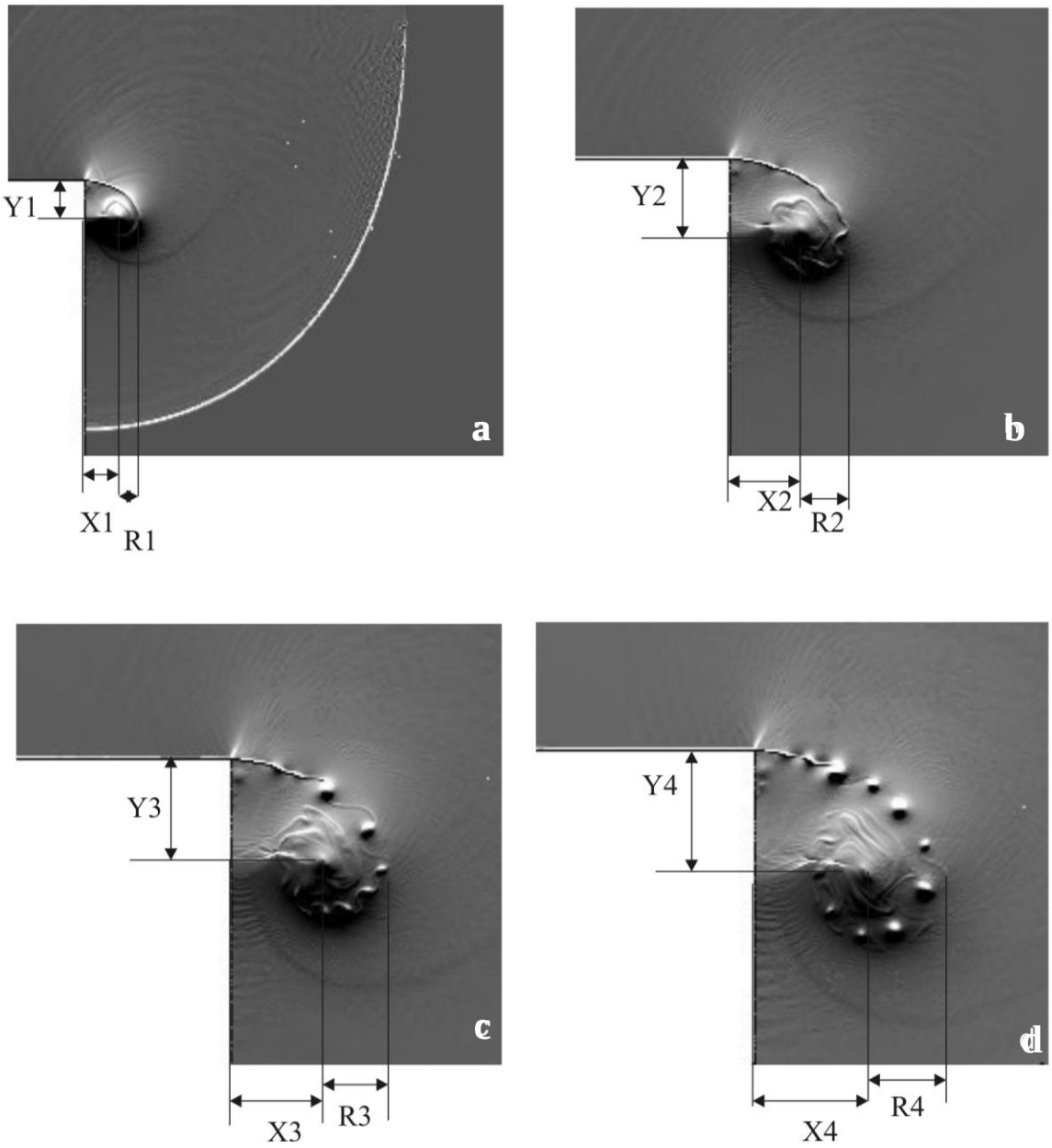

Figure 4.5: The vortices behind an incident shock Mach number 1.4 on a 90°corner using laminar Navier-Stokes solver

Non-dimensional time τ: (a) 0.1 (b) 0.8 (c) 1.1 (d) 1.3

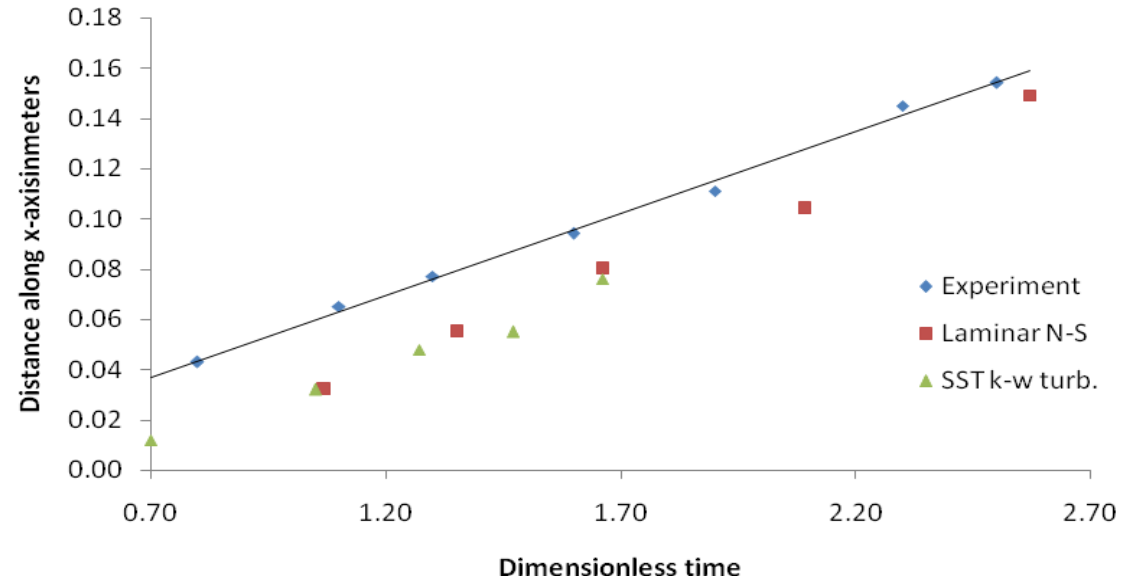

Figure 4.6: The horizontal orientation of the vortex with time

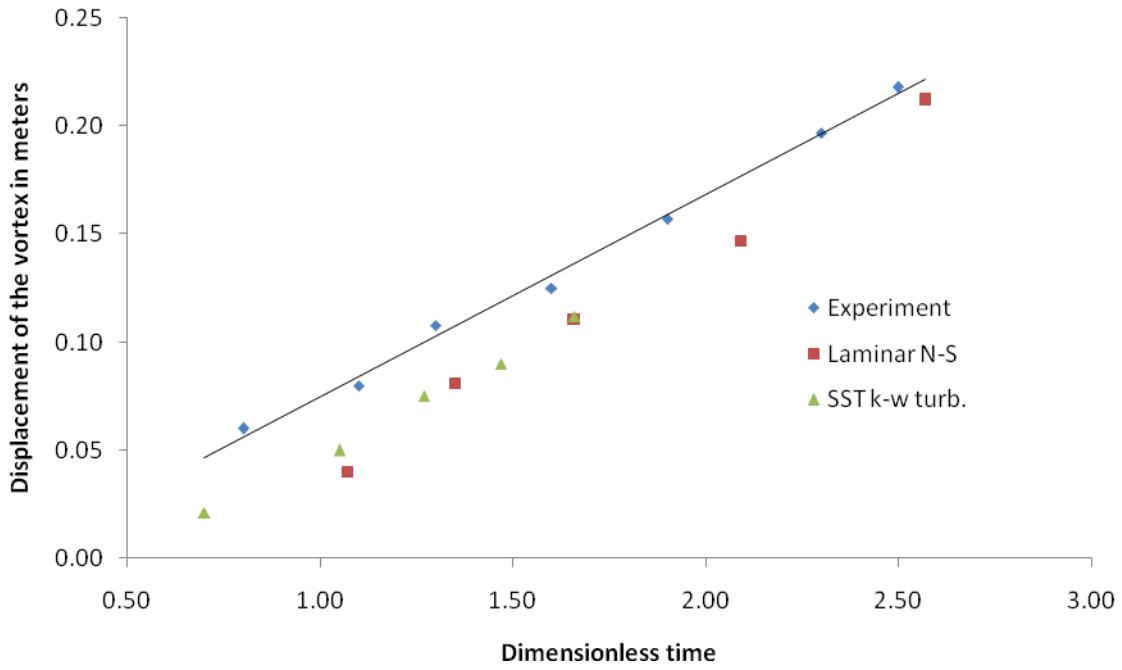

Figure 4.7: The displacement of the vortex with time

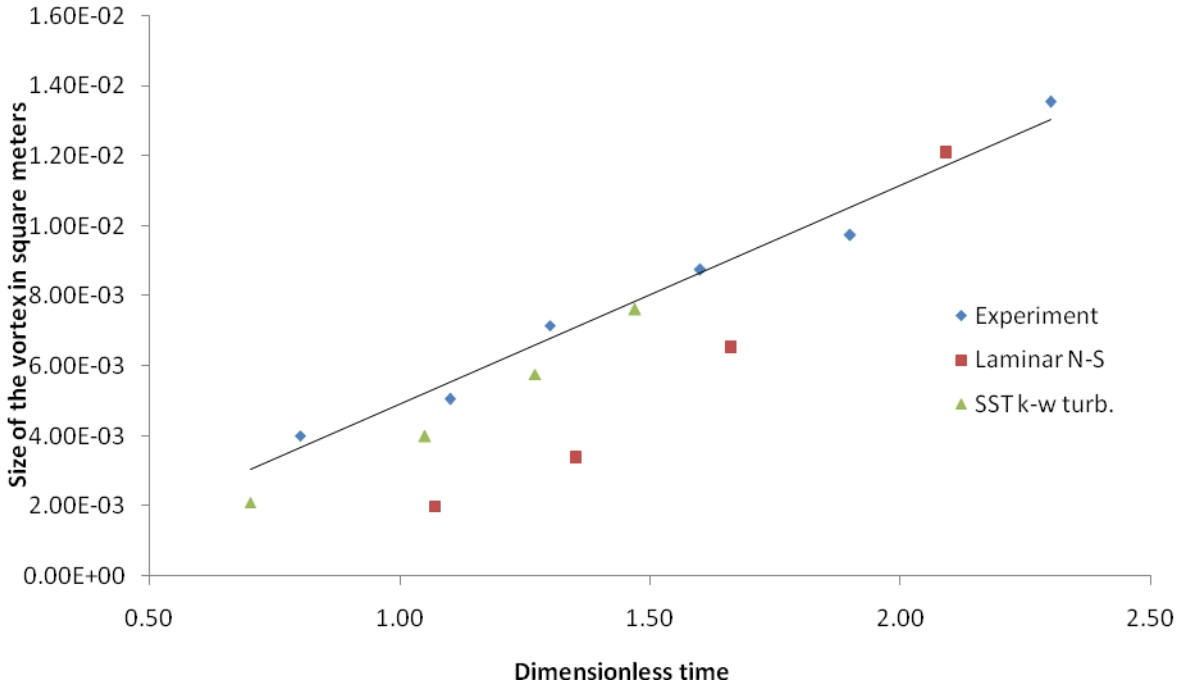

Figure 4.8: The change in size of the vortex with time

4.3.2 30° corner wall

Figure 4.9 shows comparative numerical and experimental images for the diffraction of an incident shock (M_s = 1.5) over a 30° wall at the same time scale. The dominant flow features were clearly identified in both the numerical and experimental images, prominent among these features are: lambda shocks that form above the shear layer, the shear layer is not smooth and flow instabilities appeared under the shear layer. The shear layer is terminated by a vortex that is affected by strong turbulent flow, and it continues to be distorted as it extends downstream. The turbulence intensity in the experimental picture is much higher than the numerical result showing that the real flow behaviour is under-predicted.

The shear layer could not retain its original shape due to strong instabilities that form around within the flow. The vortex and the shear layer break up into vortices and the flow is dominated by turbulence at later times. There is homogenous turbulent flow from the

corner that extends all over the wall surface. The primary flow features in the experimental picture are well replicated by the numerical images in terms of the shock patterns and the flow instability under the shear layer. However, the homogenous turbulent flow is not well predicted.

The pattern of propagation of lambda shocks in the numerical data is slightly different from experimental images. These shocks are not restricted to a particular portion but spread above the shear layer as shown in both experimental and numerical images of Figures 4.9&4.10. The formation of these lambda shocks has been observed by Law et al. [33] on multifaceted walls. However, the result of this earlier work is limited by the scale of the experiment. The present result shows that the shape of the lambda shocks has been affected by the breaking up of shear layer into vortices. This occurrence enhanced the development of a strong turbulent flow around the shear layer. There are more lambda shocks in the experimental pictures but not sharp as in numerical images. This may be attributed to the viscous effects in the numerical model. Law et al. [34] has shown that sharpening up and increase in the number of these lambda shocks can be achieved by reducing the dissipation in the numerical code used through decrease in viscosity.

The present investigation also shows that at large diffraction times the region far away from the corner could not sustain further propagation of these lambda shocks as shown in Figure 4.10e&f. This is due to the development of turbulent flow around the shear layer. The angle between the wall and the shear layer is similar in both numerical and experimental images especially during the early development of the flow. However, at long diffraction times there is a slight increase in this angle as shown in Figure 4.10e&f. The change in angle can be attributed to the strong turbulent flow that propagates back to the corner within the re-circulating flow behind the shear layer.

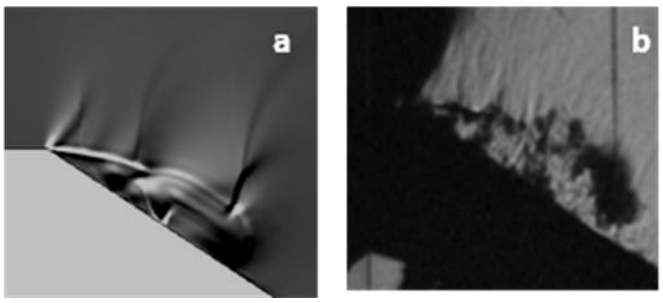

Figure 4.9: The evolution of the shear layer at Ms 1.5 incident shock on 30°corner (a) SST k-ω turbulence model (b) Experiment

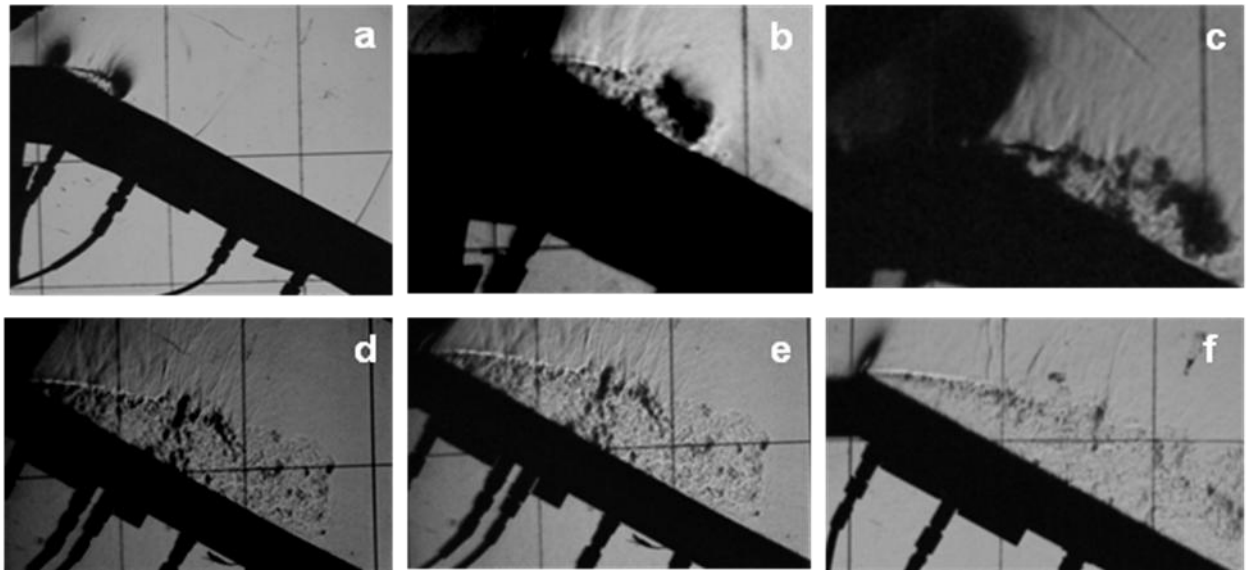

Figure 4.10: Development of homogenous turbulent flow at M_S 1.5 shock on 30° wall. Dimensionless time τ: (a) 0.2 (b) 0.4 (c) 0.6 (d) 0.9 (e) 1.11 (f) 1.55

Figure 4.11 shows the development of flow instability along the shear layer during the diffraction of an incident shock at Mach 1.34 on a 30° wall. The flow development starts with flow separation at the corner followed by the formation of flow features that could not be distinctly identified initially. These flow features becomes distinct after long times of the diffraction process. The shear layer that forms from the corner extends downstream with a vortex that has been affected by flow instabilities. The angle between the shear

layer and the wall surface is small compared to what is observed at high incident shock Mach numbers.

The flow instability is enhanced by further extension of the shear layer downstream. After long times of the flow development, the flow features become distinct showing turbulent breaking up of shear layer as illustrated in Figure 4.11c&d. The shear layer remains attached to the corner upstream as the instability develops further downstream. This observation shows that the flow development on a 30°corner wall at low Mach numbers occurs over different stages. The identification of this flow development is possible due to the scale of the experiment which allows for the diffraction of the incident shock over long times. There is also space for the visualization of the flow features behind the diffracting shock wave. The first two images (a&b) in Figure 4.11 are obtainable in conventionally sized shock tubes while the images (c&d) are only possible in a large scale shock tube facility.

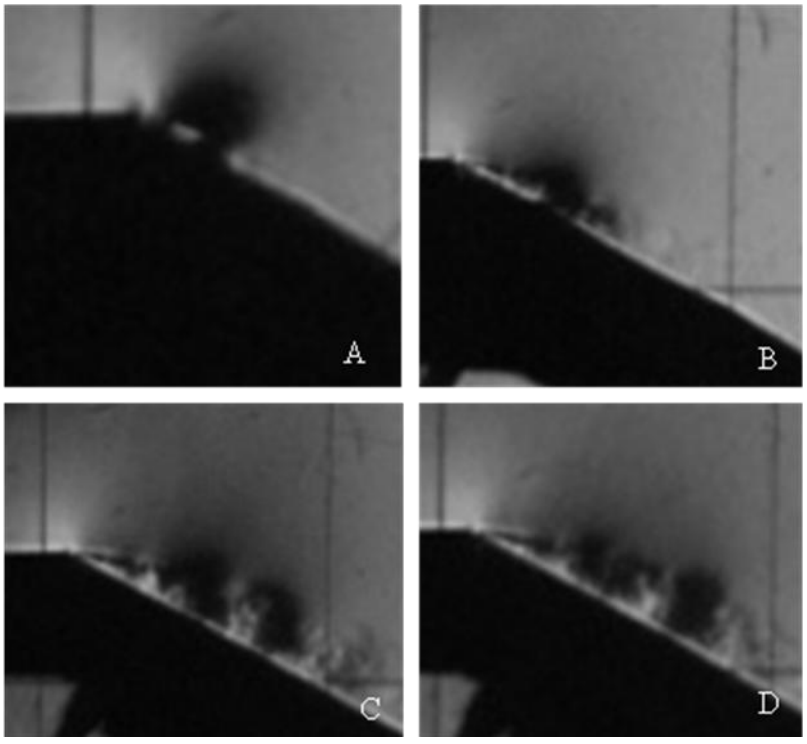

Figure 4.11: Turbulent break-up of shear layer at incident shock Ms 1.34
Dimensionless time τ: (a) 0.2 (b) 0.4 (c) 0.7 (d) 1.0

4.4 Low Mach number Incident Shock Wave on Curved Walls

Two curved walls (200mm and 400mm diameters) were initially considered for experiments over a range of incident shock Mach numbers 1.35 to 1.62. The final experimental analysis is based on the 200mm diameter wall because separation was not observed on the 400mm diameter wall for all the incident shock Mach numbers considered. The time scale used for the analysis is expressed in non–dimensional form as shown in equation (36).

$$\tau = \frac{at}{r} \tag{36}$$

where r is the characteristic length defined as radius of the curved wall, a is the speed of sound at an undisturbed location ahead of the incident shock wave and t is the time between the start of diffraction and the formation of the flow feature of interest.

Figure 4.12 shows the diffraction of an incident shock at Mach 1.5 on the 200mm diameter wall. The shock traverses the surface of the curved wall for sufficiently long time; about ten times the time scale of the conventionally sized shock tube experiments conducted by Skews [59]. Separation does not occur at the instant of the shock engaging the curvature but the boundary layer thickens. The increase in thickness of the boundary layer started from a region labelled BL as shown in Figure 4.13, and extends upstream even beyond the start of curvature. This is the same observation made by Skews[59] for a smaller radius and suggests possible separation of flow at later times.

Figure 4.13 shows the flow behaviour behind a Mach 1.5 incident shock on 200mm diameter wall at much later times. This observation is possible because the observation area in the test section of the shock tube is large enough for the shock to diffract for longer times. The change in boundary layer thickness becomes pronounced with further diffraction of the shock downstream. The flow behind the diffracting shock was monitored for the maximum time scale accommodated in the present shock tube. After a time scale of about 5.9 (Figure 4.12d) separation occurred. The separation phenomenon in this case was caused by the combined effects of adverse pressure gradient and the

impingement of weak shocks on the boundary layer. The induced separation evolved under the boundary layer with turbulent patches that spread downstream as shown in Figure 4.13e&f. A very important observation here is the movement of the separation point upstream towards the inlet. At longer times, series of reflected shocks were propagated at various regions that formed wedges, and these shocks interact with the flow. The analysis is limited to flow region that is free from these reflected shocks.

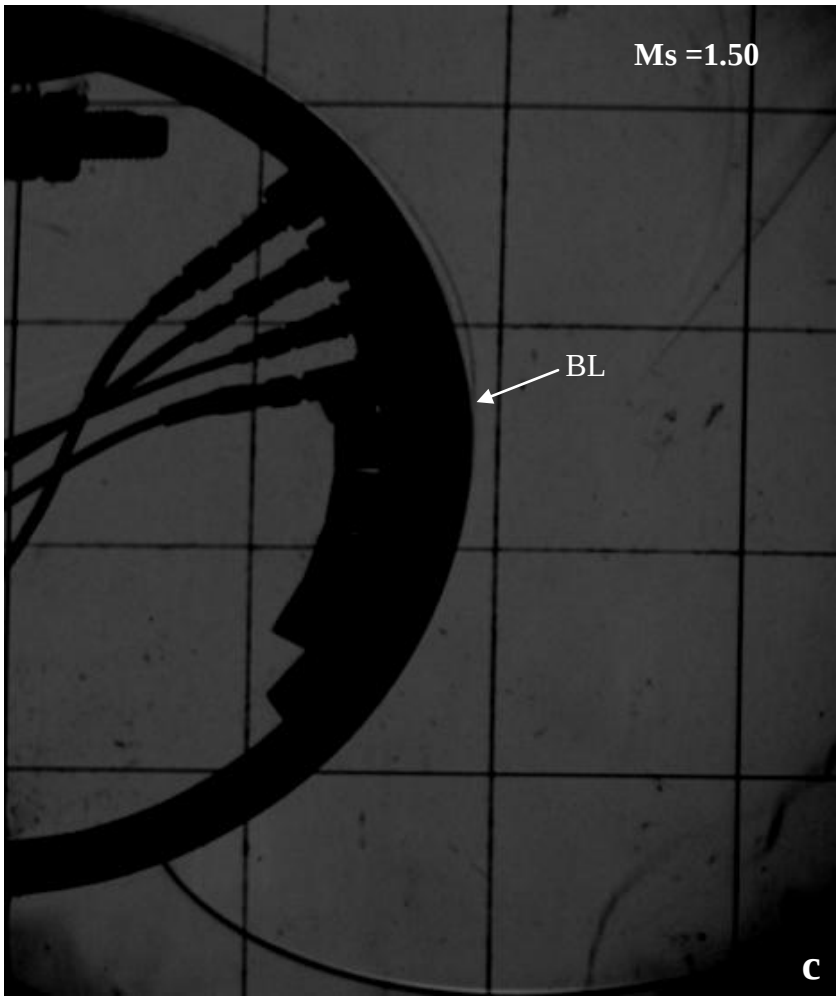

Figure 4.12: Increase in boundary layer thickness at incident shock Mach 1.5

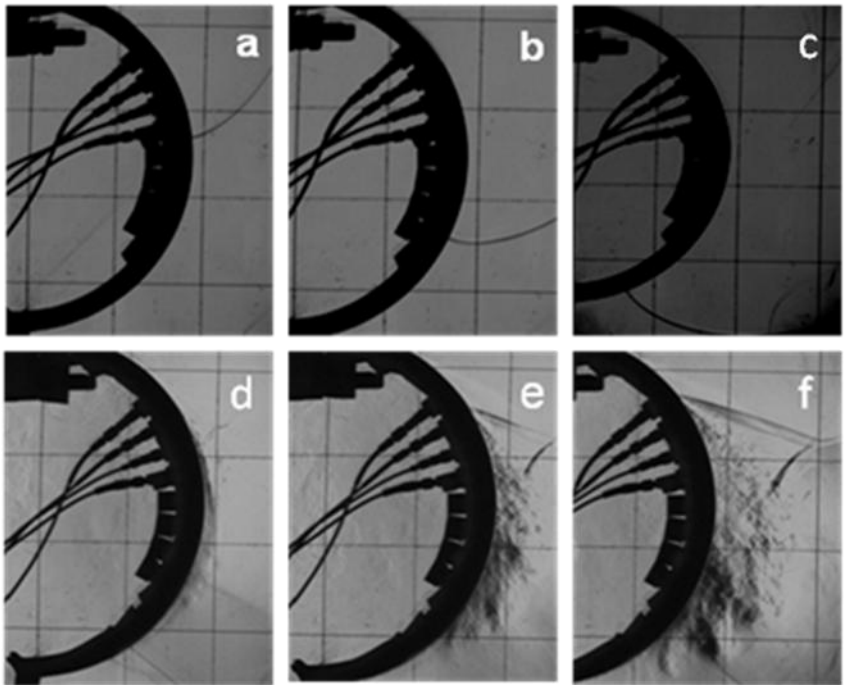

Figure 4.13: Diffraction of incident shock Ms 1.5 on a 200mm diameter wall
Dimensionless time scale τ: (a) 4.4 (b) 5.1 (c) 5.9 (d) 7.5 (e) 8.6 (f) 9.3

The diffraction of an incident shock Mach number 1.6 on a 200mm diameter wall is shown in Figure 4.14. The flow development within the perturbed region starts with an increase in boundary layer thickness from a point labelled H and extends upstream as shown in Figure 4.14a. This is followed by the formation of series of shocklets that impinges on the boundary layer as shown in Figure 4.14b. These shocklets coalesce into a shock wave at later times. The boundary layer in this case is assumed to be laminar since separation occurs shortly with further increase in boundary layer thickness upstream. The thickness of the subsonic flow region within the boundary layer increases and the velocity of the flow decreases in order to satisfy no-slip condition at the wall. The earlier work by Craig et al. [14] and Delery [16] on shock/boundary layer interaction shows that when a shock impinges on the boundary layer the Mach number decreases as it approaches the wall and disappears when reaching the sonic line. Information about the pressure rise within the subsonic region caused by the shock is sent upstream. This pressure increase upstream of the point where the shock impinges on the boundary layer causes the boundary layer to thicken.

The laminar boundary layer that forms is susceptible to separation due to its thickness. The combined effects of the impingement of the shock on boundary layer with the strong adverse pressure gradient cause the flow to separate from the wall as shown in Figure 4.14b&c. The unsteady fluctuation that engulfs the complex flow region is due to local change in flow Reynolds number around the region. It has been observed by Craig [15] that the impingement of a shock on a boundary layer can have an effect on transition. If the local Reynolds number around the region is very low, the boundary layer will remain laminar before and after the emanation of the reflected shock from the boundary layer. However, at a high Reynolds number the flow will be laminar before both separation and emanation of the reflected shock from the boundary layer, but reattach as a turbulent flow. Unsteady fluctuations may evolve upstream which may result in transition to turbulence since the subsonic portion of the laminar boundary layer is thicker.

Craig et al. [14] identified the cause of the disturbances at the downstream end of a nozzle and attributed it to separation cause by shock/boundary layer interaction. Some disturbances are found to propagate upstream about 100 boundary layer thicknesses. This important observation shows that a turbulent boundary layer which is unsteady can be generated. Figure 4.14d confirms these earlier observations.

The shear layer and an oblique shock emanate from the separation point and extend downstream with further diffraction of the shock. The formation of the shocklets indicates transonic flow which is due to the expansion fan within the region. Further increase in adverse pressure gradient motivates flow separation as shown in Figure 4.14c. A second shock (SS) is formed from the coalescing of the shocklets above the shear layer. The perturbed region behind the diffracting shock wave becomes complex due to the combination of the shear layer, oblique shock and second shock. The second shock changes to an upward facing shock with increase in strength as the complex flow regime moves away from the wall as illustrated in Figure 4.14d. A vortex is formed at the lower portion of the shear layer and this is pushed downstream by the extension of the shear layer.

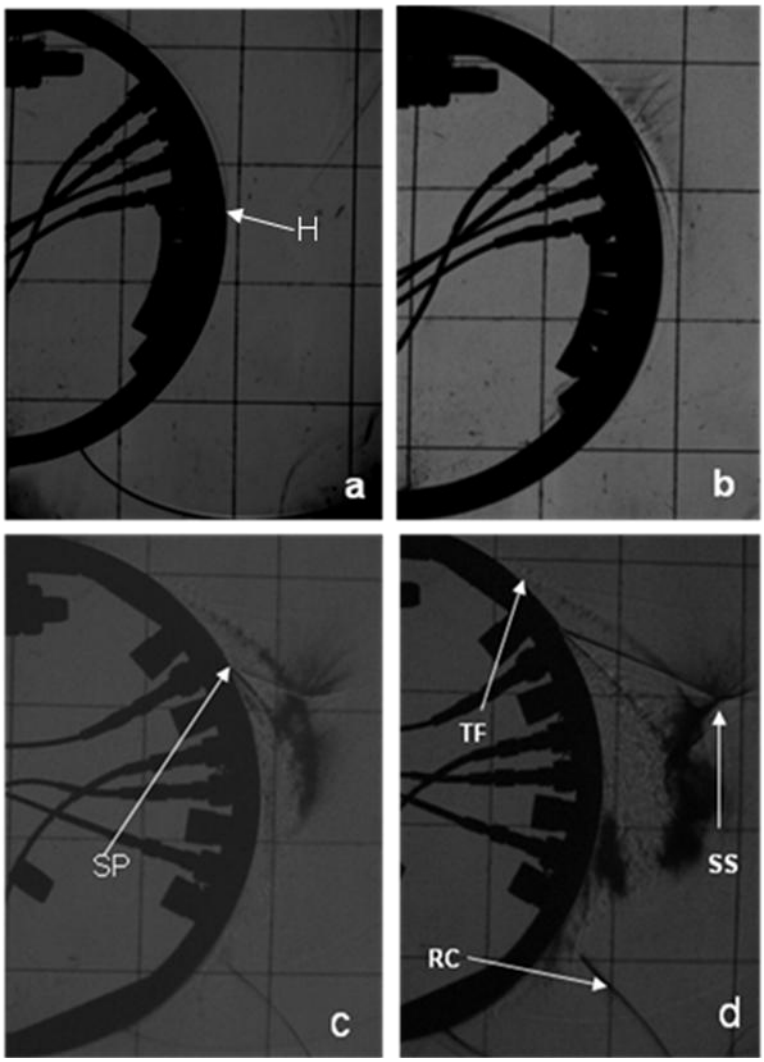

Figure 4.14: The flow features at Ms1.60 on 200mm diameter wall.
Time scale: (a) 0.52 (b) 0.62 (c) 0.76 (d) 0.96

The flow develops strong turbulent patches which extend up to point TF upstream and engulfs the entire complex flow region. A small portion of the second and oblique shock is not covered by the turbulent patches as shown in Figure 4.14d. This turbulent flow is a new flow feature that has not been observed before and is presumed to be 3-dimensional effect on the glass window of the test section. Two turbulent patches are identified; at region around the shear layer and at region downstream of the vortex. The turbulent patches near the wall extend downstream with time as shown in Figure 4.14c&d.

The vortex is formed at the lower extremity of the shear layer. The shape of this vortex has been affected and could not be distinctly identified due to the strong turbulent flow around the shear layer. It is important to note that the behaviour of this turbulent flow is different for Mach 1.5 incident shock. The turbulent patches extend downstream but are bounded by the shear layer upstream, and the complex flow region is not covered by the turbulent flow as observed at Mach 1.6. The observation of turbulent flow indicates the significant effects of the Reynolds number on the flow features behind the diffracting shock wave. Law et al. [33] investigated the effect of Reynolds number in high order accurate calculations with shock diffraction. A particular case of a 30° corner wall using the same mesh with different Reynolds number was investigated. The images obtained from the computation shows no significant change in the results between the Reynolds number 100000 and 200000. At Reynolds number 400000, degradation in flow feature resolution was observed. This degradation was due to the mesh being too coarse in that region. The code could not run at a high enough Reynolds number to capture the turbulence.

Figure 4.14d shows the beginning of interaction between the complex flow structure and the incoming reflected shock RC from the roof of the test section of the shock tube. This interaction is the limiting factor that determines both the maximum temporal and the spatial scale of the present experiment. A very important observation in the images for incident shock Mach number of 1.5 and 1.6 is that the upstream movement of the separation point is clearly identified at M_s = 1.5. However, at incident shock Mach number of 1.6 the movement of the separation point is small and it moves downstream as will be explained later using numerical data.

Figure 4.15 compares the experimental images with images obtained from numerical computations. The Mach number of the incident shock is 1.6 and the convex wall considered is 200mm diameter wall. The turbulence model replicates the experimental picture better than laminar solution, however the upstream turbulent flow is not well predicted. The turbulent patches that form along the wall downstream of the vortex is well replicated in the numerical images of SST k-ω turbulence model.

The three–shock configuration is observed in all the images however, the laminar Navier-Stokes shows multiple shock configurations above the shear layer with some instability under the shear layer. This observation confirms the earlier observation by Law et al. [32] which attributes the discrepancy between the Navier-Stokes solution and the experimental images to the instability in the finite volume method used by the numerical package. The SST-k-ω turbulence model shows a secondary vortex but this is not distinct in the experimental picture due to strong turbulent flow that engulfs the shear layer.

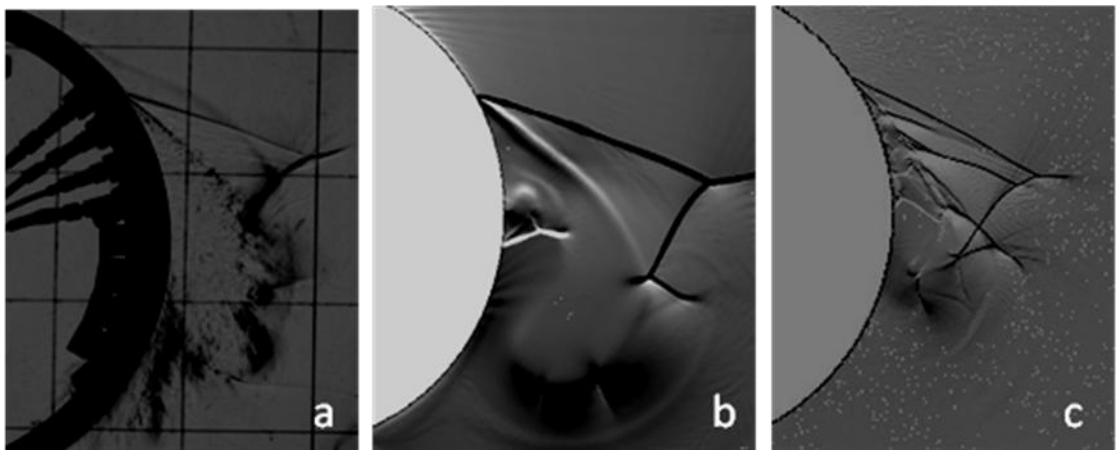

Figure 4.15: Comparison of the flow features behind an incident shock Ms 1.6 on 200mm diameter wall

(a) Experimental picture (b) SST k-ω turbulence model (c) Laminar Navier-Stokes

Figure 4.16 is the pressure flood plot for flow features at an incident shock Mach number of 1.6 on a 200mm diameter arc. The main vortex is shown at the lower end of the shear layer; the region under the shear layer is more influenced by the viscous effects due to its closeness to the wall. As the main vortex is moves downstream the secondary vortex is rotating in the opposite direction close to the wall. The formation of this vortex has been observed to be different from the way the main vortex is formed and is dependent on the strength of the incident shock wave. Other flow features such as a recompression shock, secondary shock and second shock have been explained comprehensively by earlier researchers (Kleine et al. [26] & Skews [58-60]).

The recompression shock matches the subsonic flow around the separation point with the flow under the main vortex. Secondary shock brings the flow around the main vortex to the same flow condition with the near wall flows. At low Mach number the near wall effect is sustained for long time. This is because the complex flow structure remains close to the wall. For high Mach number incident shocks the complex flow structure moves away quickly from the wall during the diffraction process.

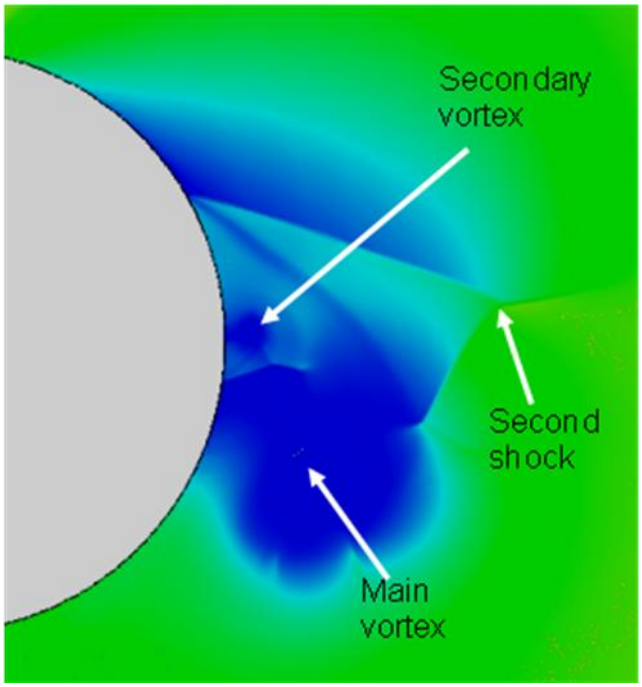

Figure 4.16: The pressure flood plot showing the secondary and main vortex (SST K-ω turbulence model at Ms 1.6)

Figure 4.17 shows the pressure contour for the transient development of a three–shock configuration, a recompression shock and a secondary shock. This observation was made behind the diffraction of an incident shock of Mach number 1.5 on a 400mm diameter wall. It is important to note that this result is obtained at later times after the shock has finished traversing the curvature. There is no separation at the instant of the shock diffracting on the curved wall. The diffraction process changes the orientation, the strength and shape of the incident shock. This process enhances the compression of the

gas behind the diffracted portion of the shock. The compression process is not uniform and this caused the propagation of different flow regimes behind the shock. The upstream gas expands while the gas particles close to the diffracted portion of the shock develop high pressure. A weak shock wave is propagated between the compressed and the expanding flow. This weak shock becomes a strong normal shock wave due to further diffraction of the shock downstream.

The shock is perturbed by a strong adverse pressure gradient near the wall and the flow separates from the wall as shown in Figure 4.17c. Earlier work by Delery [16] on shock wave/boundary layer interaction shows that a strong oblique shock that impinges on a boundary layer will cause boundary layer separation. Separation that occurs as shown in Figure 4.17b can be attributed to combining effects of an adverse pressure gradient and impingement of a strong shock wave on a boundary layer.

After the commencement of separation, the weak shock waves that propagate within the complex flow region at later times are identified as follows: an oblique shock wave that bring the expanded flow parallel to the shear layer, a second shock that matches the flow above the shear layer with the free stream flow far from the wall and a secondary shock on the surface of the main vortex. A recompression shock forms under the shear layer and matches the subsonic flow around the separation point with the flow under the vortex. The second shock is formed as a result of supersonic flow along the shear layer as earlier observed by Skews [59]. This shock has its foot on the vortex and forms a three shock configuration with the oblique shock as shown in Figure 4.17d.

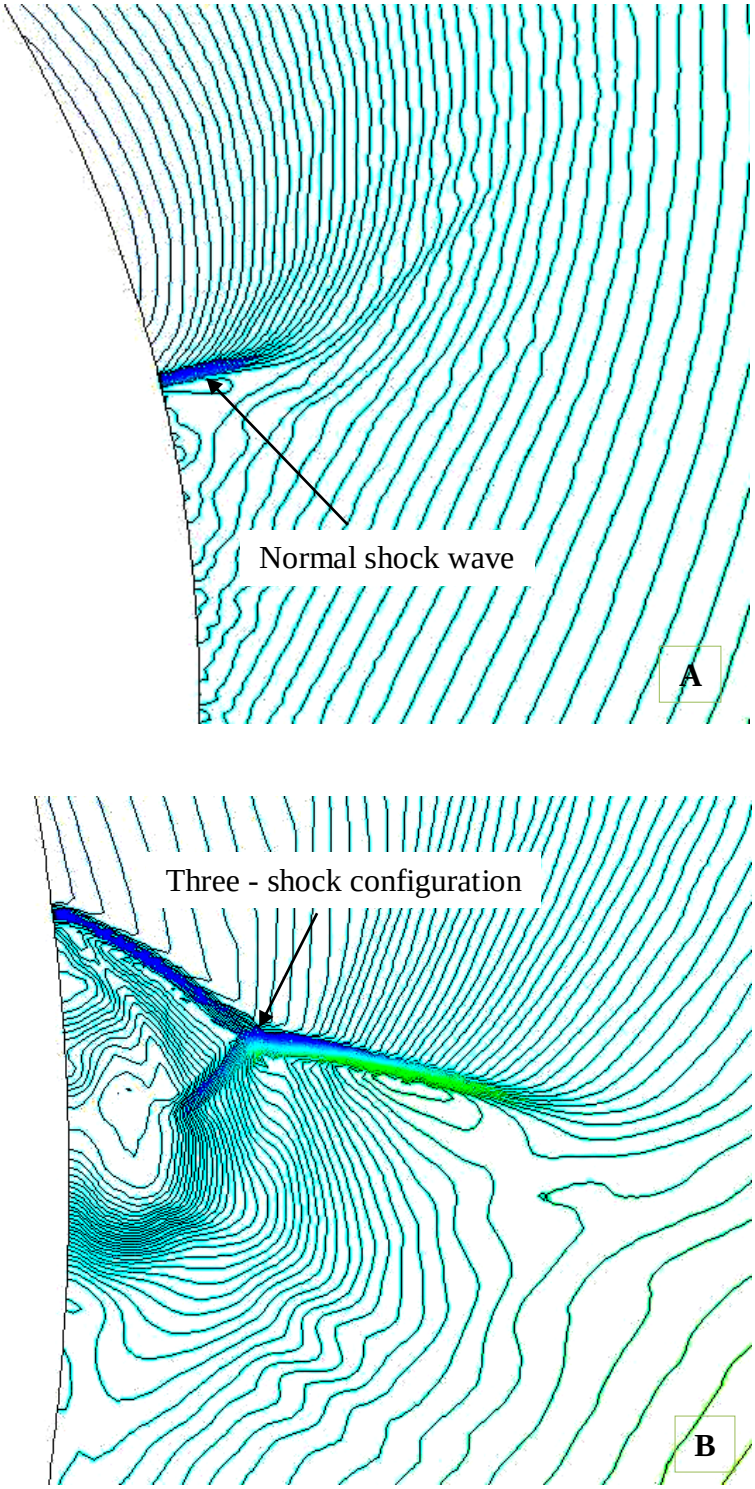

Figure 4.17: Transient development of a three-shock configuration at incidence shock Mach number 1.5 on a 400mm diameter wall

Dimensionless Time Scale τ: (a) 0.1 (b) 0.4 (c) 0.7 (d) 1.0

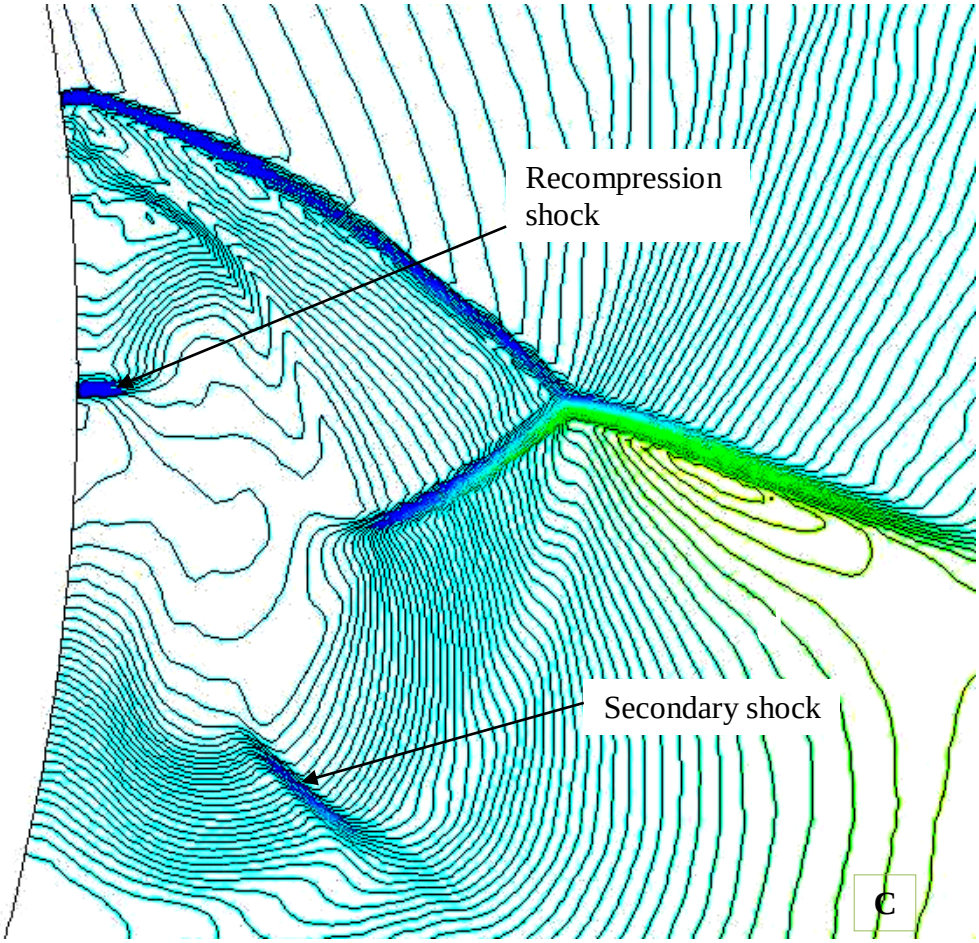

Figure 4.17 continued

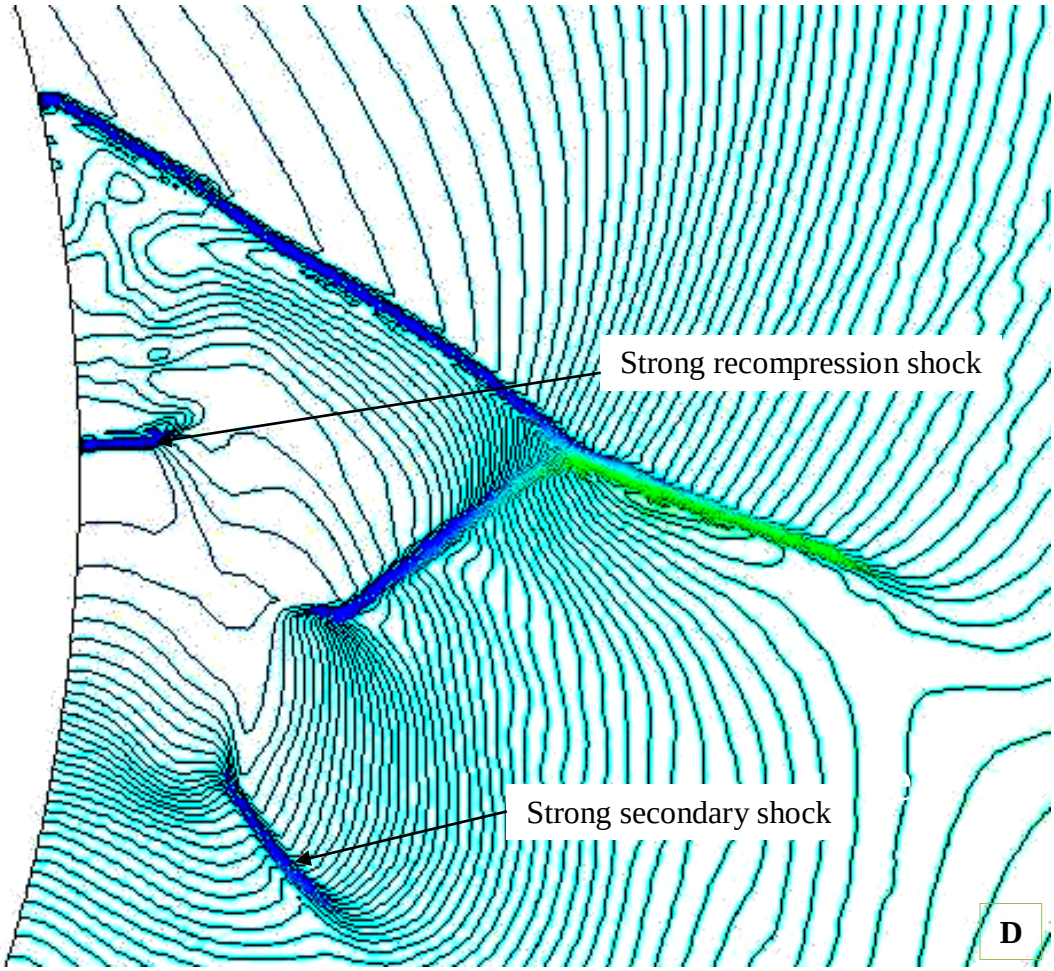

Figure 4.17 continued

4.5 Pressure Trace from Experimental and Numerical Analysis

The pressure traces are recorded by the oscilloscope and display by a hard disc data logger GL1000 Graphtec using hard disc data logger software version 1.0. The pressure traces for incident shocks M_S (1.33, 1.57, 1.51 and 1.40) as recorded by the machine before processing are shown in Figure 4.18. The colour blue, red, green and yellow represent the pressure traces for transducers at ports P_1, P_2, P_3 and P_4 respectively. The trigger is set at the first channel (CH1) which corresponds to port P_1. The sampling interval is 1µs, the abscissa is the time in seconds while the ordinate is the pressure which is recorded in volts. The voltage range for the graphs is between -0.5000 and +0.5000 over a time range of -0.8ms to 3.2ms, the system recorded voltage at 4000 data points.

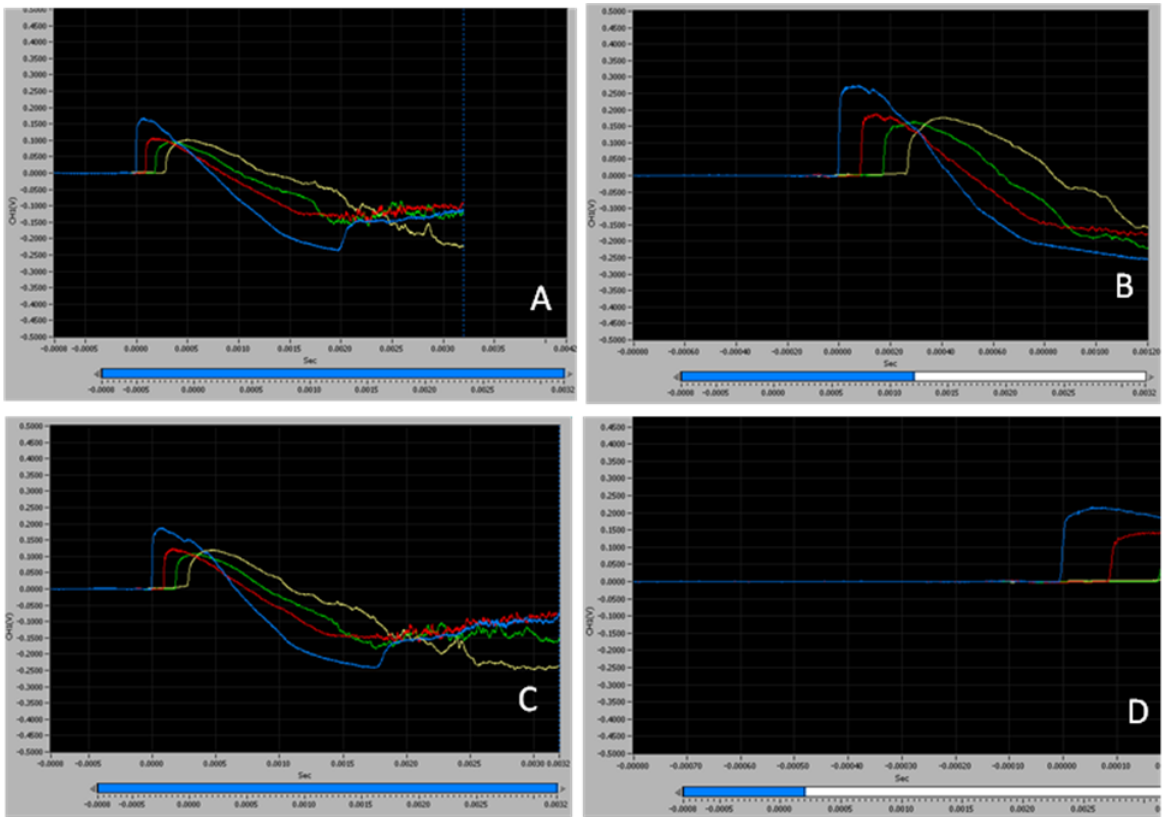

Figure 4.18: The pressure traces for incident shock M_s 1.33, 1.57, 1.51 and 1.40 over 200mm diameter wall.

The output voltage from the four ports is converted to pressure using equation (37) and the data are generated and plotted as shown Figure 4.19 - 4.21.

$$P_i = \frac{V_i \times 1000}{k} + P_0 \qquad (37)$$

where:

P_i is the absolute static pressure recorded at port P_i [kPa]

V_i is the voltage recorded by the transducer at P_i

k is the calibration constant of the transducer which is unique for each transducer [mV/kPa]

The static pressure is obtained by adding the ambient pressure P_1 to the gauge pressure. The present investigation is primarily interested in qualitative data, focussing on the trends rather than the actual values. The precise calibration of the transducers was thus not considered a priority.

Figure 4.19 shows the pressure history for the diffraction of an incident shock at Mach 1.57 over the 200mm diameter wall. The main pulse lasts for approximately 2μs, 5μs, 10μs and 20μs at ports P_1, P_2, P_3 and P_4 respectively. The shock travels about 1.07mm, 2.6mm, 5.37mm and 10.7mm respectively within these times. The shock traverses the face of the first transducer in about 10μs and the pressure history reveals rapid decay of the incident shock at the wall along the curvature. This is similar to the earlier observation by Skews [59] who noticed decreasing peak pressures on successive transducers.

The transducers recorded the maximum pressure of about 166kPa, 136kPa, 132kPa and 126kPa at ports P_1, P_2, P_3 and P_4 respectively. There is a small jump in pressure trace along the first and the second transducers (S) and this can be attributed to propagation of shocklets around this region. It is important to note that the trigger for the experimental pressure history is at CH1; hence this channel is used as the reference point for the analysis. For the numerical analysis Port P_1 is used as the reference point.

In Figure 4.19 the time range of about 4500μs shows long time history of the flow especially flow instability that could not be obtained in the conventional shock tube. The fluctuation along the pressure trace is used to identify the beginning of instability along the wall. The instability is first noticed at A on the transducer located at port $P_{2,}$ and extends to port P_3 (labelled B) after about 200μs. It spreads upstream and reaches port P1 after about 800μs (label C). Ports P_1 and P_3 are at the same distance from P_2, this implies that there is a significant difference between the rates at which the turbulent patches spread upstream compared to downstream. It is observed from the plot that the turbulent length scale around region P_2 and P_3 is higher compared to the upstream port P_1 and downstream port P_4. This shows that the turbulent flow does not evolve from the upstream or downstream of P_2 but at a region around it.

Direct comparison of both experimental and numerical pressure history with the transient development of pressure profile give the information about separation as shown in Figure 4.20. The analysis involves an incident shock M_s = 1.56 over a 200mm diameter wall. The separation point reaches port P_4 about 900μs after the shock leaves port P_1 as shown in Figure 4.20b. The separation point is labelled SP in both experimental and numerical pressure histories. There is about 5% variation in pressure at the point of separation in the numerical result compared to the experiment.

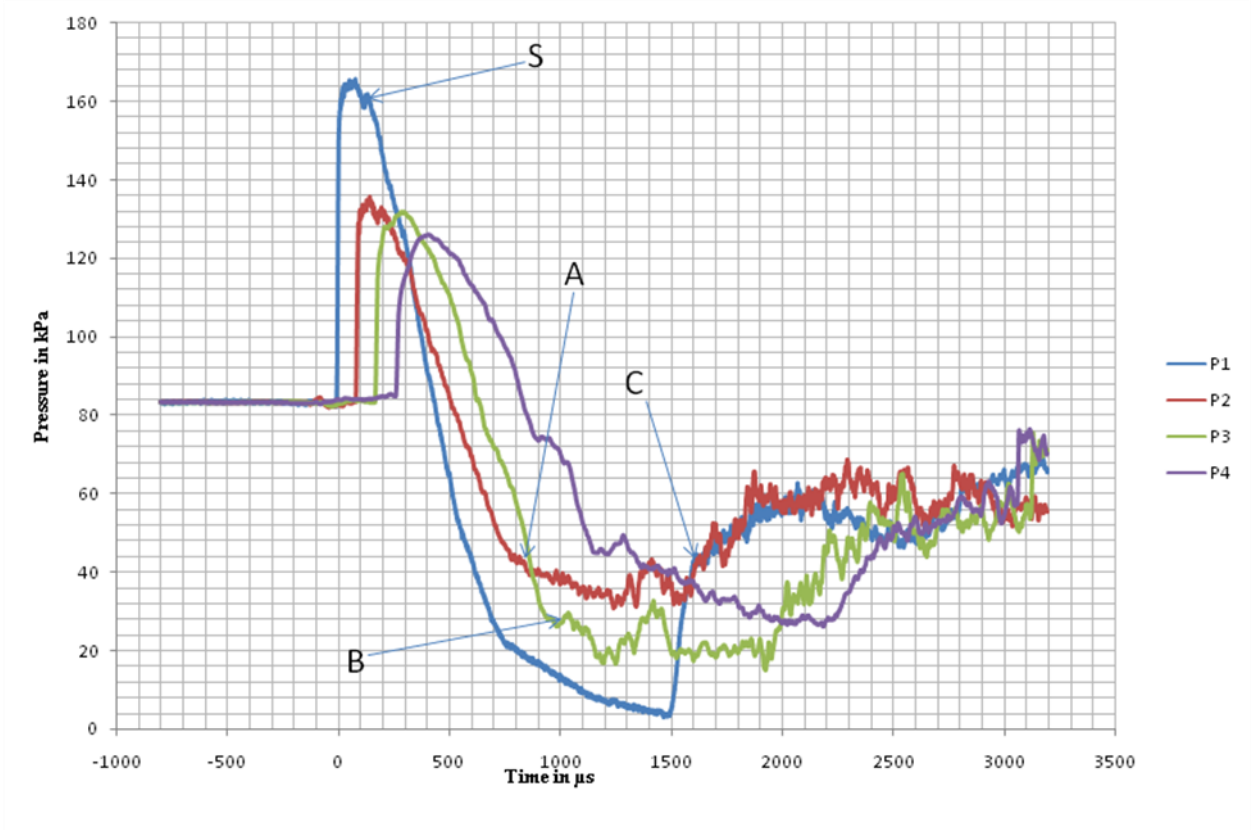

Figure 4.19: Pressure history for incident shock M_s 1.57 on 200mm diameter wall

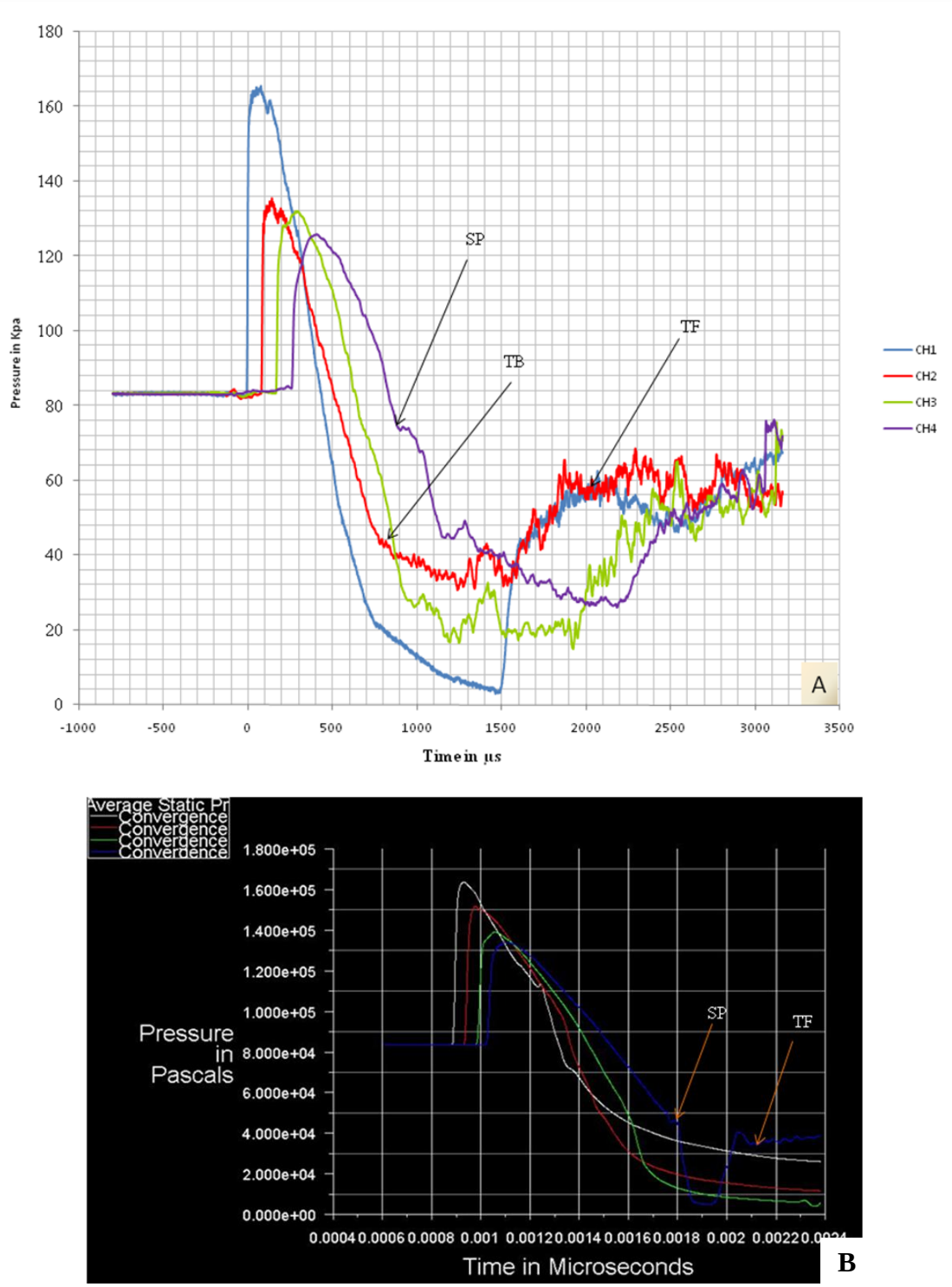

Figure 4.20: Experimental and numerical pressure history for incident shock M_s 1.56 on 200mm diameter wall

(A) Experimental result (B) Numerical result

Further analysis using incident shock Mach numbers 1.52 and 1.50 is shown in Figure 4.2. The separation point is not distinct within the time range of the analysis in plot A, however channel CH4 shows traces of separation at about 1380μs. Instability commences on the second and third transducers, however, further propagation of this instability is not captured because of the time scale of the graph.

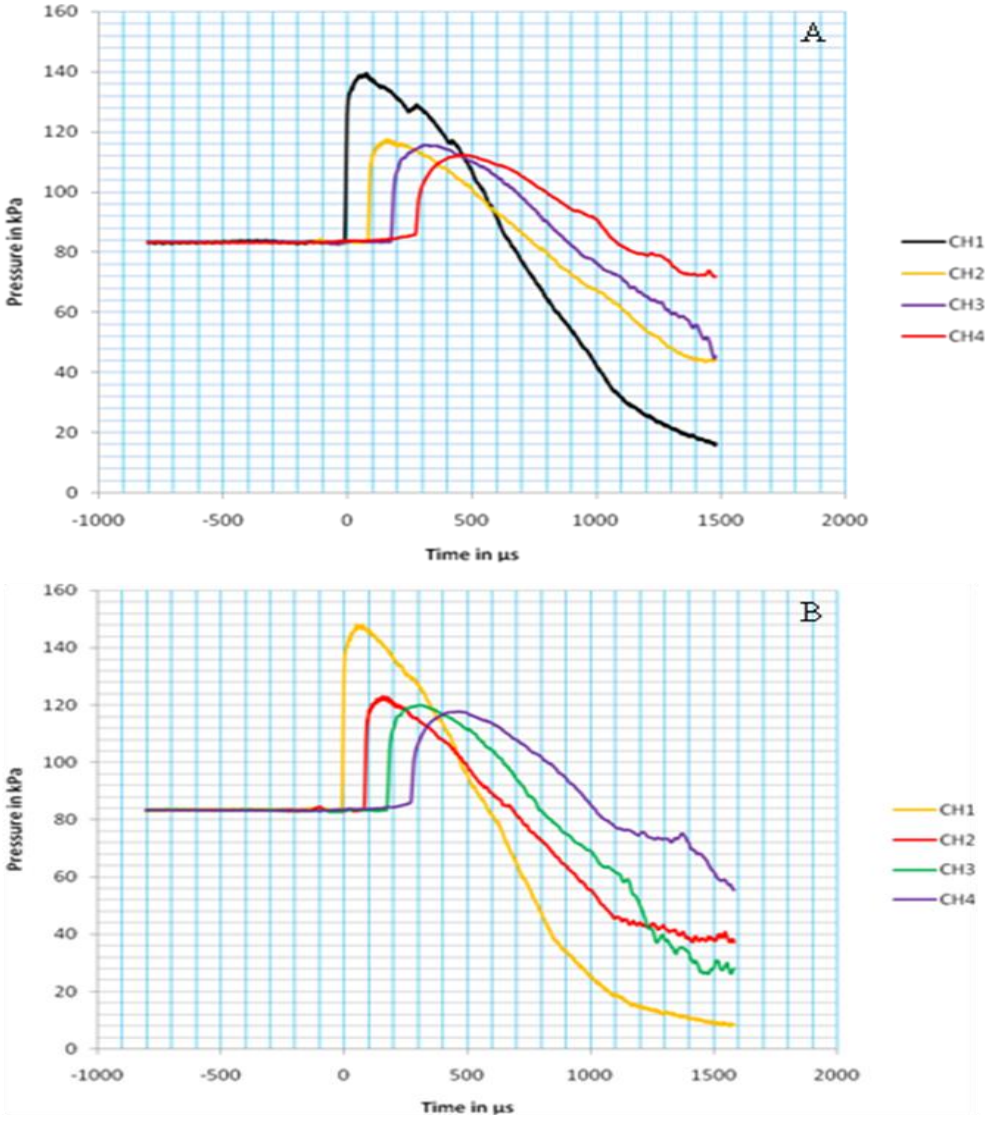

Figure 4.21: Experimental pressure history at incident shock M_s (1.50 & 1.52) on 200mm diameter wall

(A) M_s 1.50 (B) M_s 1.52

The summary of relevant data acquired from the pressure traces is presented in Table 4.1. The initial pressure in the driver section (IDP) is in the first column followed by the corresponding incident shock Mach number (M_s). M_s is calculated from the time taken by the planar shock to cover the distance between two transducers located at the inlet into the test section. The approximate Mach number of the wall shock is determined using the theoretical relationship between shock Mach number and the pressure ratio across the shock. This relationship is shown in equation (38).

$$M_s = \left(\frac{\gamma+1}{2\gamma}\left(\frac{P_2}{P_1}-1\right)+1\right)^{1/2} \tag{38}$$

where γ is the ratio of heat constants which is 1.4 for the present analysis, P_2 is the pressure behind the shock and P_1 is the pressure downstream of the shock. R_s is the port at which separation is first observed and T_f is the port that shows early development of instability.

Table 4.1: Data obtain from Pressure traces

IDP (kPa)	**M_s**	**M_{sP1}**	**M_{sP2}**	**M_{sP3}**	**M_{sP4}**	**R_s**	**T_f**
520	1.58	1.39	1.25	1.23	1.21	P_3 &P_4	P_2-P_4 &P_1
510	1.57	1.36	1.24	1.23	1.20	P_3 &P_4	P_2-P_4 &P_1
500	1.56	1.36	1.22	1.22	1.20	P_3 &P_4	P_2-P_4 &P_1
450	1.52	1.34	1.22	1.21	1.18	P_4	P_2 &P_3
400	1.51	1.26	1.22	1.19	1.16	-	P_2 &P_3
390	1.5	1.26	1.18	1.17	1.16	-	-
380	1.49	1.27	1.19	1.17	1.16	-	-
280	1.44	1.26	1.17	1.16	1.13	-	-
240	1.35	1.23	1.14	1.14	1.12	-	-

Figure 4.22 shows the behaviour of the wall shock for different incident shock Mach numbers. The pressure across the shock at each location is obtained from the pressure

history and the ambient pressure used is about 83.3kPa. Experimental measurement of the time spent between two consecutive ports is nearly the same. This shows that there is no significant difference in the speed of the shock across the transducer ports. The sharp difference in the strength of the wall shocks between port P_1 and other ports shows that the wall shock decays more rapidly within the first quadrant of the curved wall. The decay of the wall shock is evident also at other transducer locations as shown in the pressure history plots in Figures 4.19 – 4.21. A very important revelation in Figure 4.22 is that there is a significant difference in the decay of the wall shock between the first quadrant (CH 1) and downstream of the first quadrant (CH 2-4).

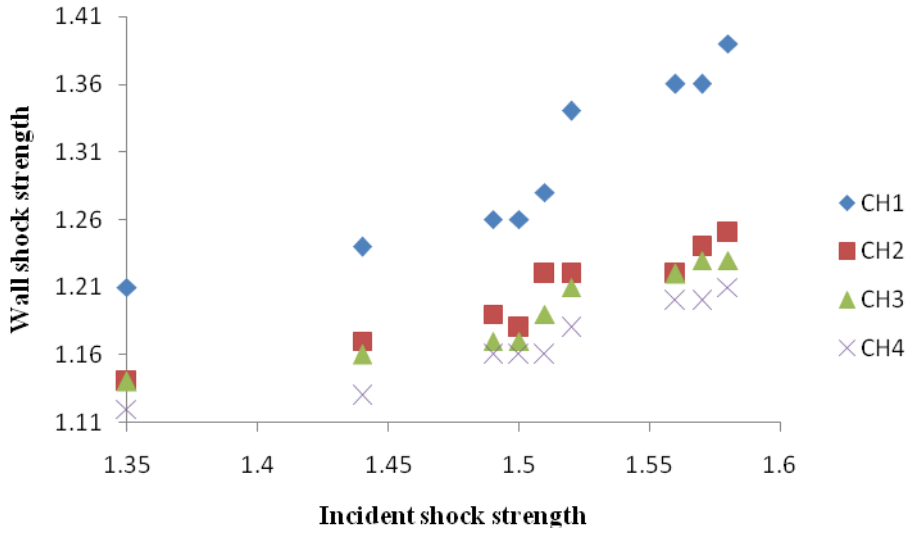

Figure 4.22: Behaviour of wall shock with change in incident shock Mach number

The above analysis is based on the assumption that a certain portion of the shock is perpendicular to the wall. This implies that the original incident shock is divided into three parts: the non-diffracted part, the diffracted part and the wall shock which is the portion of the shock that touched the wall.

5.0 HIGH MACH NUMBERS INCIDENT SHOCK WAVE

5.1 Introduction

Previous chapters shown that numerical methods applied are adequate for predicting the flow behaviour behind the diffracting shock wave. This chapter analyses the data obtained from simulations of the flow behind an incident shock with Mach numbers ranging between 2.0 and 3.0. The analysis involves only the numerical results as experiments could not be conducted at these Mach numbers in the current shock tube facility. Figures 5.1 shows a numerical result for the diffraction of an incident shock M_s = 3.0 on a 200mm diameter wall and two corner walls (30° and 90°). The important flow features behind the diffracting shock are shown as SH-Shear layer, OS-Oblique shock, SP-Separation point, CS-Contact surface, T-Triple point, SS-Secondary shear layer and DS-Diffracted shock.

The diffraction of an incident shock at Mach 3.0 on a 200mm diameter wall is shown in Figure 5.1A. The result gives a good replication of the earlier experimental result obtained by Skews [58] in a conventional shock tube of dimensions 51mm x 76mm. The complex flow structure behind the diffracting shock starts with an increase in boundary layer thickness as the diffraction process starts at the convex bend. Separation occurs when the adverse pressure gradient is strong enough to overcome the viscous force along the wall. A shear layer evolves from the wall at the separation point labelled SP in Figure 5.1A. The angle between the shear layer and the horizontal increases gradually as the diffraction process continues downstream.

The separation point is not fixed but moves along the wall with further development of the flow. The terminator that bounds the expansion fan changes to an oblique shock which motivates the formation of another shock described previously as a second shock by Skews [59]. It has been shown that the separation is delayed slightly by an increase in incident shock Mach number.

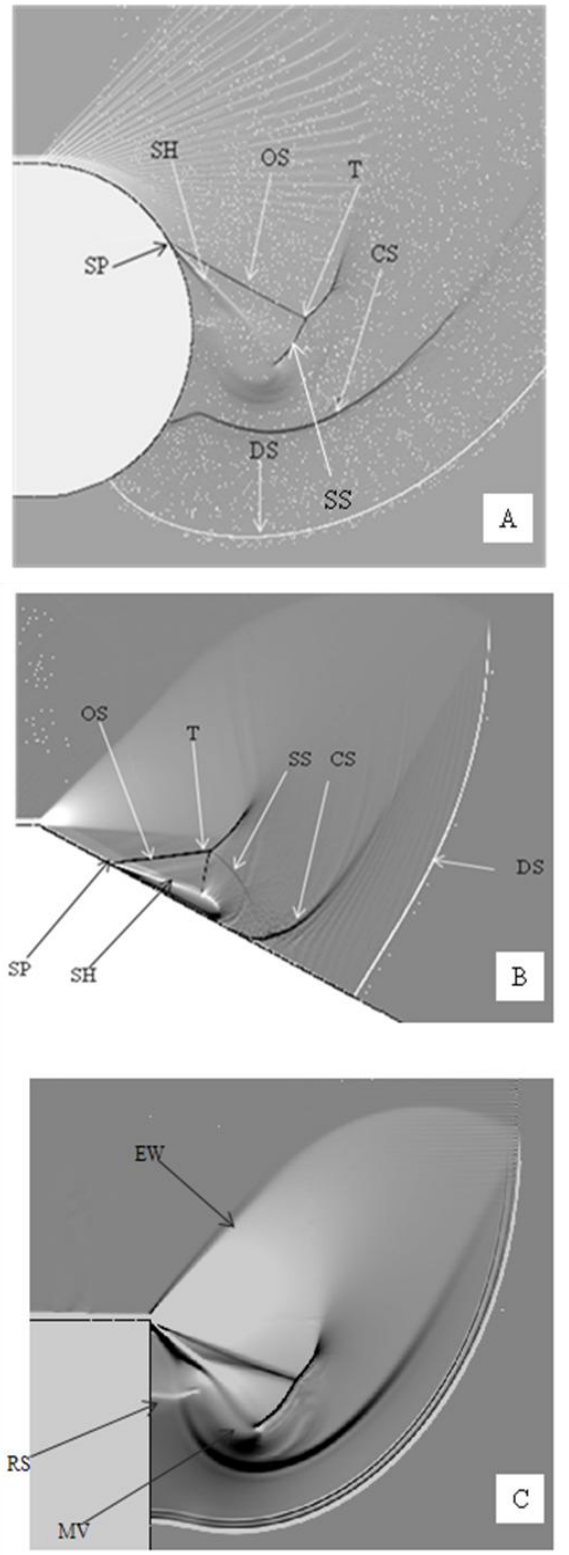

Figure 5.1: Flow features behind M_s 3.0 incident shock on convex walls (SST k-ω turbulence model) (A) 200mm diameter wall (B) 30° (C) 90°

Figure 5.2 shows the behaviour of the separation point with time at different incident shock Mach numbers. There is a significant difference in the movement of separation point for high Mach number incident shocks compared to low Mach numbers. Separation starts very late at low incident shock Mach numbers and the separation angle varies slightly with time especially for the case of $M_s = 1.6$. The comparison of $M_s = 1.5$ and $M_s = 1.6$ revealed that the separation angle at $M_s = 1.5$ decreases with time as shown in Figure 5.2 while it increases with time for $M_s \geq 1.6$. There is a transition Mach number between $M_s = 1.5$ and $M_s = 1.6$ at which the separation point does not move with time.

The angle of separation increases with time for high incident shock Mach numbers unlike low Mach numbers. There is similarity in the behaviour of the separation point at higher Mach numbers with a slight increase in velocity once the separation point is established. This observation may be due to increase in the velocity of the induced flow at higher incident shock Mach numbers.

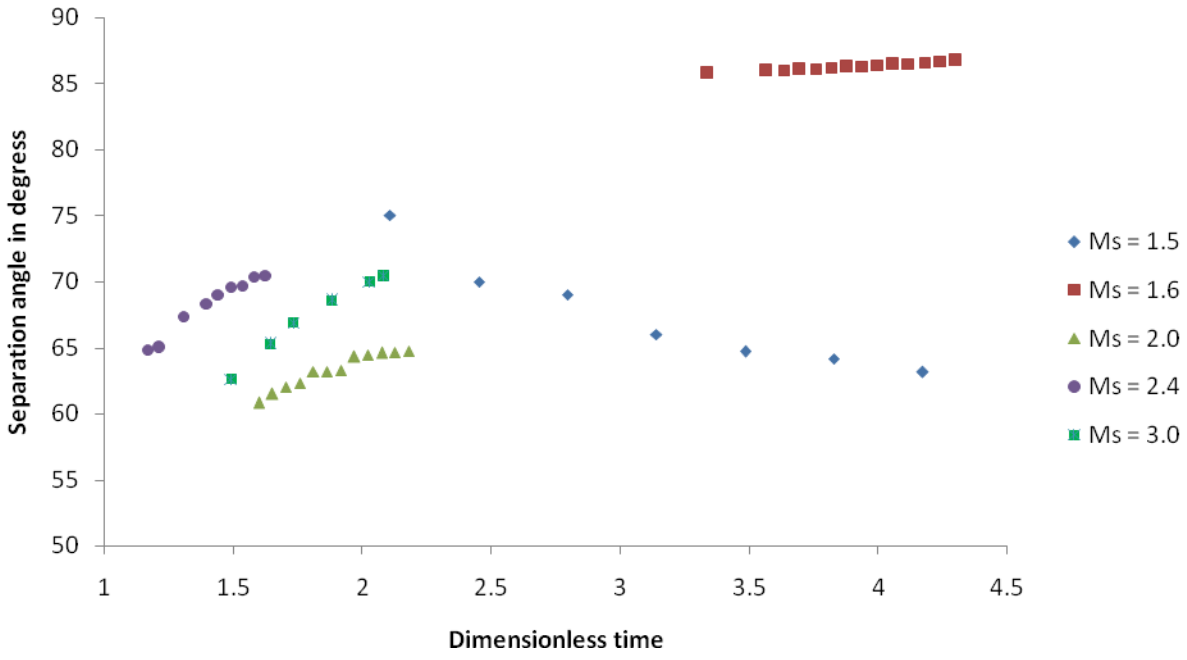

Figure 5.2: The change in separation angle with time on 400mm diameter wall

The behaviour of the separation point with circular walls of different radii is shown in Figure 5.3. The separation angle increases with time for all the curvatures but there is a significant difference in separation angle for small diameter walls compared to larger diameter walls. The behaviour of the separation point tends to become independent of curvature as the radius increases. This implies that the movement of the separation point will be independent of wall radius for an incident shock with high Mach number diffracting on a large diameter wall. This is evident by the collapse of the separation lines on 300, 400 and 500mm diameter walls as shown in Figure 5.3.

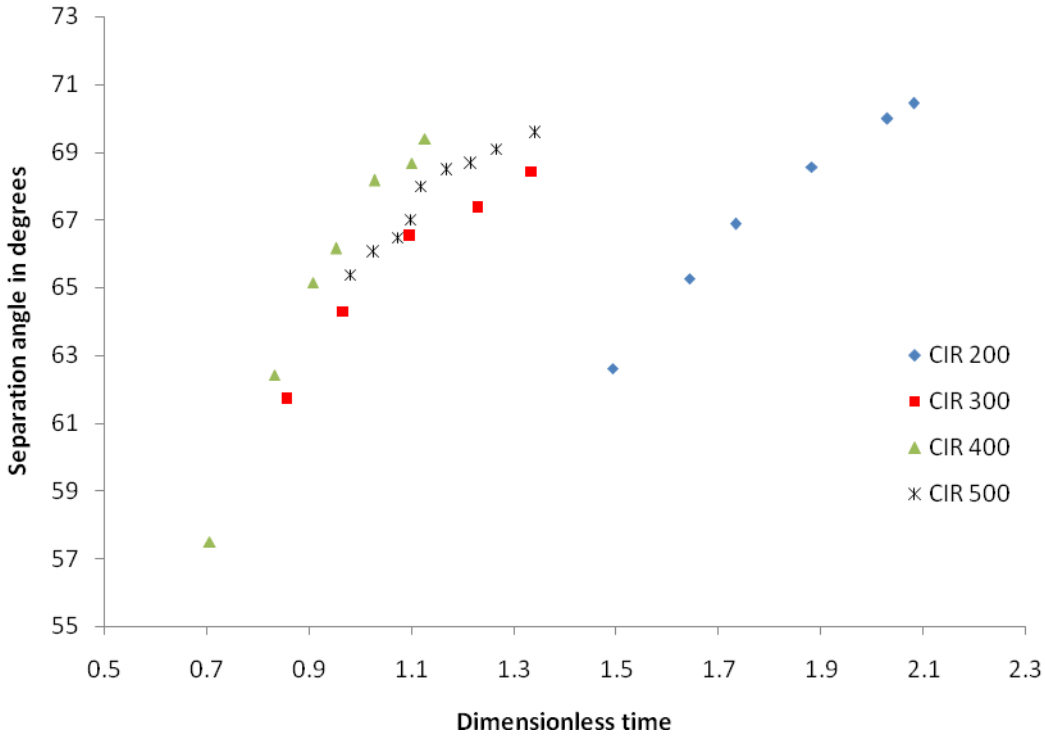

Figure 5.3: Effect of wall curvature on the movement of separation point at incident shock Mach number 3.0

The effect of the incident shock Mach number on the shear angle is shown in Figure 5.4. The shear angle increases with time but there is a significant difference in the behaviour at low Mach number compared to high Mach number incident shocks as illustrated by the M_s = 1.6 line in Figure 5.4. For high Mach number incident shocks the flow behind the shock is supersonic while the flow is subsonic at lower Mach numbers. The shear angle

increases substantially due to the increase in velocity of the flow as it separates from the wall surface. The angle approaches a constant value with time as the incident shock becomes stronger and this is expected since the maximum angle of deflection of the shear layer must be less than 90°.

Figure 5.5 shows the effect of curvature on the deflection of the shear layer from the wall at incident shock M_s = 3.0. The shear angle increases with time but is independent of curvature when the radius of curvature is above 200mm. At small radius the shear angle depends on radius of curvature and increases with time.

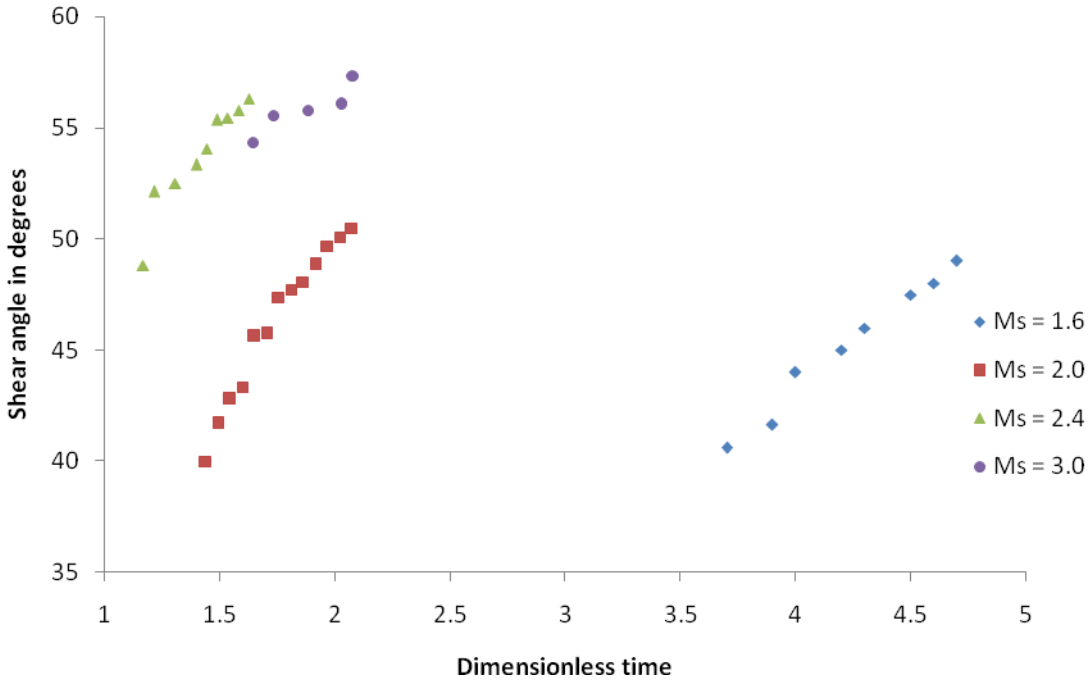

Figure 5.4: Effect of incident shock Mach number on the shear layer for the 400mm diameter wall

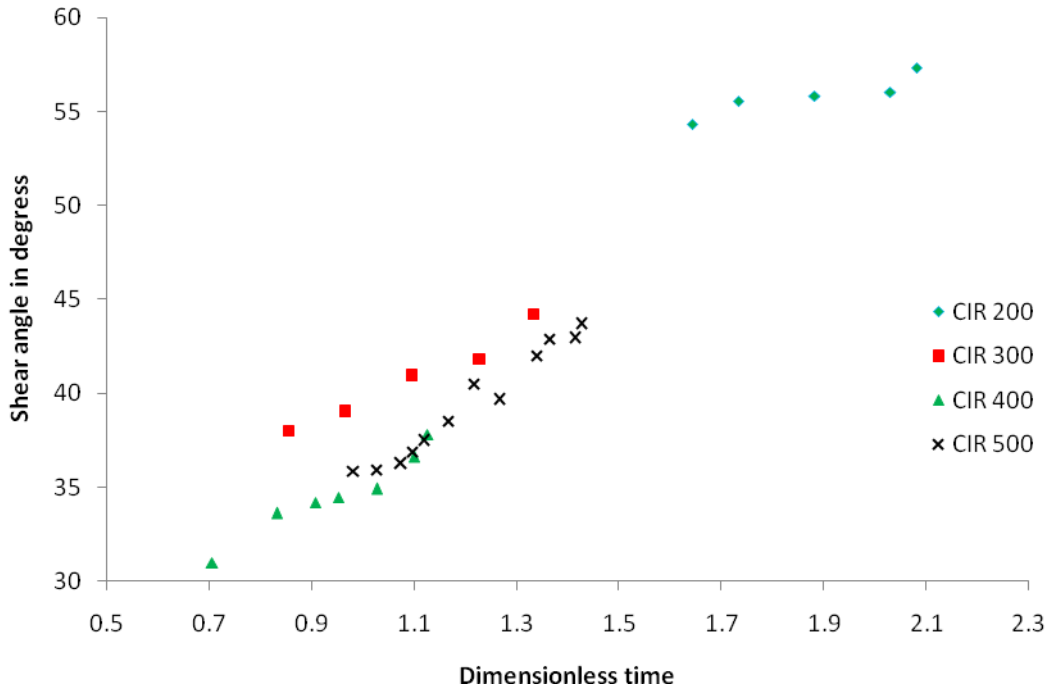

Figure 5.5: Effect of curvature on the shear layer for incident shock M_s = 3.0

A very important new observation at higher incident shock Mach number is the development of three shock configurations within the complex flow regime. The shock configuration is formed from the combination of the oblique shock with the two parts of the second shock labelled TP in Figure 5.1A. A secondary shear layer emanates from the junction of the three shock configuration and extends smoothly towards the wall and is pulled around the vortex as shown in Figure 5.1A. This secondary shear layer is a line of finite discontinuity of velocity and temperature and forms as a result of entropy inequality between the flows at the either side. The lower part of the second shock brought the flow exiting the region above the main shear layer parallel to the secondary shear layer.

These flow features are also evident in the numerical Euler and Navier - Stokes (with laminar boundary conditions) results as shown in Figure 5.6. This implies that the formation of these flow features is independent of viscosity and is pressure driven. However, the behaviour of the secondary shear layer is slightly different depending on

the solution. Euler result shows instability along the main and secondary shear layer (FI), and the Navier-Stokes (with laminar boundary conditions) result is characterised by a slight attenuation especially around the three shock configuration (FA). The kink that forms at the lower part of the contact surface is more pronounced in the Navier-Stokes (with laminar boundary conditions) model labelled CS in Figure 5.6C.

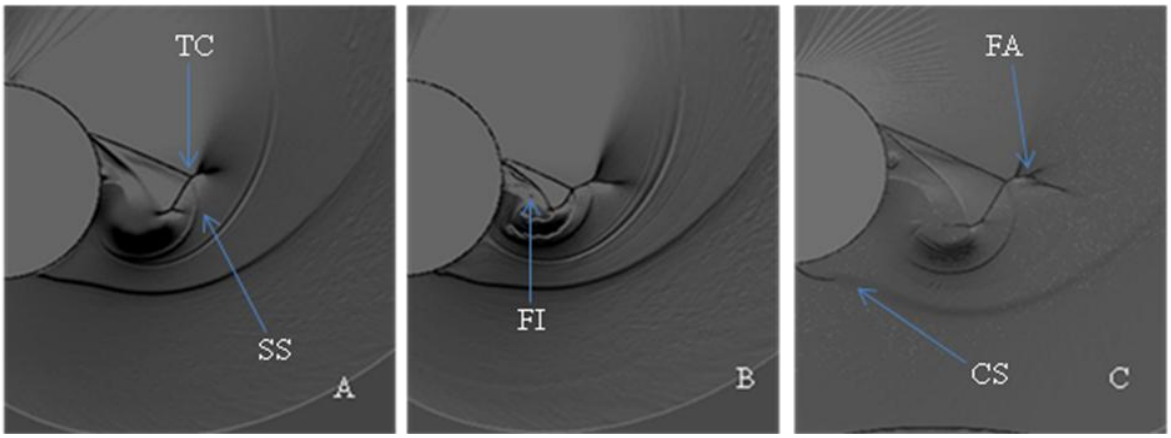

Figure 5.6: **The flow structure behind an incident shock M_s= 2.0 on a 200mm diameter wall (A) SST k-ω turb. model (B) Euler result (C) Navier-Stokes (Laminar boundary conditions)**

Figure 5.8 shows the transient development of two three-shock configurations at an incident shock Mach number of 2.0. The formation of this shock configuration follows the same pattern as at low incident shock Mach numbers except that two configurations are observed at higher Mach number. The upper configuration T_2 forms as a result of property gradients that arise among three different flow regimes. The flow regimes are free stream flow, locally supersonic flow that could not cross the oblique shock, and the flow crossing the upper part of the second shock as illustrated in Figure 5.7. The formation of the upper configuration precedes the lower configuration and it forms before the flow separates from the wall. The lower configuration forms from the lower portion of the second shock. The occurrence of these two three-shock configurations confirm the significant difference in the flow features behind the diffracting shock at low and high Mach number.

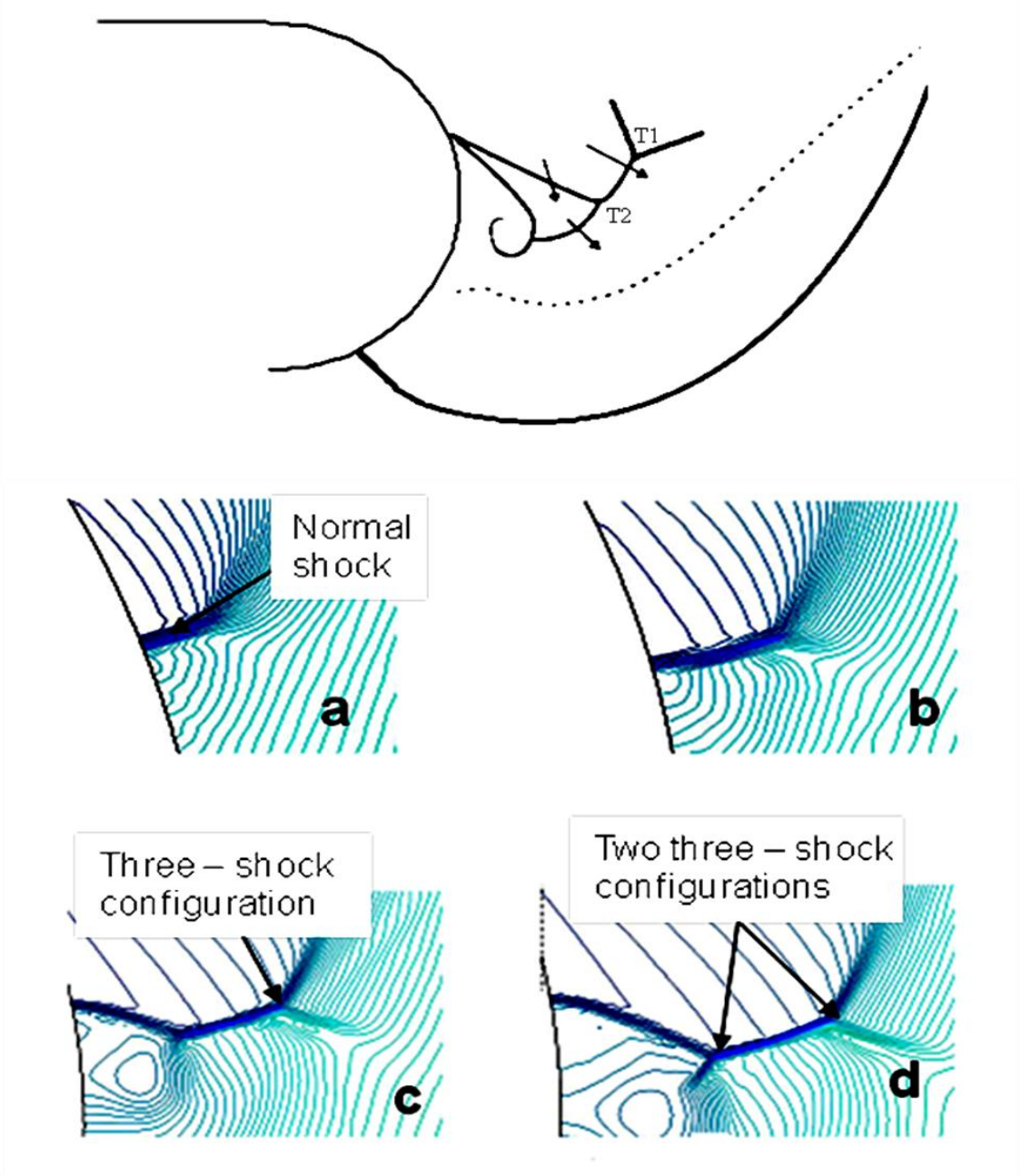

Figure 5.7: **Three-shock configurations at incident shock Ms 2.0 on a 200mm diameter wall**

Non-dimensional time τ: (a) 0.1 (b) 0.3 (c) 0.6 (d) 0.8

At higher Mach numbers the upper three-shock configuration fades away as the complex flow region moves away from the wall. The lower triple point becomes stronger and the

secondary shear layer becomes weak due to a reduction in the effect of the near wall on the flow.

The pattern of the propagation of the recompression shock under the main shear layer is different for low and high Mach number incident shocks. At lower Mach numbers the flow remains subsonic behind the diffracting shock and the pressure difference between the separating and the reattaching flow may not be high enough to generate a strong recompression shock. However, for higher Mach numbers there are significant pressure gradients that lead to the formation of a recompression shock as shown in Figure 5.8.

At higher Mach numbers the recompression shock appears earlier than at lower Mach numbers but the strength decreases as the flow develops further and it fades away at later times as shown in Figure 5.8d. The disappearance of this shock signifies decrease in the near wall effect on the flow under the shear layer as the complex flow region moves away from the wall surface. The effect of the proximity of the vortex on the recompression shock is reduced. The pressure gradient between the upstream separating flow and the downstream reattaching flow is not significant enough after long times of the diffraction process. Hence the final disappearance of the recompression shock.

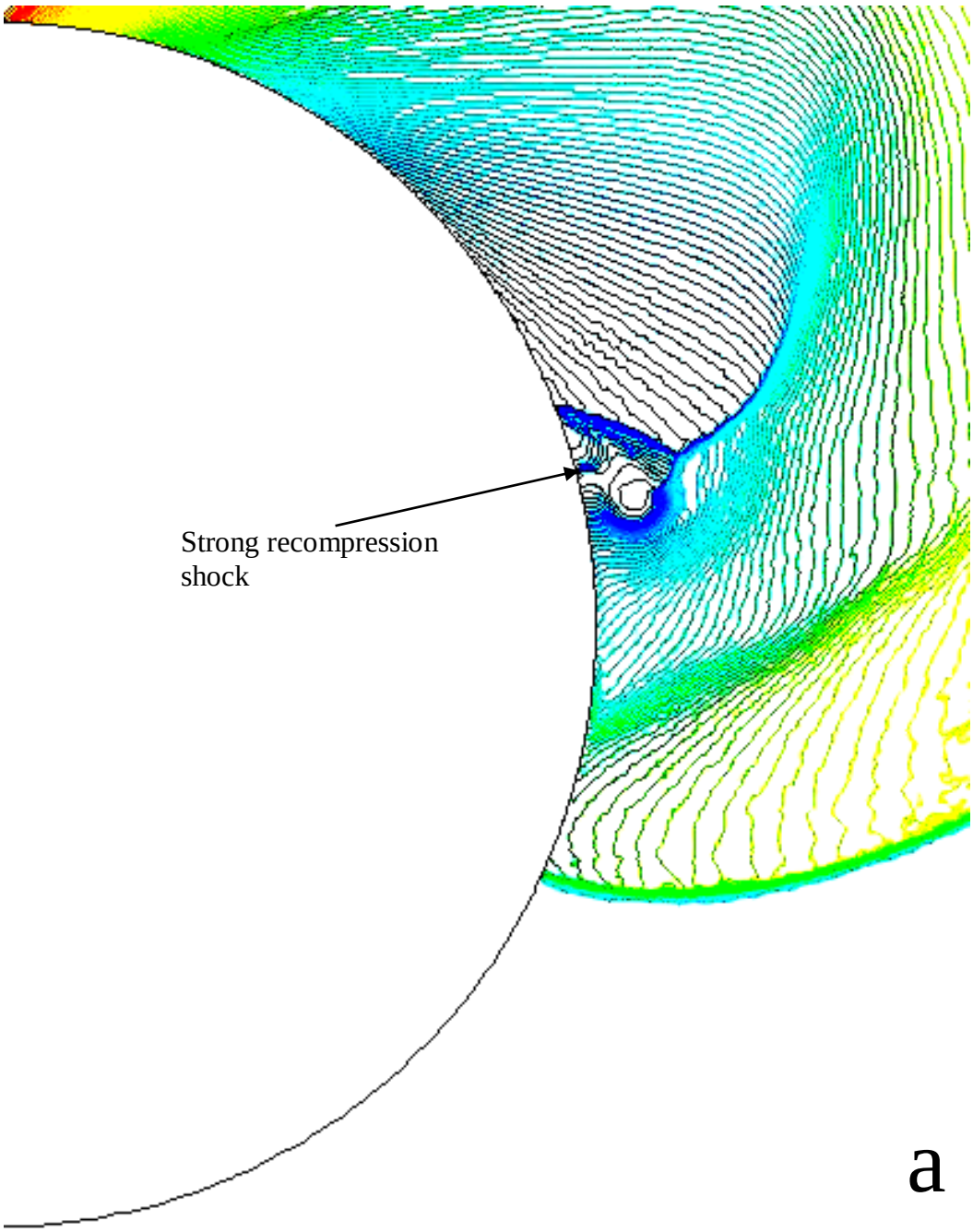

Figure 5.8: Transient development of recompression shock at incident shock Ms 3.0 on 400mm diameter wall.

Density contour at time T after the start of diffraction: (a) T = 785μs (b) T = 1079μs (c) T = 1344μs (d) T = 1485μs

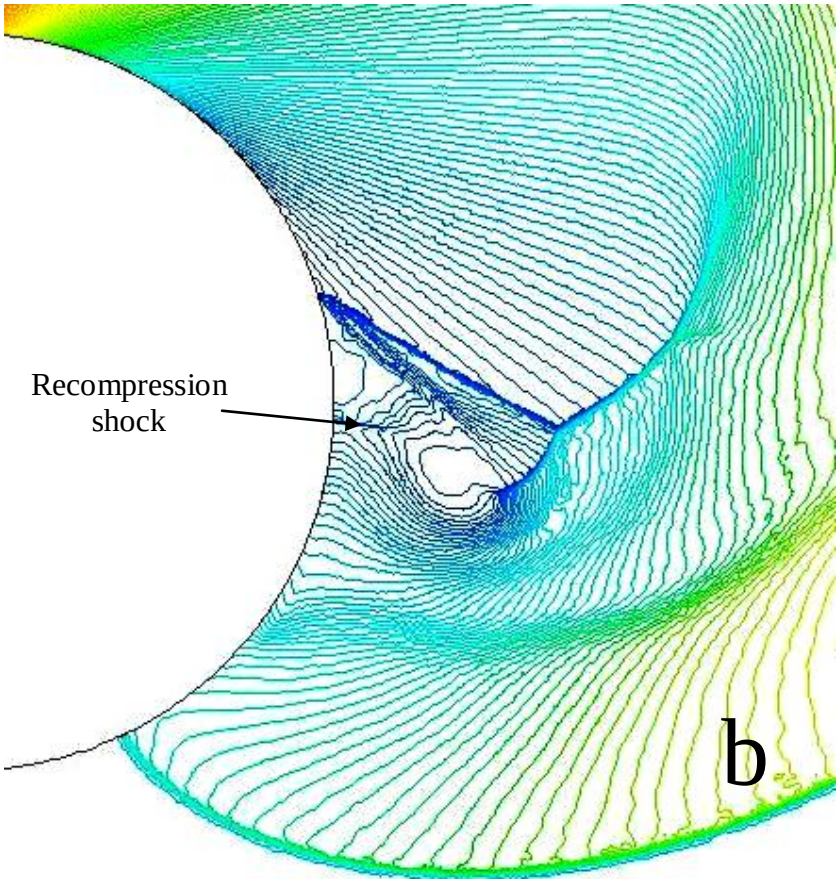

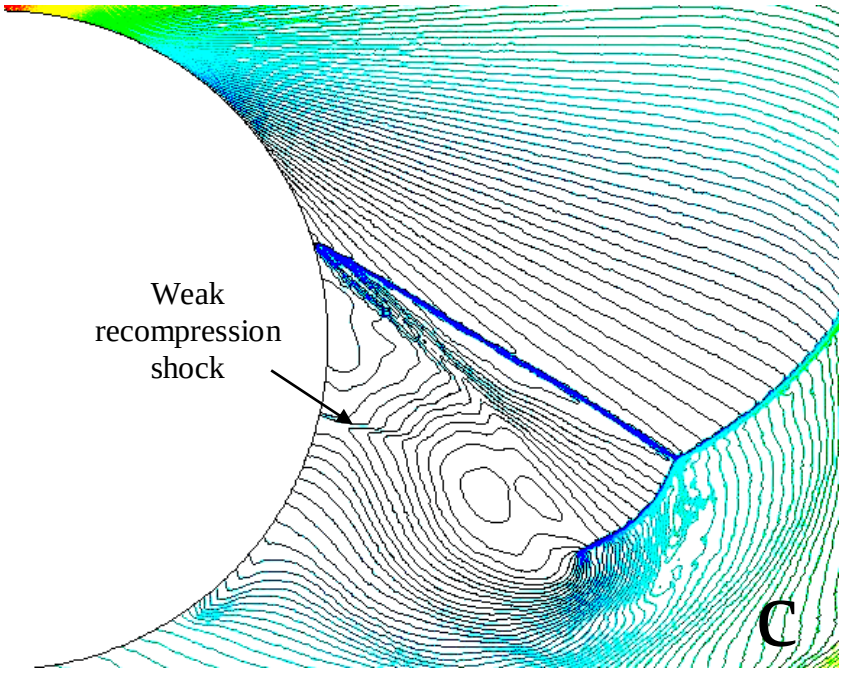

Figure 5.8 Continued

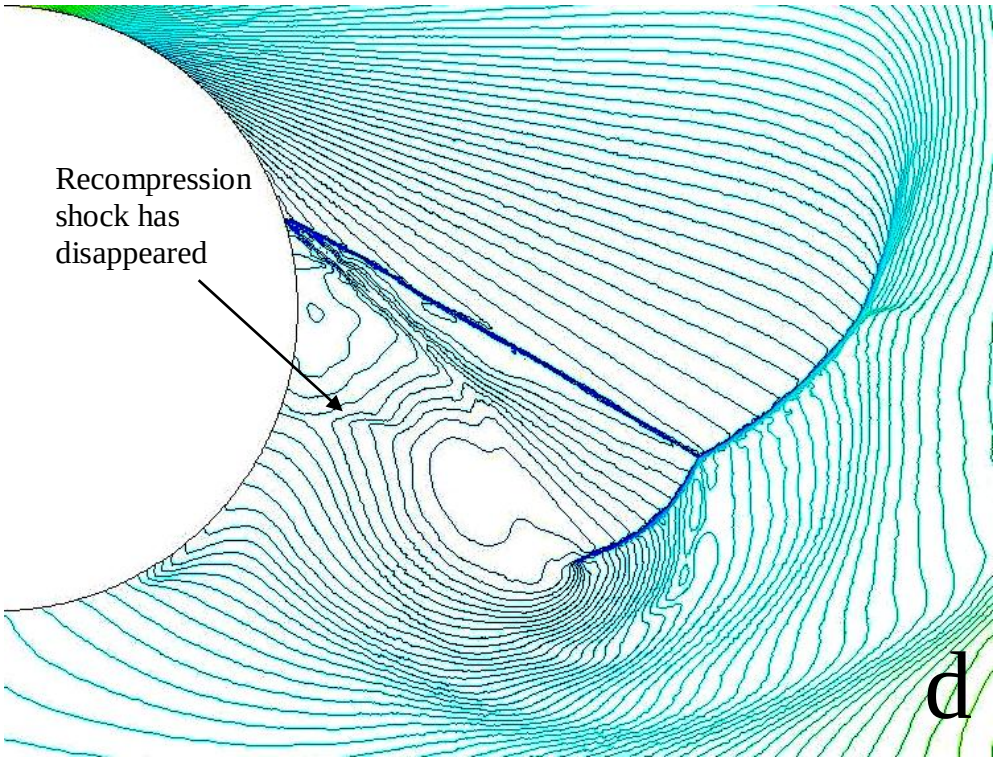

Figure 5.8 Continued

6.0 DISCUSSION OF RESULTS

6.1 Introduction

Earlier experimental analysis on shock wave diffraction revealed various flow features within the perturbed region behind a diffracted shock wave. However, the scale of the experiments did not allow for detailed analysis, hence the global flow behaviour could not be comprehensively explained. There are many flow features that appear in the present large scale experimental investigation which could not be seen clearly in the earlier works [58-60 & 32]. Notable among these features are:

- Flow instability along the shear layer followed by breaking up of the shear layer into vortices as illustrated in Figures 4.4 and 4.5.
- Formation of a series of lambda shocks above the shear layer with a region of turbulent flow underneath as shown in Figures 4.9
- Development of homogenous turbulent flow downstream of the 30° corner wall at later times as shown in Figure 4.10
- Confirmation of turbulent shear layer break-up on the 30° corner wall as illustrated in Figure 4.11.
- Confirmation of the significant difference in flow features between low and high Mach number incident shocks on curved walls (Figure 5.3&5.5)
- Discovery of the independence of the flow feature from the radius of curvature at high incident shock Mach numbers (Figures 5.4&5.6)
- Development of strong turbulent flow that engulfed the complex flow region on curved wall as shown in Figure 4.14.
- Observation of various flow features at low Mach numbers especially those that were observed at higher Mach numbers in conventional shock tubes.

The breaking up of the shear layer into vortices was described by Sun and Takayama [62] as follows: *"The rolling up of small vortices along a vortex sheet, which was reported in solving Euler's equation but never been observed in shock tube experiments, appears also*

in the solution of the 2-D Navier – Stokes equations, but may be suppressed by using a turbulence model. The numerical mechanism of the rolling-up in numerical simulation is still a controversial issue". The rolling up of small vortices along a vortex sheet has now been observed in several large scale experiments (see Figure 4.4). The scale of the present analysis is about ten times the scale of previous tests.

The flow development observed in the experiments follows a pattern similar to the numerical images except that the instability along the shear layer started earlier in the numerical computations with little dissipation, such as illustrated in Figure 4.3h&i. The experimental images show how the instability develops and breaks up into vortices, it then rolls up into a spiral vortex at later times (Figure 4.4).The rate of formation of the vortices along the shear layer is very low with the vortex moving away from the corner. The displacement of the vortex from the wall and the change in size of the vortex are compared as shown in Figures 4.6 - 4.8. The numerical result using SST k-ω turbulence model gives a good prediction of both displacement and change in size of the vortex with time.

The present investigation reveals that neither of the numerical models could give the exactly the same results as experiments. The laminar solution shows the early development of the instability with the break-up of shear layer into vortices, and rolling up of the shear layer into a spiral vortex. However, the rate of formation of vortices is over predicted due to a lack of dissipation. Further investigation using SST k-ω and k-ε turbulence models suppresses the vortices due to excess dissipation. The three models predicted the rest of the flow fields with adequate accuracy for the purpose of this study.

Sun and Takayama [62] has earlier observed the good agreement between the results of k-ε turbulence model and the results of the experiments conducted in the conventionally sized shock tube. However, the present results from large scale experiments show vortices that could not be captured in the previous tests. Comparison of the present results shows that there is good agreement between the images from experiment and the Navier-

Stokes (with laminar boundary conditions) in terms of the formation of vortices. Other models could not capture these vortices; the analysis suggests that the numerical dissipation in numerical codes (turbulence models) tends to be too high away from the wall.

The lambda shocks are formed along the shear layer indicating transonic flow around the corner as shown in Figure 4.4. A similar observation is made on a 30° corner wall, the lambda shocks are formed above the shear layer and spread downstream as shown in Figure 4.9. This implies that at the Mach number under consideration (1.5) the flow above the shear is transonic. There is strong flow instability under the shear layer which increases as the shear layer extends downstream. The flow develops further to turbulent flow as the shear layer breaks up into vortices. This turbulent behaviour shows the relevance of Reynolds number in the analysis of the flow features behind the diffracting shock on 30° corner wall. Law et al. [34] obtained a good prediction of the lambda shocks that form above the shear layer by considering the effects of the Reynolds number in the analysis of the shock diffraction.

Both experimental and numerical results for the diffraction of an incident shock at Mach 1.5 on a 200mm diameter wall confirmed that the flow does not separate at the instant of the shock engaging the curved surface. However, there is an increase in the thickness of the boundary layer starting from a point along the surface and extending upstream as shown in Figure 4.13. The flow separates later as shown in Figure 4.12 and the separation point is moving upstream contrary to what is observed at higher incident shock Mach numbers. Further analysis at an incident shock $M_s = 1.6$ is illustrated in Figure 4.14.

The separation of the flow is preceded by formation of shocklets at the region where the flow is locally transonic. Adverse pressure gradients develop downstream of this region due to the compression imposed by the diffracting shock as shown in Figure 6.1 (HPR is the high pressure region and LPR is the low pressure region, velocity rises at HVR while the flow at LVR moves at very low velocity). The shocklets impinge on the boundary

layer before later coalescing into a shock described as a second shock (Figure 4.14b). The flow separates from the wall when the adverse pressure gradient is strong enough to overcome the viscous force along the wall. A very important observation is the cause of separation of the flow at this low incident shock Mach number. Two factors are proposed base on the numerical and experimental images in Figure 4.14b and 6.1. The impingement of a weak shock wave on the boundary layer and the presence of an adverse pressure gradient at the wall. The weak shock wave becomes normal to the wall and is perturbed by the adverse pressure gradient as shown in Figure 4.17. The flow eventually separates from the wall with the normal shock becoming an oblique shock and a shear layer emanates from the separation point. The separation phenomenon in both circular wall and 30° corner wall cases are similar except that the vortex at the lower extremity of the shear layer is distinct for the curved wall. The expansion waves at the corner are centred for the corner walls with the lambda shocks spread over the shear layer. Unlike the 30° corner wall, for the curved wall the expansion waves are not centred at the start of curvature and the lambda shocks that form initially upstream of the separation point coalesce into a second shock.

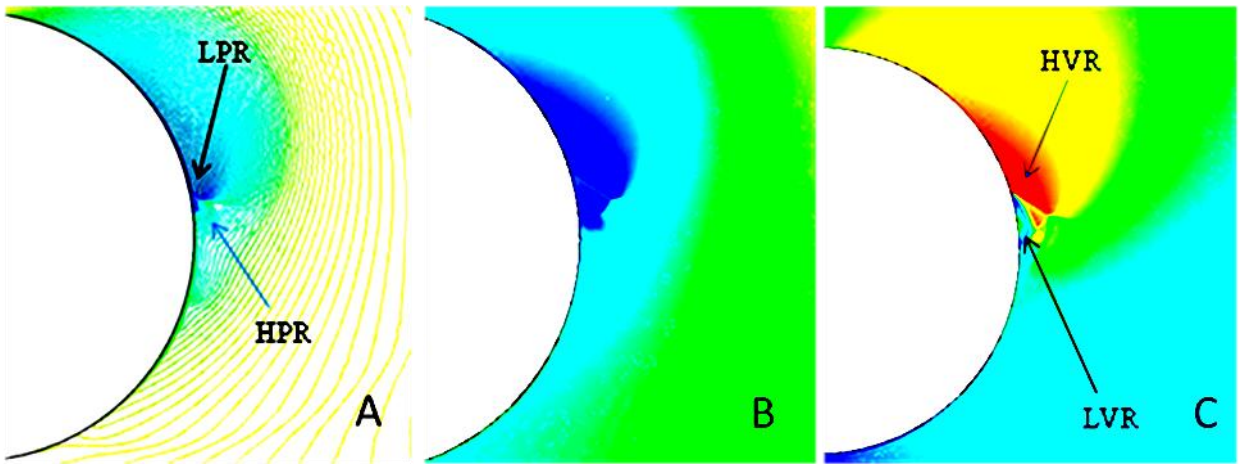

Figure 6.1: Separation behind an incident shock M_s 1.5 on a 200mm diameter wall (A) Density contour (B) Pressure flood (C) Velocity flood

The observations at high Mach number do not show the lambda shocks, this is because the flow behind the diffracting shock is supersonic and the complex flow region moves

away from the wall faster than at low Mach numbers. Separation at high Mach number is driven purely by the strong adverse pressure gradient and most of the flow features could be identified even at small diffraction time.

The result of the analyses shows that at high incident shock Mach numbers the radius of the curved wall does not significantly affect the separation point and the angle of the shear layer as shown in Figure 5.4&5.6. In contrast to this, at low incident shock Mach numbers, the movement of the separation point and the change in shear angle depend on the radius of curvature. The separation point varies inversely with time for M_s=1.5 as shown in Figure 5.2.

The significant difference in the behaviour of the flow behind the diffracting shock at low Mach numbers is proposed to be the result of near wall effects as shown in Figure 6.2. At high Mach numbers the complex flow region is far from the wall compared to low Mach numbers. The movement of the complex flow region from the wall reduces the near wall effects on the flow, hence the flow features that form as a result of viscous effects could not be observed. Among these features are the lambda shocks that form above the shear layer (Figure 6.2 B&C) and the bifurcated shock that interacts with the main vortex. Existence of lambda shocks confirms that the flow behind the diffracting shock at low Mach numbers is partly transonic.

At low Mach number the SST k - ω turbulence model shows a distinct main vortex with a secondary vortex that is formed due to viscous effects under the shear layer. The experimental pictures show a strong turbulent flow that starts from a point upstream of the separation point, and engulfs the complex flow region. The inability to capture the secondary vortex under the shear layer could be attributed to the turbulent flow that dominates the region. The turbulent flow around the shear layer is not well predicted in the SST k-ω and k-ε turbulence models. This implies that both numerical models could not predict this flow feature accurately due to too much dissipation in free stream flow field.

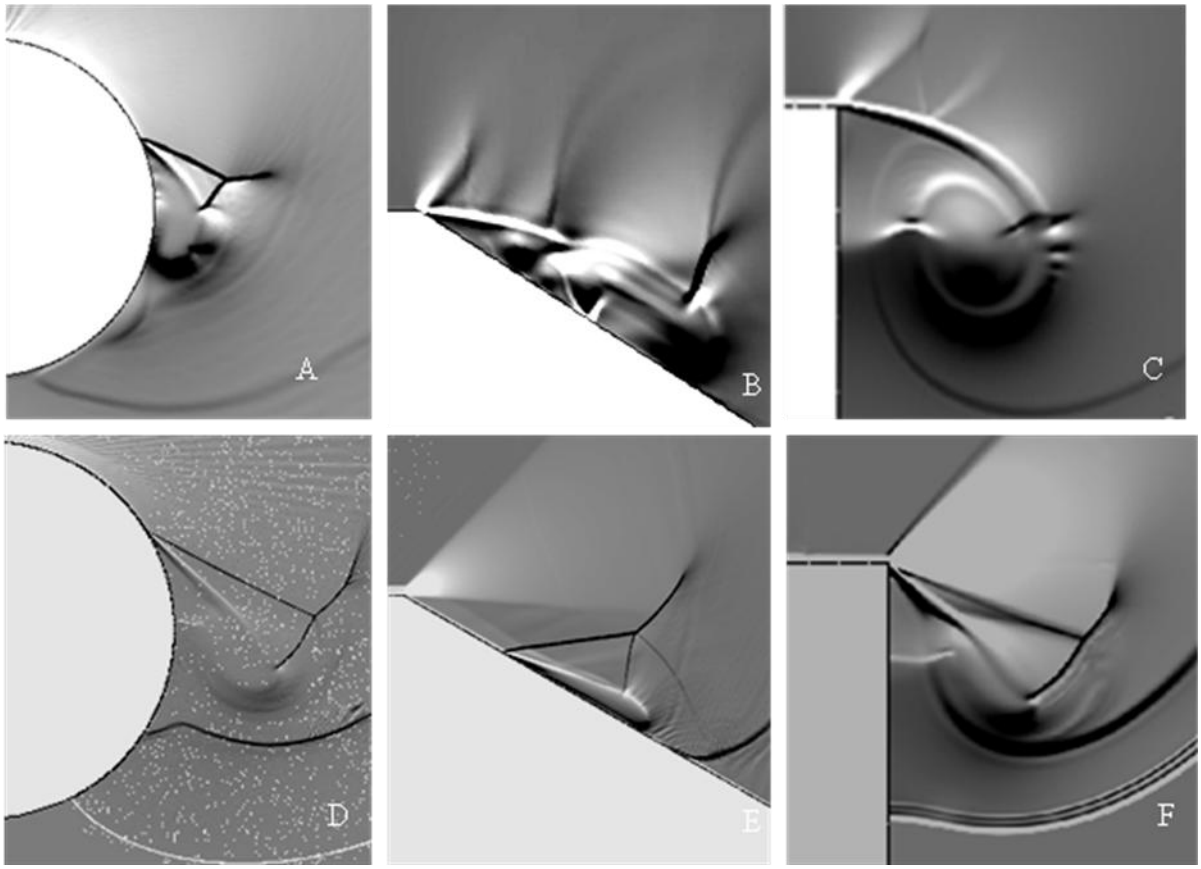

Figure 6.2: Comparison of the flow features behind the low and high incident shock Mach numbers on different walls

(A) M_s 1.6 on 200mm diameter wall (B) M_s 1.6 on 30° corner wall (C) M_s 1.6 on 90° wall (D) M_s 3.0 on 200mm diameter wall (E) M_s 3.0 on 30° wall (F) M_s 3.0 on 90° wall

The numerical (SST k-ω turbulence model) results shows the three - shock configuration and this can be more than one on a curved wall depending on the incident shock Mach number. These multiple shock configurations are due to the formation of different flow regions within the perturbed region behind the diffracting shock wave. The flow regions have different flow conditions enhanced by non-uniform compression of the gas behind the diffracting shock. However, at high incident shock Mach number the complex flow region moved away faster from the near wall effect which enhances the fading away of the upper triple point with time.

6.2 The Global Flow Behaviour behind the Diffracting Shock Wave

The flow domain engendered by the diffraction of the planar shock wave over a 90° convex corner is dependent only on the incident shock Mach number for a gas with a constant specific heat ratio (γ =constant) as observed by Skews [58 - 60] and Kleine [26]. Three flow regimes have been identified behind the diffracting shock on a 90° convex wall (subsonic: $1 < M < 1.35$, Transition: $1.35 < M < 2.07$, and Supersonic: $M > 2.07$ Klein [27]). The flow features in the perturbed region behind the diffracting shock is different for each flow regime. For subsonic flow, three important flow features observed are: a shear layer that evolves from the corner, the expansion wave bounded upstream by a sound wave and downstream by a terminator as well as the diffracted and undiffracted portion of the incident shock.

6.2.1 Low Mach number incident shocks

The diffraction of incident shock Mach numbers between 1.4 and 1.6 on plane and curved walls induces flow that is partly transonic and partly supersonic. The shear layer evolves from the corner/bend immediately after the start of diffraction with lambda shocks forming along the shear layer. This observation confirms the earlier work by Kleine [27] that the flow around the corner is transonic. For a 30° corner wall, a series of lambda shocks are formed above the shear layer due to the closeness of the shear layer to the wall surface. However, the lambda shocks that form on the 90° corner wall are limited to the region close to the corner as shown in Figure 6.3B. This shows that the flow retains its transonic nature over a wider region on the 30° wall than on the 90° corner.

For curved walls the lambda shocks are formed at a region along the curvature where the flow is locally transonic as shown in Figure 6.3C. The expansion waves along the curved wall are not centered hence the flow velocity varies with further diffraction of the shock downstream. The lambda shock impinges on the boundary layer and the thickness of the boundary layer increases prior to separation of the flow from the wall.

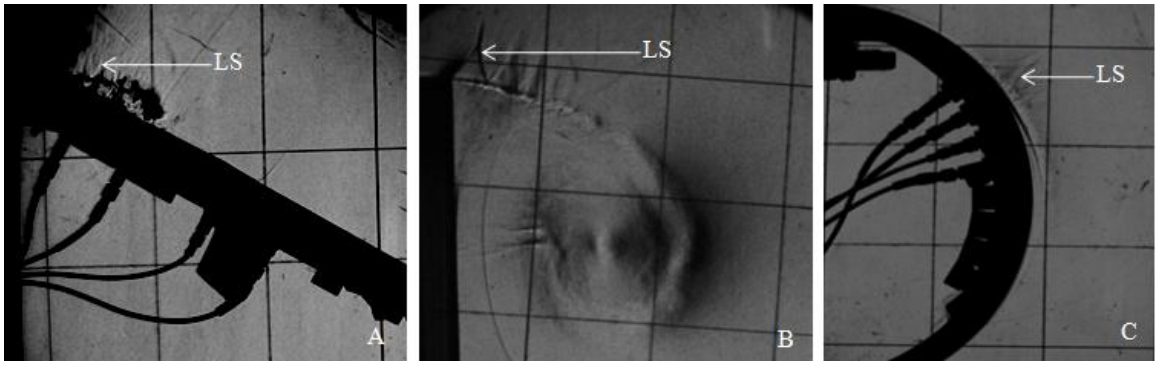

Figure 6.3: Lambda shock propagation at incident shock Mach number 1.5 on 30^0, 90^0 and 200mm diameter walls

The geometrical change of a curved wall is gradual and this promotes gradual development of the adverse pressure gradient especially at low incident shock Mach numbers. The flow upstream is at higher momentum due to expansion but the gas downstream is compressed by the diffracting shock wave. Shocklets are propagated as earlier explained and later coalesce into a weak shock that separates the expanded and compressed gas. The weak shock becomes strong and is perturbed by the adverse pressure gradient at the wall. This process of perturbation makes the flow to become stagnated and separates from the wall surface as shown in Figure 6.4.

The perturbed shock transforms to an oblique shock and extends downstream. The flow domain is partitioned by the evolving oblique shock into a subsonic flow near the wall and expanding flow upstream. There is a sharp velocity gradient between the two flows hence a shear layer emanates from the wall at the separation point. The oblique shock brings the flow upstream parallel to the flow along the shear layer before the flow is finally matched with the subsonic flow at the wall. The region across the shear layer has a finite velocity discontinuity without any significant pressure gradient as shown in Figure 6.4b&d.

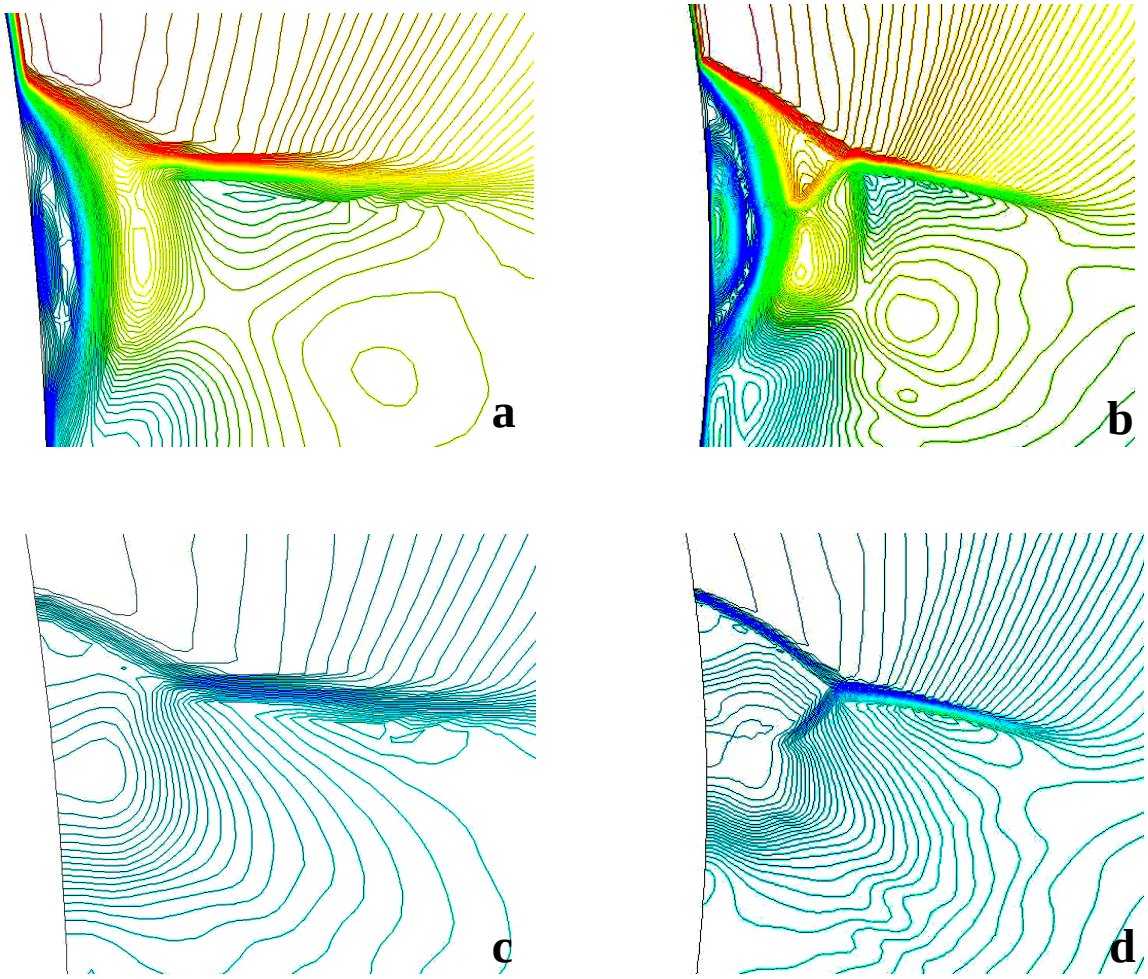

Figure 6.4: The velocity (a & b) and Pressure (c & d) contour of a separating flow at Ms 1.5 on 200mm diameter wall

Separation is evident on 30° plane walls even at a very low incident shock Mach numbers like 1.34. However, separation is not evident on the 200mm diameter wall for incident shock Mach number 1.5 at the instant of the shock engaging the curved wall. The early separation of flow on plane walls is due to a sudden change in boundary condition which enhances sudden development of adverse pressure gradients that triggered the separation of the flow.

The long time scale diffraction of the incident shock over a 90° corner wall enhances extension and break-up of the shear layer into vortices. The earlier works on shock wave diffraction could not capture this stage of the flow development because of the scale at

which the experiments were conducted. The present analysis is conducted in a large scale experimental shock tube that is about ten times larger than the conventional shock tubes.

Three stages of flow development are identified on plane walls: evolution of its shear layer which is smooth initially as it evolves from the corner, turbulent break-up of shear layer on 30^0 wall, and development of homogenous turbulent flow. The turbulent flow that is observed on 30° corner wall shows the significant effects of the Reynolds number on the flow. The experimental images for the diffraction of incident shock $M_s = 1.6$ over a curved wall also show strong turbulent flow which engulfs the complex flow region as shown in Figure 4.15a. However, the two-dimensional numerical analysis does not reveal this observation. It is proposed that this new observation may result from a boundary layer effect which is three-dimensional.

The development of a three – shock configuration within the perturbed region behind the diffracted shock wave for low incident shock indicates that there are three distinct flow regimes. These flow regimes are the free - stream flow which is not affected by the near wall effects, the expanding gas upstream and the compressed gas that is close to the diffracting shock wave. The flow conditions in these regions are matched by the three shocks that formed the so-called three-shock configuration.

6.2.2 High Mach numbers incident shocks

At high incident shock Mach numbers the flow behind the diffracting shock is supersonic with the compressibility effect not strongly felt by the flow upstream due to the speed at which the diffracting shock moves downstream. The complex flow region moves from the wall into the free stream flow and the expanded flow that is exiting the oblique shock (A-B in Figure 6.5) remains locally supersonic and is made parallel to the shear layer (SL). There is a significant portion of the expanded flow above the complex flow region that does not cross the oblique shock as shown in Figure 6.5. This flow region shown as A-D in the figure attains the same flow conditions with the downstream compressed flow

through a second shock (SS). The flow above the shear layer which is supersonic becomes matched with the compressed flow behind the contact surface through another second shock. The present requirement for two second shocks enhances the distortion of the original second shock at a point where it forms a three-shock configuration (TSC) with the oblique shock wave as illustrated in Figure 6.5. The profile of the second shock depends on the incident shock Mach number. The higher the Mach number the farther away the complex flow region is from the wall, the less the curvature of the second shock because the property gradients across this shock reduces.

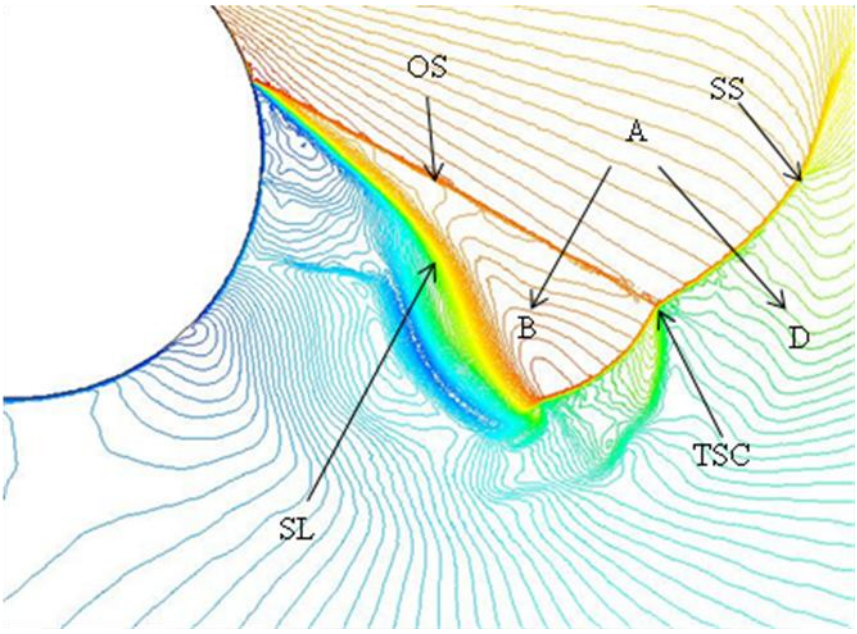

Figure 6.5: The velocity contour plot of the complex flow region for incident shock Ms 3.0 on 200mm diameter wall

At some incident shock Mach numbers (Ms < 3.0), two three shock configurations are formed as earlier explained in section 4.2.2. The upper triple point fades away when the complex flow region is far enough from the wall. A secondary shear layer may emerge from this triple point especially if the incident shock Mach number is moderate and this will pull around the original shear layer that forms the main vortex as shown in Figure 6.6. The flow exiting the lower portion of the second shock is at higher velocity (HSF) compared to the subsonic flow under the shear layer (LSF) as shown in Figure 6.6. A

secondary shock is embedded in the main vortex to match this flow with the subsonic flow close to the wall surface. Under the shear layer two flow regimes are formed as shown in Figure 6.6. There is a subsonic flow (LSF) around the separation point and the high speed flow (HS) around the main vortex; these two flows are matched by the recompression shock. This shock is evident in both low and high incident shock Mach numbers. It fades away with time at high incident shock Mach numbers, because the complex flow region is far enough from the wall surface.

The contact surface in front of the complex flow region creates two regions of different densities, low density flow at the vicinity of the main vortex and compressed flow close to the diffracting shock wave. The contact surface with its upper part originated from the point of contact between the diffracted and the undiffracted incident shock. It extends towards the wall and develops a kink as it approaches the wall surface as shown in Figure 6.7.

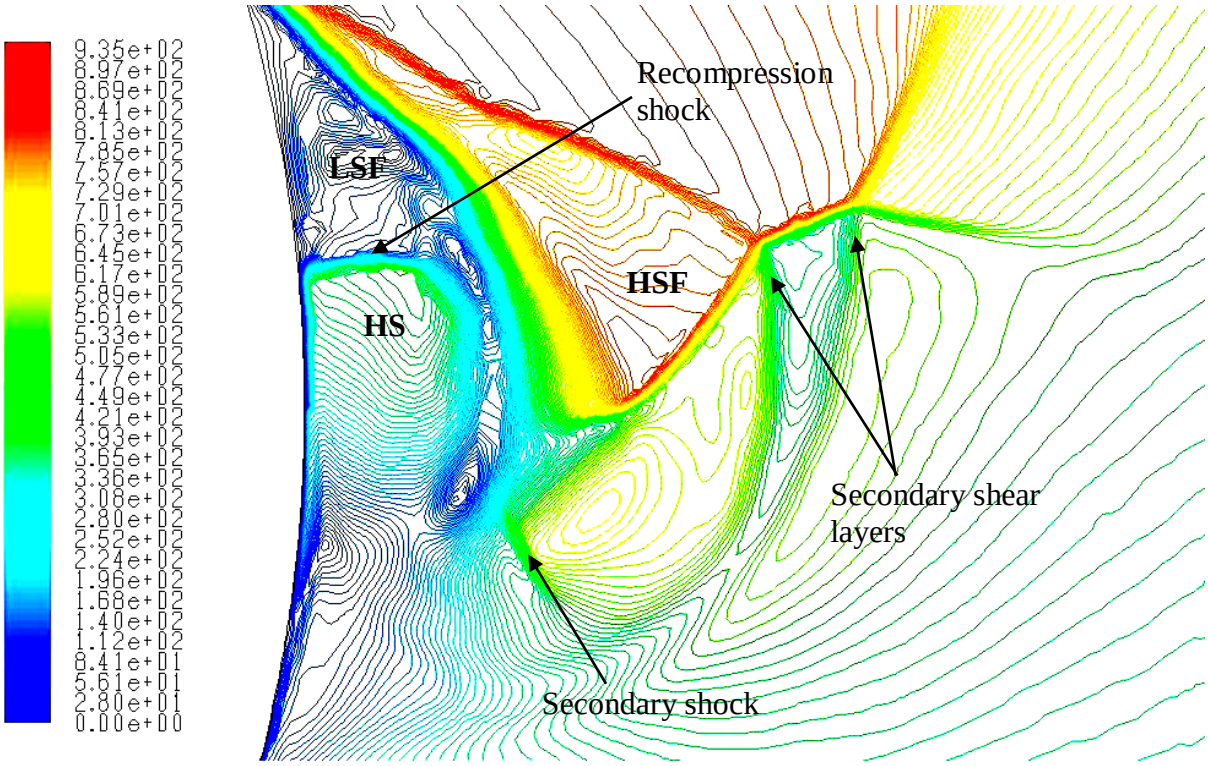

Figure 6.6: A secondary shear layer from three-shock configuration (Velocity contour plot)

The contact surface shows a more pronounced kink at higher incident shock Mach numbers; this can be attributed to sudden change in radial velocity as the flow passes the complex flow domain. The fluid particles gain some tangential momentum as it approaches the wall surface as described by equation (39). The second term of the equation tends to zero at the wall and the tangential momentum represented by the third term increases as the radius decreases. The fluid particles at the lower portion of the contact surface will gain more momentum thereby distorting the contact surface as shown in Figure 6.7.

$$\frac{\partial \rho V_r}{\partial t} + (\rho V.\nabla)V_r - \rho\frac{1}{r}V_\theta^{\,2} = -\frac{1}{\rho}\frac{\partial P}{\partial r} + g_r + F_{viscous} \qquad (39)$$

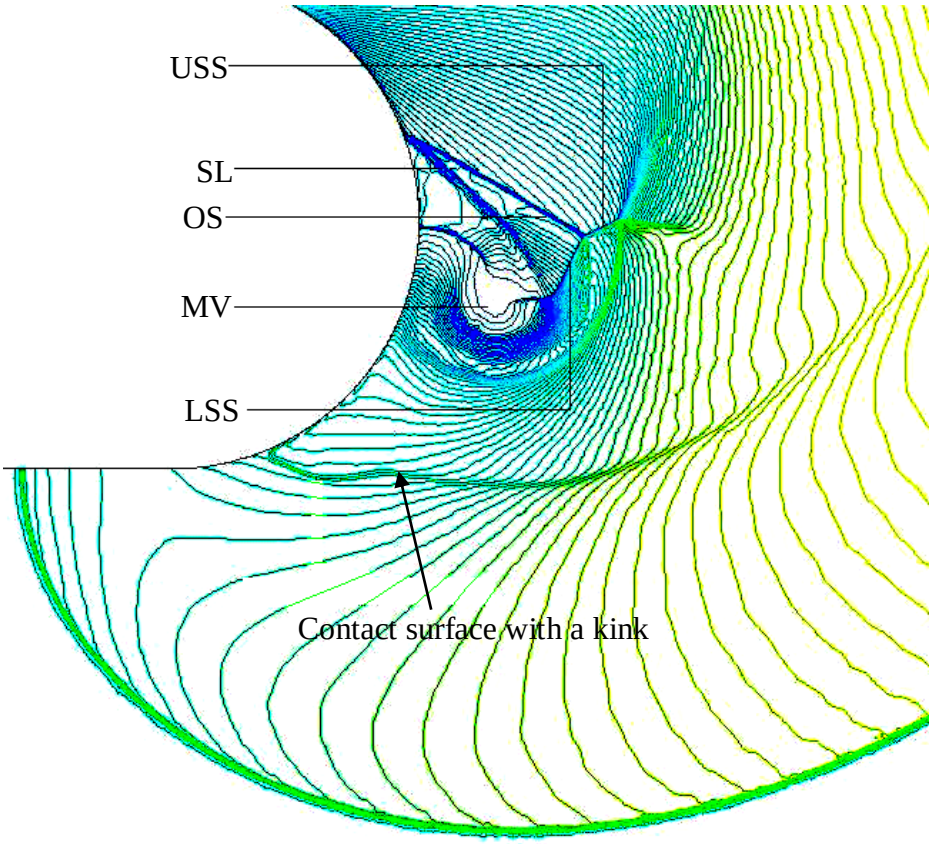

Figure 6.7: Density contour plot showing a kink at the lower portion of the contact surface

7.0 CONCLUSION AND RECOMMENDATION

7.1 Introduction

The unsteady separation behind a diffracted shock wave over convex walls has been investigated with a view to give the detailed analysis of the global flow behaviour behind the diffracted shock wave. Large scale experiments were carried out in a purpose built shock tube that allows for the diffraction of a shock over a maximum period of about 1500μs. Images of the interaction behind the diffracting shock were captured by a schlieren optical system. Three cases were considered for 30° corner wall (M_s = 1.34, 1.4 and 1.5) while two cases were considered for 90°corner wall (M_s = 1.4 and 1.5). For the curved wall incident shock Mach numbers of 1.5 and 1.6 were considered.

The pressure histories at different locations along the curved wall were recorded for incident shock M_s = 1.5, 1.56 and 1.57. A particular case of M_s = 1.56 was used for comparison with pressure history recorded from numerical simulation. Important information obtained from the pressure histories are time and location of separation point, and location of flow instability under the shear layer.

Numerical simulations were carried out using incident shock Mach numbers ranging between 1.34 to 3.0 over 200, 400, 600, 800 and 1000mm diameter walls, and 30° and 90° corner walls. The images of interaction behind the diffracting shock were obtained using numerical schlieren, density and pressure contour/flood plot. Numerical data were obtained for the angle of separation and shear angle for various flow conditions over different walls. These data were plotted to examine the effect of wall geometry and influence of incident shock Mach numbers on the flow behaviour behind the diffracting shock wave. Direct comparison of the experimental pictures of the flow interaction with numerical images was used to validate the results. This validation is used to justify further analysis using numerical computation for high incident shock Mach numbers.

7.2 Conclusion

The comprehensive explanation of the global flow behaviour behind the diffracted shock wave was given based on the results of the tests of the low incident shocks complemented with numerical computation for high incident shocks. The following conclusions were deduced from the analysis:

- There is a significant difference between the large and small scale experiments; hence, the scale of experiment (both temporal and spatial) plays a very important role in the analysis of shock wave diffraction on convex walls.
- The instability along the shear layer and the breaking up of shear layer into vortices are evident in both experimental and numerical results.
- The movement of separation point behind a diffracting shock wave is dependent on the strength of the incident shock and radius of curvature for low Mach number incident shocks. At high Mach number the behaviour of separation point is independent of the radius of curvature.
- The number of three - shock configuration that forms on curved wall is dependent on the incident shock Mach number. However, the upper triple point disappears as the complex flow region moves far away from the wall surface.
- The flow features within the complex flow region consists of many weak shocks such as: second shock, secondary shock, recompression shock and an oblique shock. However, the formation of both the secondary and recompression shock depends on the incident shock Mach number and is time dependent.
- The sudden change in radial velocity of the flow passing the surface of the main vortex is proposed to be the main cause of the kink on the lower part of the contact surface.
- The numerical dissipation in the SST k-ω turbulence model used in this study is too high in the free stream flow field.

7.3 Recommendations

- The present study has been able to test maximum incident shock Mach number of 1.62 due to equipment constraints. Further work should be conducted to ascertain the flow behaviour at higher Mach numbers at the same scale of experiments.
- The ability to capture the development of various flow features at smaller time increments would have enhanced a better understanding of the transient evolution of the separation phenomenon. Large scale experimentation using high speed flow visualization system should be conducted to capture the instantaneous behaviour and evolution of the flow.
- Further work should be carried out on planar walls of different angles and curved walls like spheres with different radii.
- The present investigation calls for further development of the existing turbulence models in the code used to capture the vortices that are formed from the breaking up of the shear layer, and to predict the upstream turbulent flow on curved walls.
- Further work should be carried out on the threshold incident shock Mach number at which the movement of separation point is constant with time.
- Further investigation should be conducted on the influence of Reynolds number on the flow features behind the diffracting shock on both planar and curved walls.
- Three dimensional investigation of the diffraction of shock on curved wall should be conducted to ascertain the behaviour of the upstream turbulent patches.

REFERENCES

1. A. Al – Falahi, M.Z. Yusoff, N.H. Shuaib and T. Yusaf, *Flow instability in shock tube due to shock wave-boundary layer-contact surface Interactions, a numerical study.* European Journal of Scientific Research, 2009. 30(1): pg. 164-176.
2. M.T. Allen, S. Richard, and L.K. Barbara, *The triple point paradox for the nonlinear wave system.* SIAM Journal of Applied Mathematics, 2006. 67(2): pg. 321-336.
3. J. D. Anderson, ed. *Modern compressible flow with historical perspective* Third edition ed. McGrawHill series in aeronautical and aerospace engineering, ed. J.D. Anderson. 2003, McGrawHill New York. 760.
4. J.D. Anderson, ed. *Computational fluid dynamics, the basics with applications*. International edition ed. Mechanical Engineering series. 1995, McGRAW-HILL New York.
5. R.A. Anthony, W.C. Mark, and L.P. Eric, *Test-time extension behind reflected shock waves using CO2–He and C3H8–He driver mixtures* Shock Waves, 2006. 16(2): pg. 157 – 165.
6. F.J. Barbosa, *shock wave interaction with a spiral vortex.* Physics of fluids, 2001. 13(10): pg. 3049-3060.
7. F.J. Barbosa, *Shock wave and shock wave-vortex interactions in a bifurcated shock tube*. PhD Thesis, 2000, Faculty of Engineering and Built Environment, University of the Witwatersrand, South Africa.
8. F.J. Barbosa, and B.W. Skews, *Experimental confirmation of the von Neumann theory of shock wave reflection transition* Journal of Fluid Mechanics, 2002. 472: pg. 263-282.
9. G. Ben-Dor, O. Igra and T. Elperin, eds. *Handbook of shock waves*. Vol. 1. 2001, Academic Press: San Diego. 2,102.
10. G. Ben-Dor, M. Ivanov, E. I. Vasilev and T. Elperin, *Hysteresis processes in the regular reflection↔Mach reflection transition in steady flows.* Progress in Aerospace Sciences, 2002, 38(4-5): pg 347-387

11. G. Ben-Dor, I.M. Dewey, and K. Takayama, *The Reflcctlon of a Plane Shock Wave over a Double Wedge.* Journal of Fluid Mechanics 1987. 176: pg. 483 – 510.
12. M.K. Berezkina, I.V. Krasovskaya, and D.K. Ofegeim, *Shock wave reflection and diffraction on a convex double wedge.* Technical physics letters, 2004. 30(12): pg. 1017- 1019.
13. M.K. Berezkina, I.V. Krasovskaya, and D.K. Ofegeim, *Diffraction of a two-shock configuration by a convex cylindrical surface,*. Technical Physics, 2006. 51(7): pg. 827-833.
14. R.S. Craig, P.S. Steven and P.B. Mathew, *Disturbances from shock/boundary layer interactions affecting upstream hypersonic flow.* 35th AIAA Fluid Dynamics Conference and Exhibit, 6-9 June 2005, Toronto, Ontario Canada.
15. R.S. Craig, *Disturbances from Shock/Boundary-Layer Interactions Affecting Upstream Hypersonic Flow,* Dec 2005, PhD Thesis Purdue University.
16. J.M. Delery, *Shock wave/Turbulent boundary layer interaction and its control* Prog. Aerospace Science 1985. 22: pg. 209-280.
17. R.A. Evans, and M.I.G. Bloor. *The starting mechanism of wave induced flow through a sharp edge*. in *Proc. 7th Int. shock tube symposium* 1977.
18. F.G. Friedlander. The diffraction of sound pulses: I, Diffraction by a semi-infinite plane, Proceedings of the Royal Society of London, Vol. 186, pg. 322-344, 1946
19. A. Haselbacher, S. Balachandar, and S.W. Kieffer, *Open-Ended Shock Tube Flows: Influence of Pressure Ratio and Diaphragm Position* AIAA Journal 2007. 45(8): pg. 1917.
20. L.F. Henderson, *On the Whitham theory of shock-wave diffraction at concave corners.* Journal of Fluid Mechanics, 1980. 99 (4): pg. 801-811.
21. R. Hillier, ed. *Numerical modeling of shock wave diffraction* Shock Waves Pg.17., ed. B. Marsielle IV, R. and Dumitrescu,L. 1995, Springer: Berlin
22. J.O. Hinze. *Turbulence*, 1975, McGraw – Hill Publishing Company, New York.
23. L.N. Howard, and J. Matthews, *On the vortices produced in shock diffraction.* Journal of Applied Physics, 1956. 27: pg. 223-231.

24. M. Ivanov, Y. Bondar, D. Khotyanovsky, A. Kudryavtsev, G. Shoev, *Effects of viscosity on steady reflection of weak shock waves* in *40th Thermophysics conference*. 2008, American Institute of Aeronautics and Astronautics Inc: Seattle, Washington.
25. W. John, *An interferometric investigation of the regular to Mach reflection transition boundary in pseudostationary flow in air*, in *UTIAS Technical note*. 1985, UTIAS.
26. H. Kleine, E. Ritzerfeld, and H. Grönig, *Shock waves diffraction - new aspects of an old problem*. in *19th ISSW*. 1995. Marseille: Springer.
27. H. Kleine, E. Ritzerfeld, and H. Gronig, *Shock wave diffraction at a ninety degree corner.* Computational Fluid Dynamics, 2003. 12(2): pg. 142-158.
28. D.D. Knight, *Numerical simulation of compressible turbulent flows using Reynolds-Average Navier-Stokes equations*, AGARD Report R-819.
29. S. Kobayashi, T. Adachi, and T. Suzuki, *Examination of the von Neumann paradox for a weak shock wave.* Fluid Dynamics Research, 1995. 17: pg. 13-25.
30. B.E Launder and D.B. Spalding, *The numerical computation of turbulent flows.* Comput. Methods Appl. Mech. Eng. 1974. Vol. 3: pg 269-289.
31. L.D. Landau, and E.M. Lifshitz, eds. *Fluid Mechanics* 2nd ed ed. 1987, Pergamon.: Oxford.
32. C. Law, B.W. Skews, and N. Menon, *Near-wall features in transient compressible flow on convex walls* in *25th International Symposium on Shock Waves* E.A. G Jagadeesh, KPJ Reddy (Eds.) Editor. 2005, Society for Shock Wave Research, IIS.: Bangalore, India. pg. 77-82.
33. C. Law, B.W. Skews, and K.H. Ching, *Shock wave diffraction over complex convex walls* in *26th International Symposium on Shock Waves, (ISSW26)* 2007: Göttingen
34. C. Law, Q. Abbas, J. Nordström, B. Skews, *The effect of Reynolds number in high order accurate calculations with shock diffraction* in Proceeding of Sevevnth South African Conference on Computational and Applied Mechanics SACCAM 2010, Pretoria.

35. G. Lebo, and V.D. Zvorykin, *The study of turbulent mixing zone development in laser shock tube experiments* Phys. Scr. T132 (2008) 2008(014018): pg. 4.
36. H. Li, G. Ben-Dor, and Z.Y. Han, *Analytical prediction of the reflected- diffracted shock wave shape in the interaction of a regular reflection with an expansive corner* Fluid Dynamics Research 1994. 14**:** pg. 229 -239.
37. Q. Li, *A shock tube – based facility for impact testing.* Experimental Techniques, 2007. 31 (4): pg. 25 -28.
38. M.J. Lighthill, *The Diffraction of Blast II.* Proc. Royal Society of London, 1950 200: pg. 554 - 565.
39. W.W. Liou and P.G. Huang, *Calculations of oblique shock wave/turbulent boundary-layer interactions with new two-equation turbulence models,* NASA CR-198445.
40. W. Merzkirch. *Flow visualization. 1987, Academic Press, Inc.Orlando Florida.*
41. F.R. Menter, *Zonal two equation k-w Turbulence models for aerodynamic flows.* AIAA 1993(93-2906).
42. O.O. Mojola, *Steady flow separation along a straight streamwise corner.* Applied Scientific Research, 1976. 31(6): pg. 431-436.
43. A.O. Muritala, C. Law and B.W. Skews, *Near wall effects on the global flow behaviour behind a diffracted shock wave* in Proceeding of Seventh South African Conference on Computational and Applied Mechanics. 2010: Pretoria, South Africa.
44. M. Nobuya, S. Nagata, K. Ikuya, S. Kasuya, T. Shu and M. Yoichiro, *Development of Ultra Small Shock Tube for High Energy Molecular Beam Source* in *Proceedings of the 26th International Symposium on Rarefied Gas Dynamics* 2008
45. H. Onodera, *Shape of a shock wave front diffracting on a perforated wall.* Experiments in Fluids, 1998. 24: pg. 238-245.
46. E.K. Park, *Supersonic flow in a shock tube of divergent cross section* UTIA, Editor. 1952, University of Toronto Ins. for Aerophysics.
47. V.C. Patel**,** W**.** Rodi and G**.** Scheuerer, *Turbulence models for near-wall and low-Reynolds-number* ***flows***: A review, AIAA J, 1984. Vol.23, No.9, pg.1308.

48 . T. Peacock, R. Coral, and G. Haller, *Experimental investigations of a new approach to unsteady separation* AIAA Paper, 2005(4903).

49. L. Prandtl, in Verhandlungen des dritten Internationalen Mathematiker – Kongresses in Heidelberg 1904, A. Krazer, ed. Teubner Leipzig, Germany (1905), pg 484. English translation in Early Development of Modern Aerodynamics, J. A. Ackroyd, B.P. Axcell, A. I Ruban, eds, Butterworth – Heinemann Oxford, UK (2001), pg. 77.

50. I.S. Rego, K.N. Sato and S. Kugimiya, *Development of a Large Diameter Diaphragmless Shock Tube for Gas-Dynamic Laser Studies.* Materials Science Forum 2008. 566 pg. 9-14.

51. S. Richard, and M.T. Allen, *The von Neuman Paradox*. Computational Method in Applied Sciences. Vol. 16. 2008, Netherlands: Springer.

52. N. Rott, *Diffraction of a weak shock with vortex generation.* Journal of Fluid Mechanics 1956. 1: pg. 111-128.

53. A.I. Ruba, X. WU, and R.M.S. Pereira, *Viscous – inviscid interaction in transonic Prandtl – Meyer flow.* Journal of Fluid Mechanics, 2006. 568: pg 387 – 424.

54. A. Sasoh, K. Takayama, and T. Saito, *A weak shock reflection over wedges.* Shock Waves, 1992. 2(4): pg. 277-281.

55. H. Schlichting, eds. *Boundary layer theory* 8th revised and enlarged edition ed. 2000 Springer-Verlag 20-30.

56. W.R. Sears, and D.P. Tellionis, *Boundary layer separation in unsteady flow* SIAM Journal of Applied Mathematics, 1975. 28(1): pg. 215-235.

57. W.C.F. Shepherd, *Spontaneous Ignition of an Inflammable Gaseous Mixture on Release from Compression.* Nature 1954. 174: pg. 658 - 659.

58. B.W. Skews, *The pertubed region behind a diffracting shock wave.* Journal of Fluid Mechanics, 1967b. 29: pg. 705-719.

59. B.W. Skews, *Shock wave diffraction on multi-faceted and curved walls* Shock Waves, 2005. 14(3): pg. 137-146.

60. B.W. Skews, *The shape of diffracting shock wave.* Journal of Fluid Mechanics, 1967a. 29: pg. 297-304.

61. M. Sun, and K. Takayama, *The formation of a secondary shock wave behind a shock wave diffraction at a convex corner* Shock Waves 1997. **7**: pg. 287-295.
62. M. Sun, and K. Takayama, *A note on numerical simulation of vortical structures in shock diffraction.* Shock waves, 2003. 13: pg. 25-32.
63. K. Takayama, and O. Inoue, *Shock wave diffraction over a 90 degree sharp corner.* Posters Presented at 18th International Symposium on Shock Waves ISSW 1991. 1(4): pg. 301-312.
64. C. Tropea, A.L. Yarin and J.F. Foss, Springer handbook of experimental fluid mechanics, Springer-Verlag Berlin Heidlberg, 2007.
65. J.R. Viegas, M.W. Rubesin, C.C. Horstman, *On the use of wall functions as boundary conditions for two-dimensional separated compressible flows*, AIAA Ppaper 85-180, Reno, NV.
66. H.K. Versteeg and W. Malalasekera. *An introduction to computational fluid dynamics: the finite volume method, 1995*, Addison Wesley Longman Limited, England.
67. F.M. White, ed. *Viscous fluid flow*. ed. M. Inc. 1974: New York.
68. D.C. Wilcox. *Turbulence modeling for CFD*. 1998, DCW Industries, Inc,. La Canada, California.
69. D. C. Wilcox, *Wall matching, a rational alternative to wall functions*, 1989, AIAA Paper 89-611, Reno, NV.
70. D.C. Wilcox, *Reassessment of the scale determining equation for advanced turbulence models*, 1988a, AIAA Journal, Vol.26, No.11, pg 1299-1310.
71. A.R. Zakharian, M. Brio, J.K. Hunter, G.M. Webb, *The von Neumann paradox in weak shock reflection.* Fluid of Fluid Mechanics, 2000. 422: pg. 193-205.
72. H. Zekai, F.D. David, and K.H. Ronald, *Contact surface tailoring condition for shock tubes with different driver and driven section diameters* Shock Waves 2009. 19: pg. 331–336.

APPENDICES

APPENDIX A: Detailed drawing of the models

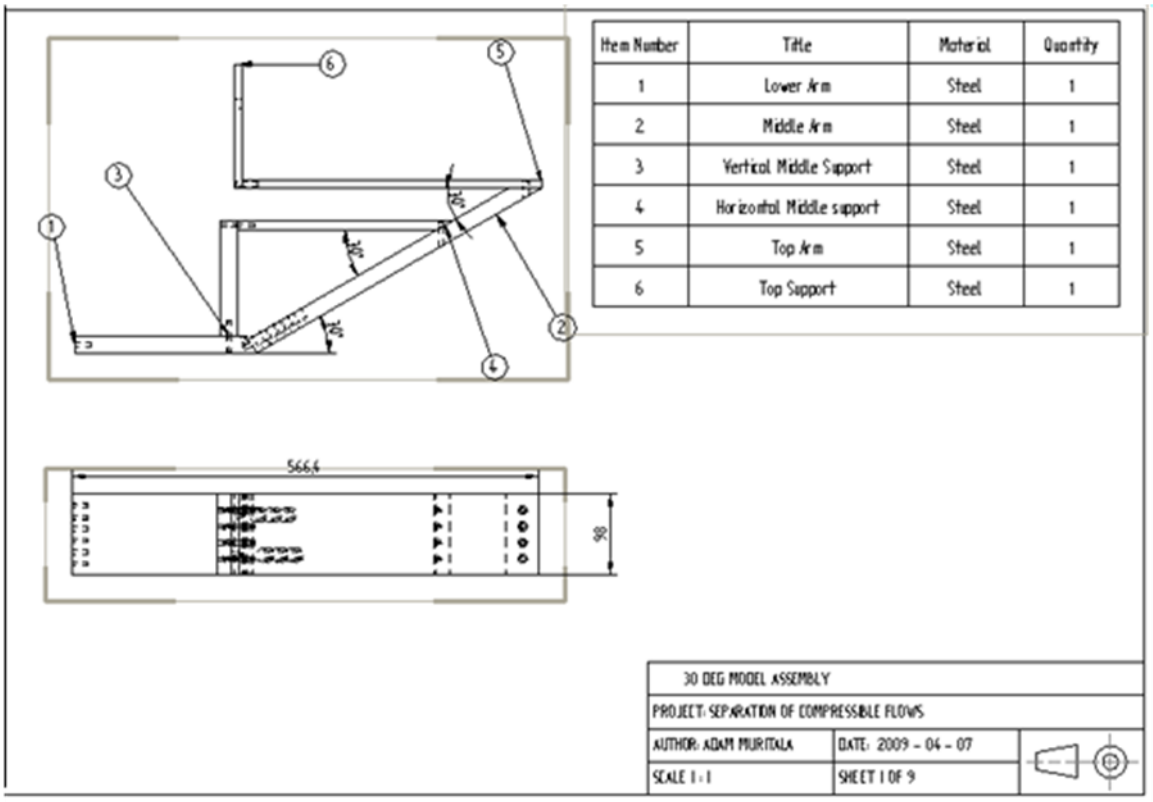

PLATE A1: The assembly of 30^0 wall

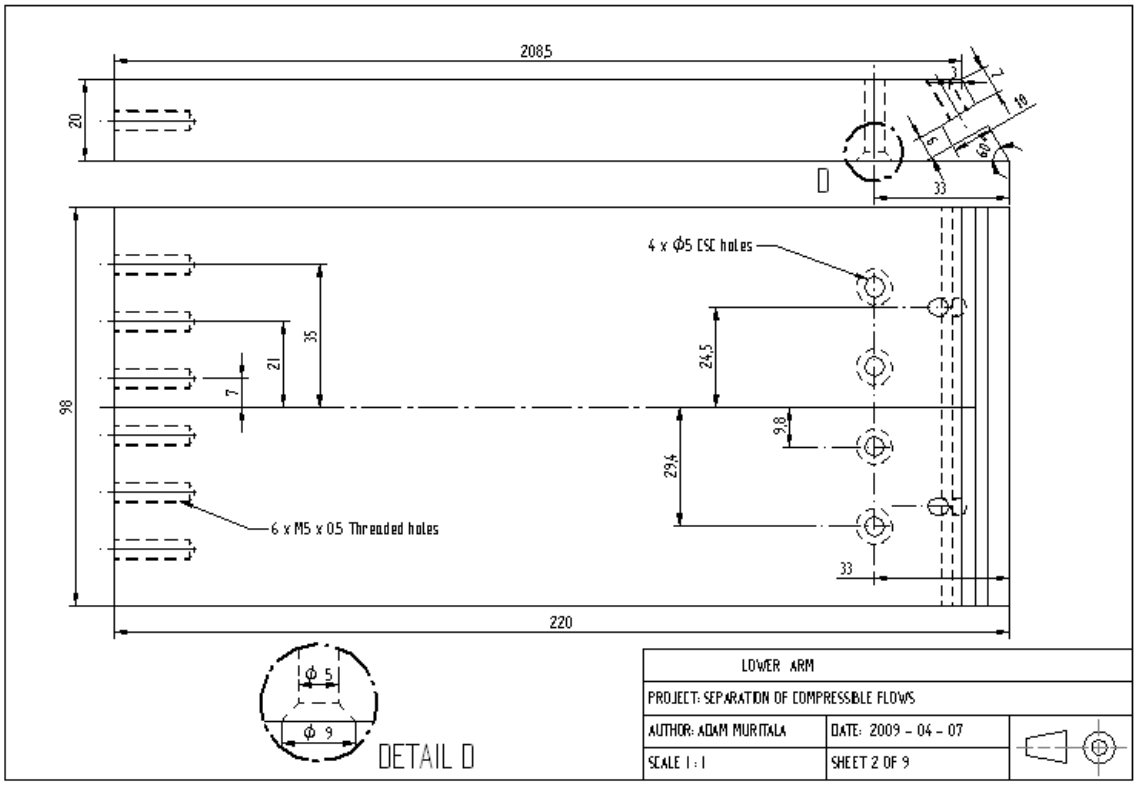

PLATE A2: The lower plate of 30^0 wall

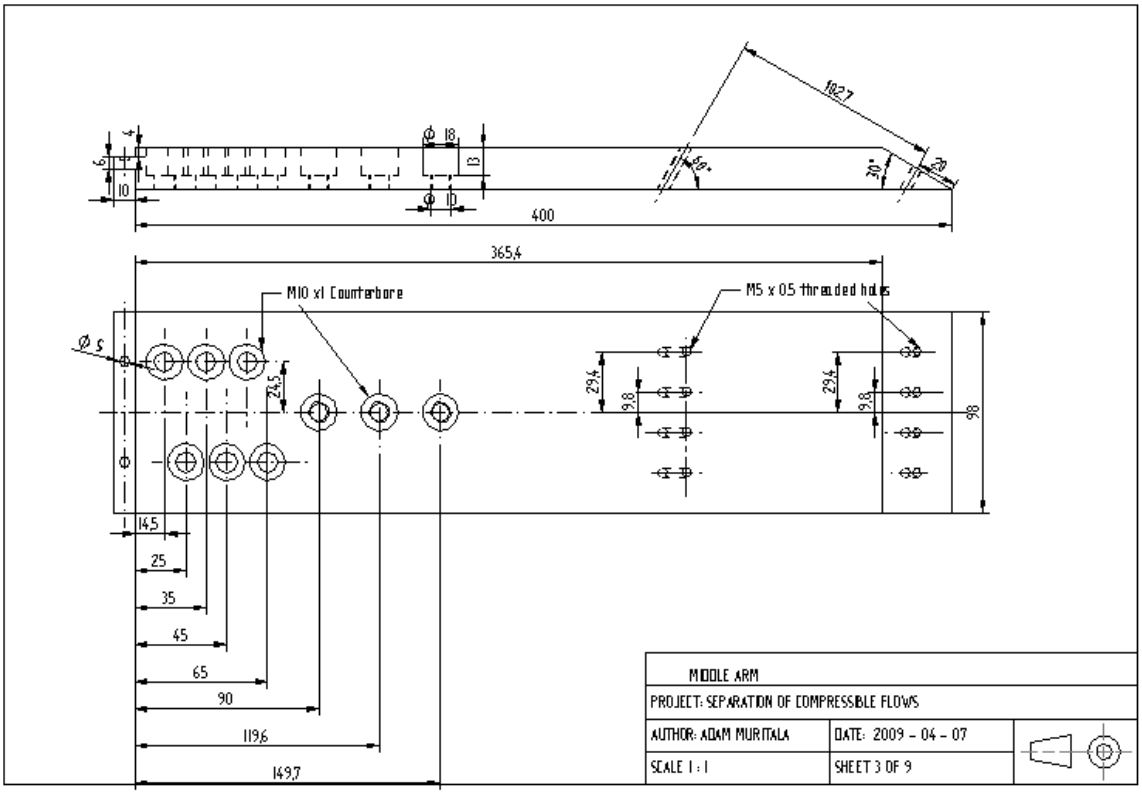

PLATE A3: The middle plate of 30^0 wall

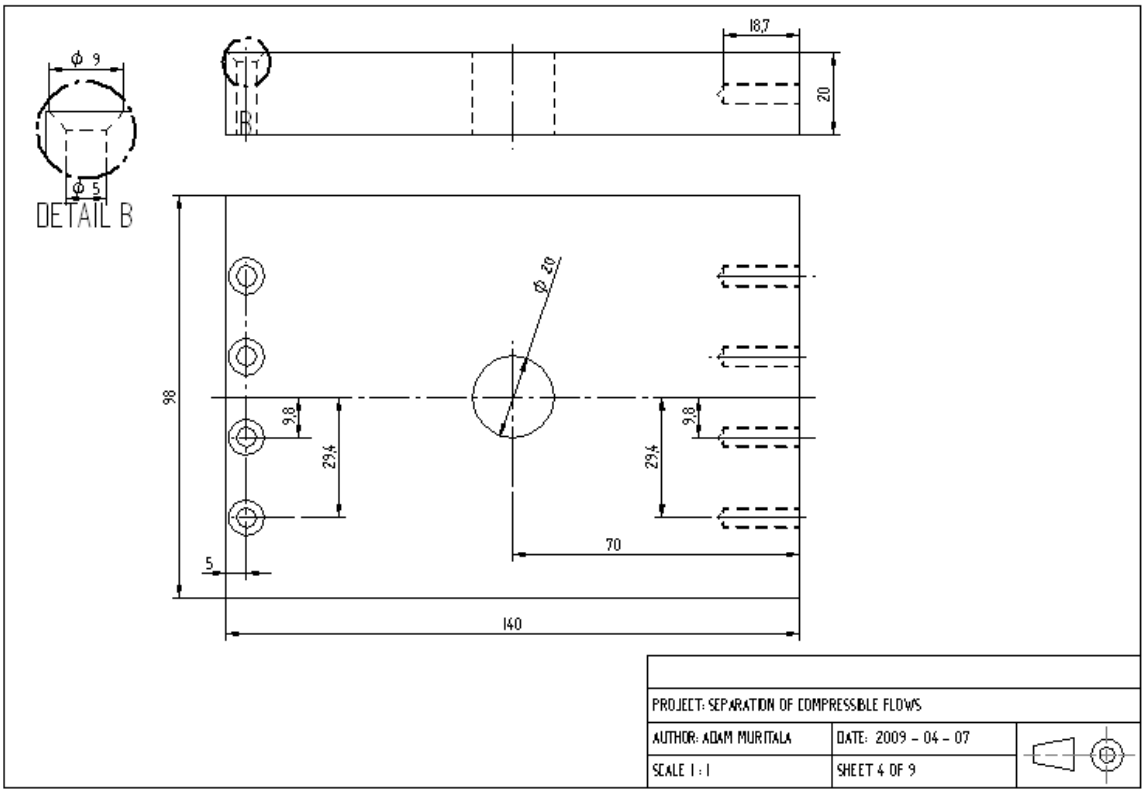

PLATE A4: The vertical middle plate of 30^0 wall

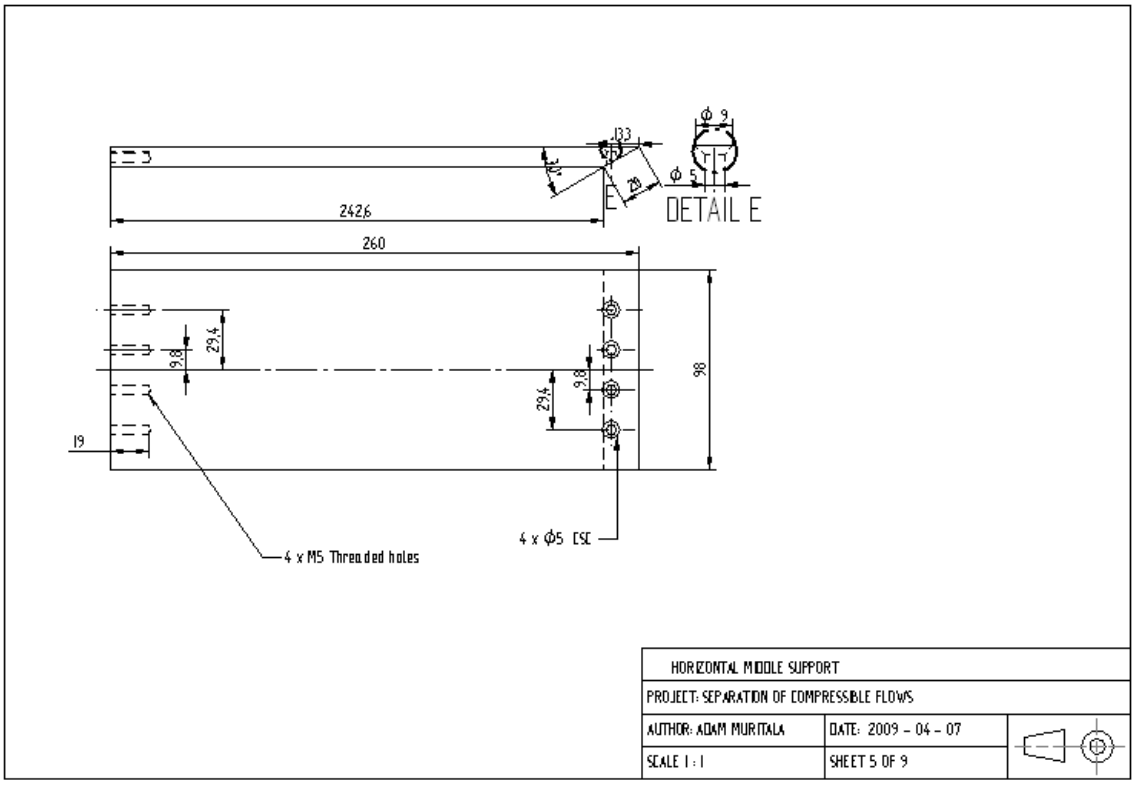

PLATE A5: The horizontal middle support plate of 30^0 wall

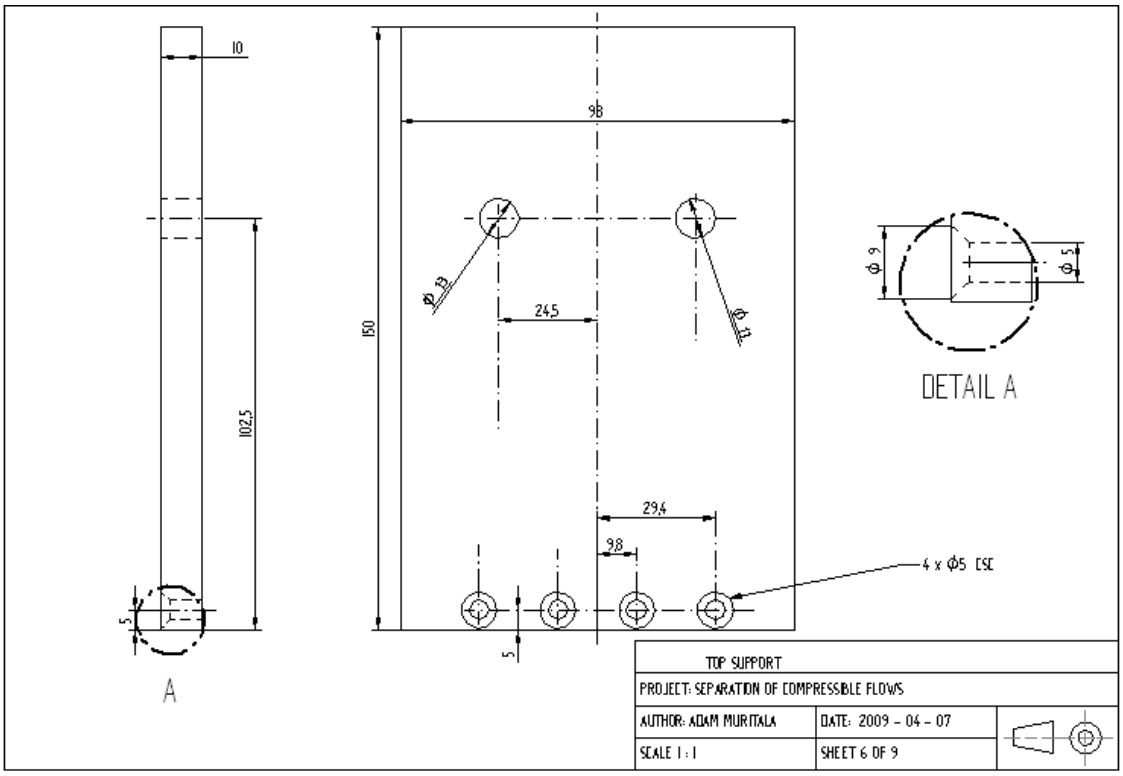

PLATE A6: The top support plate of 30^0 wall

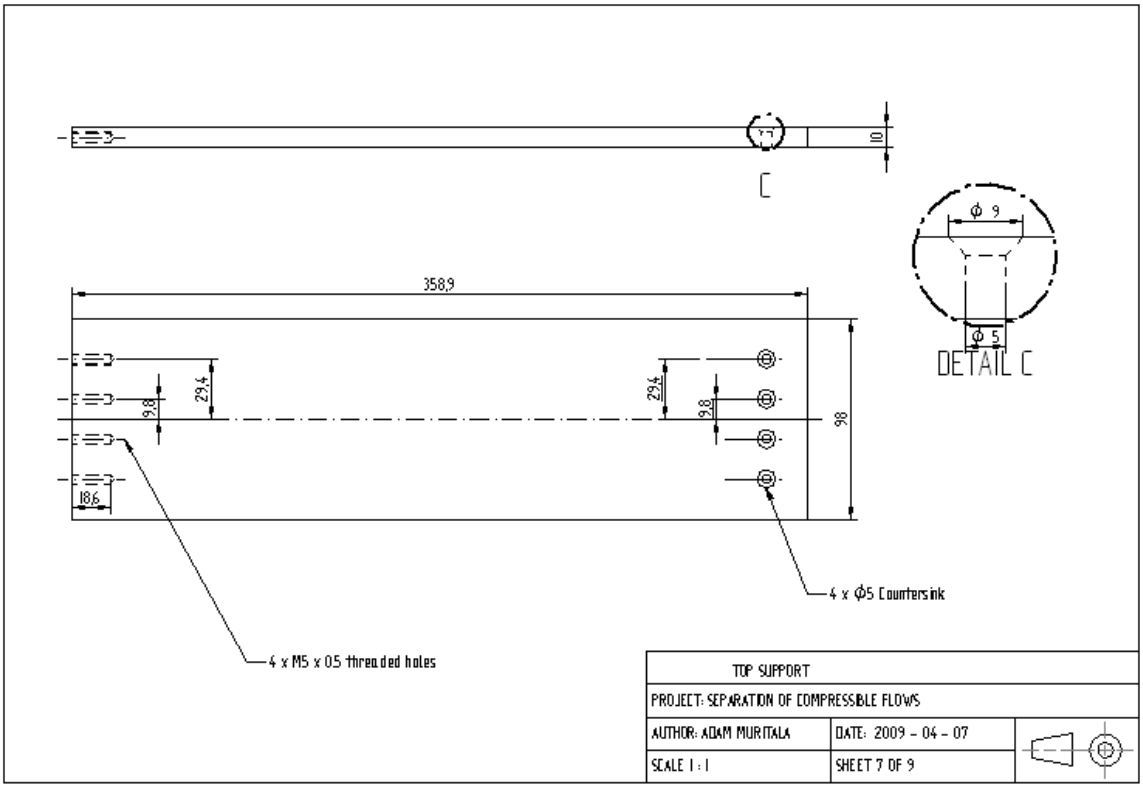

PLATE A7: The top arm plate of 30^0 wall

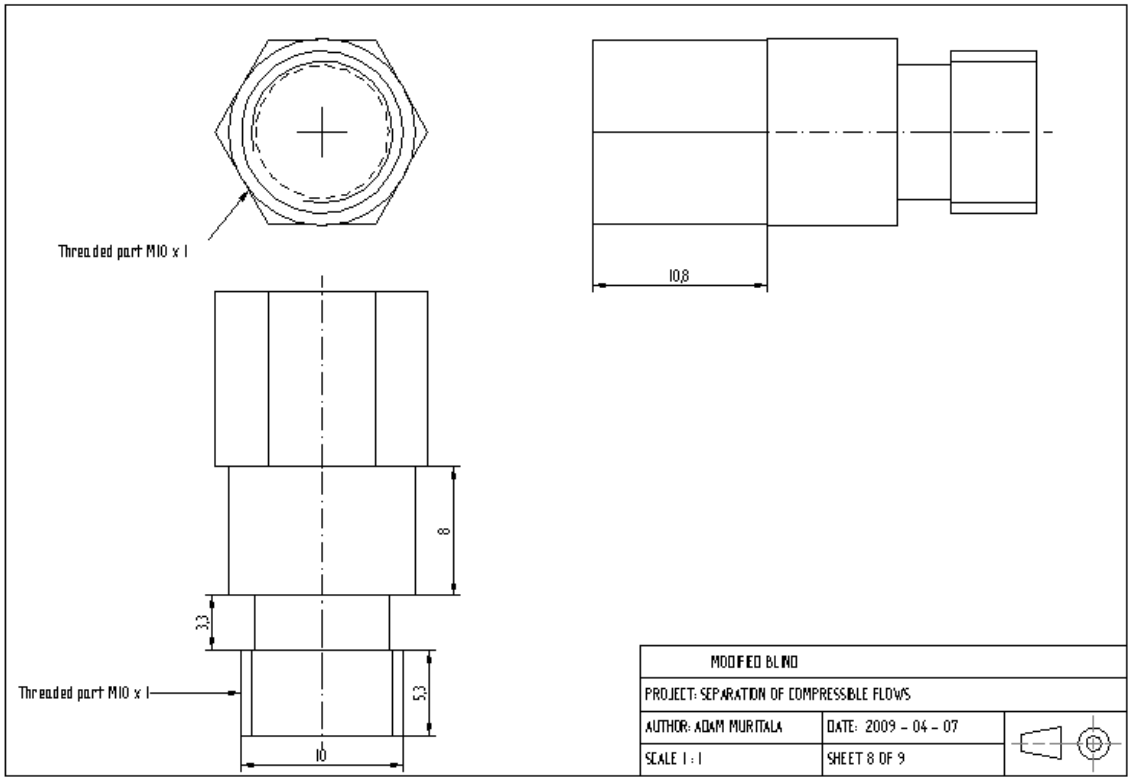

PLATE A8: The blind for transducer holes on 30^0 wall

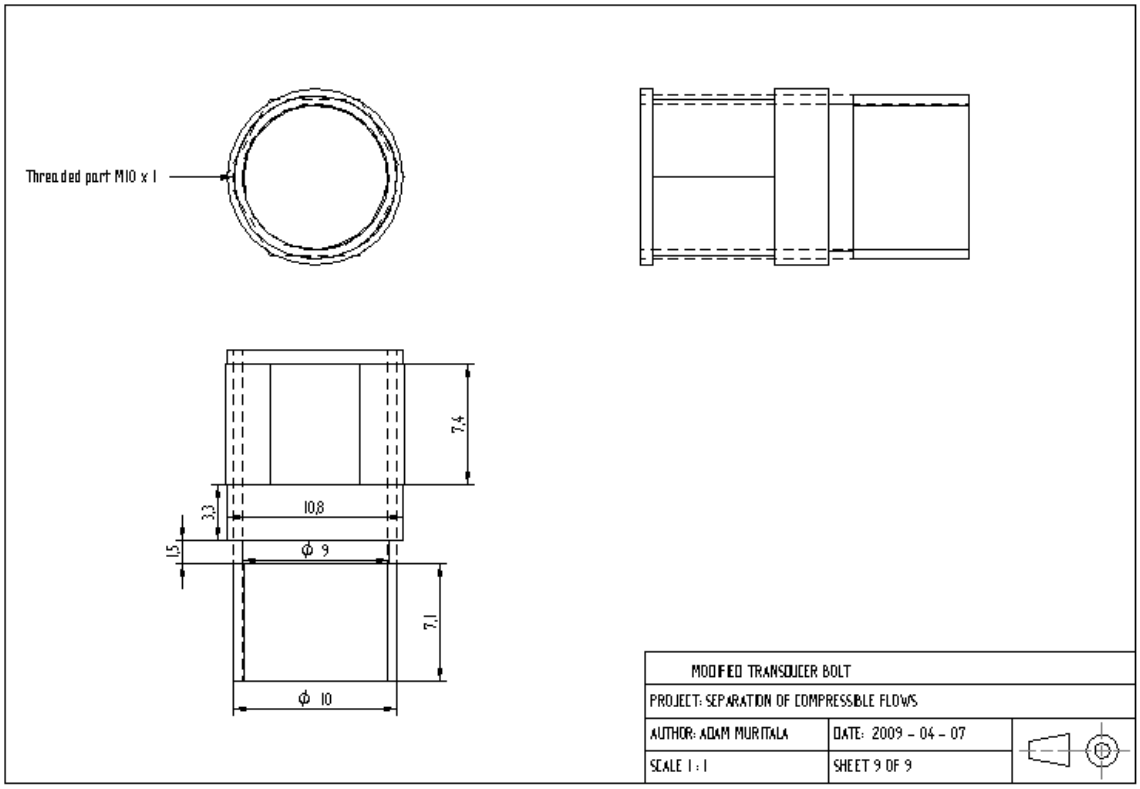

PLATE A9: The transducer support for 30^0 wall

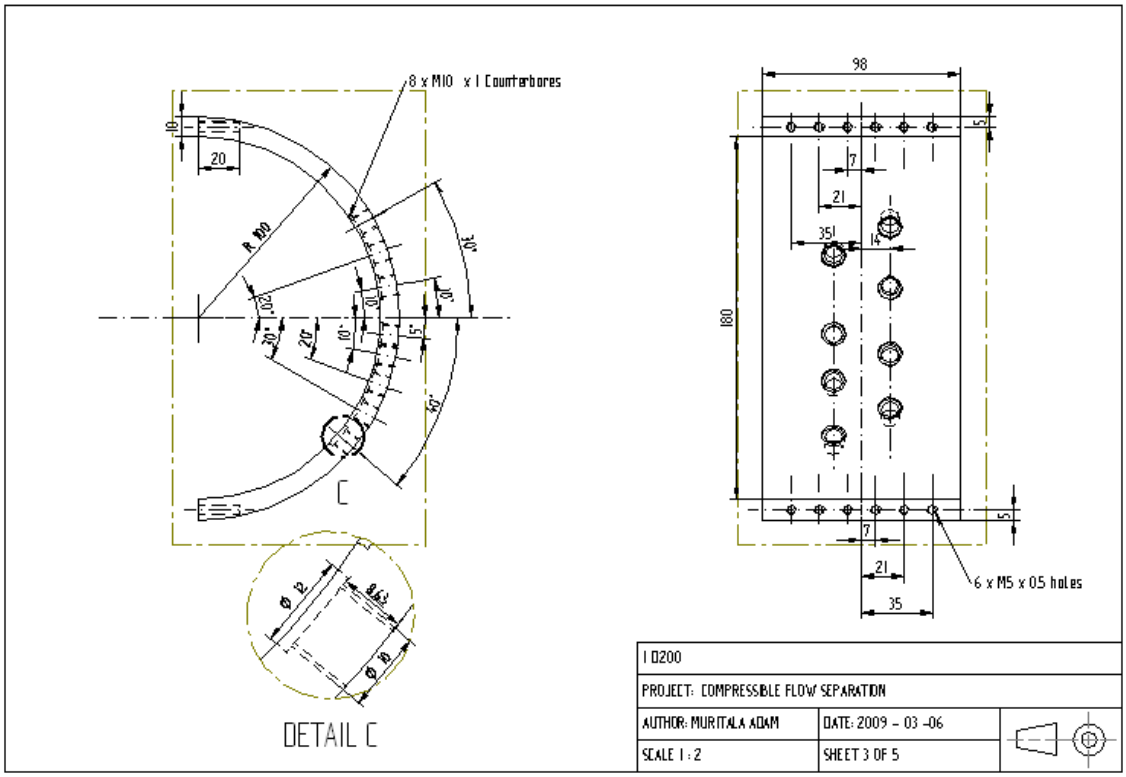

PLATE A10: The 200mm diameter wall

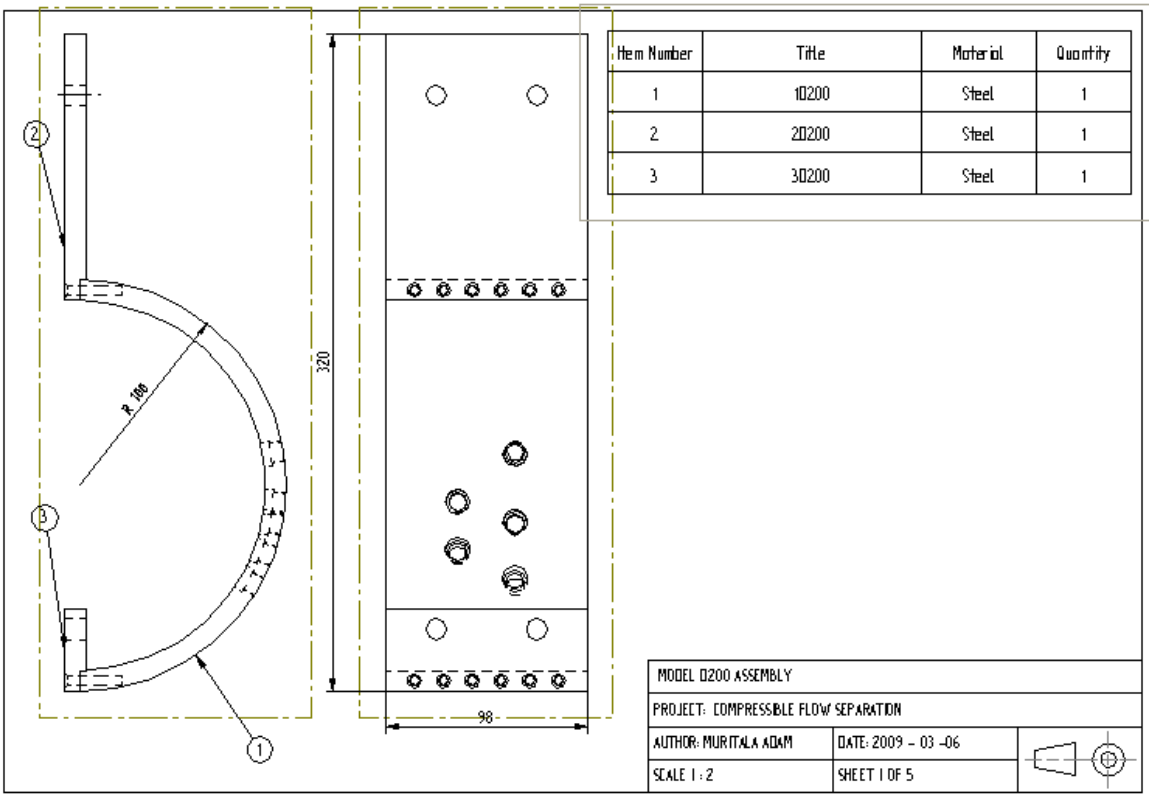

PLATE A11: The assembly of 200mm diameter wall

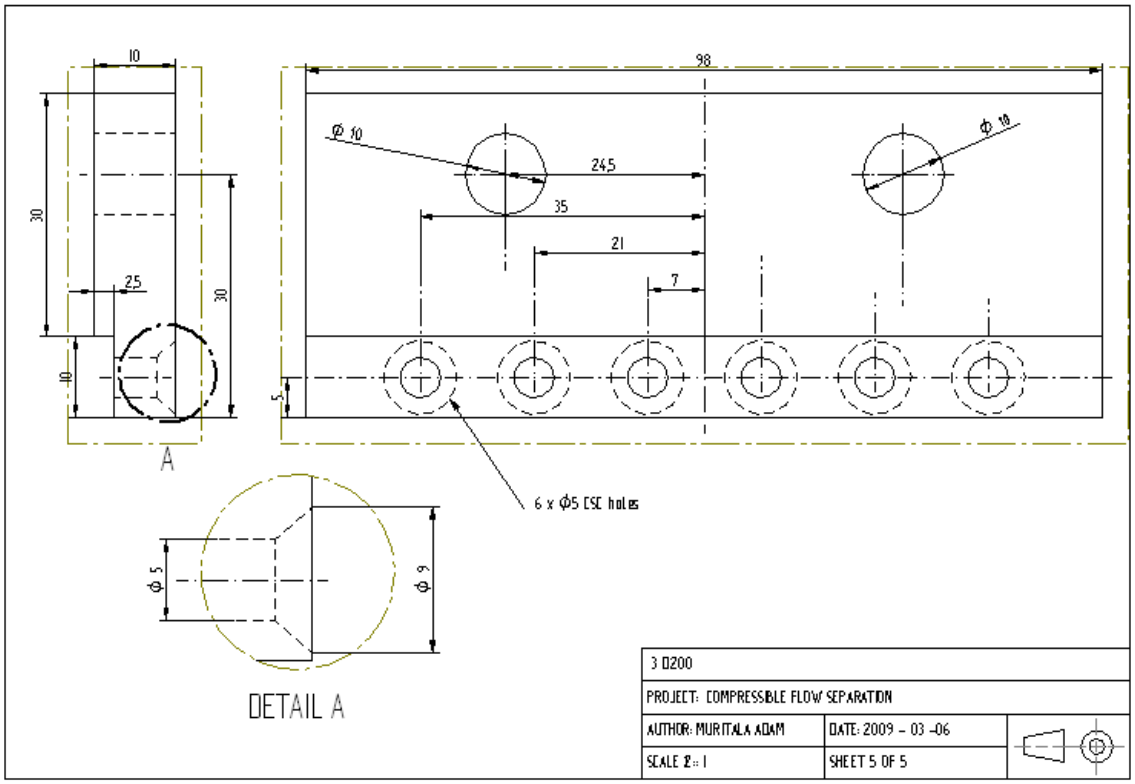

PLATE A12: The lower plate for 200mm diameter wall

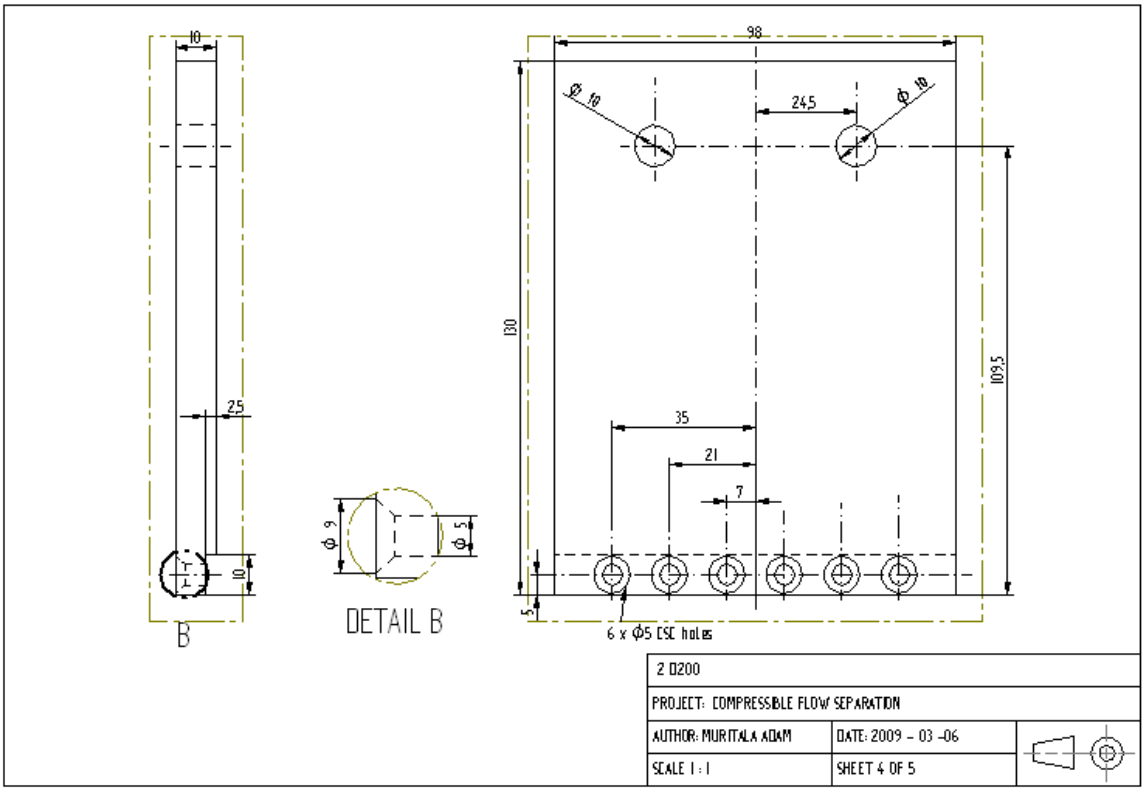

PLATE A13: The upper plate for 200mm diameter wall

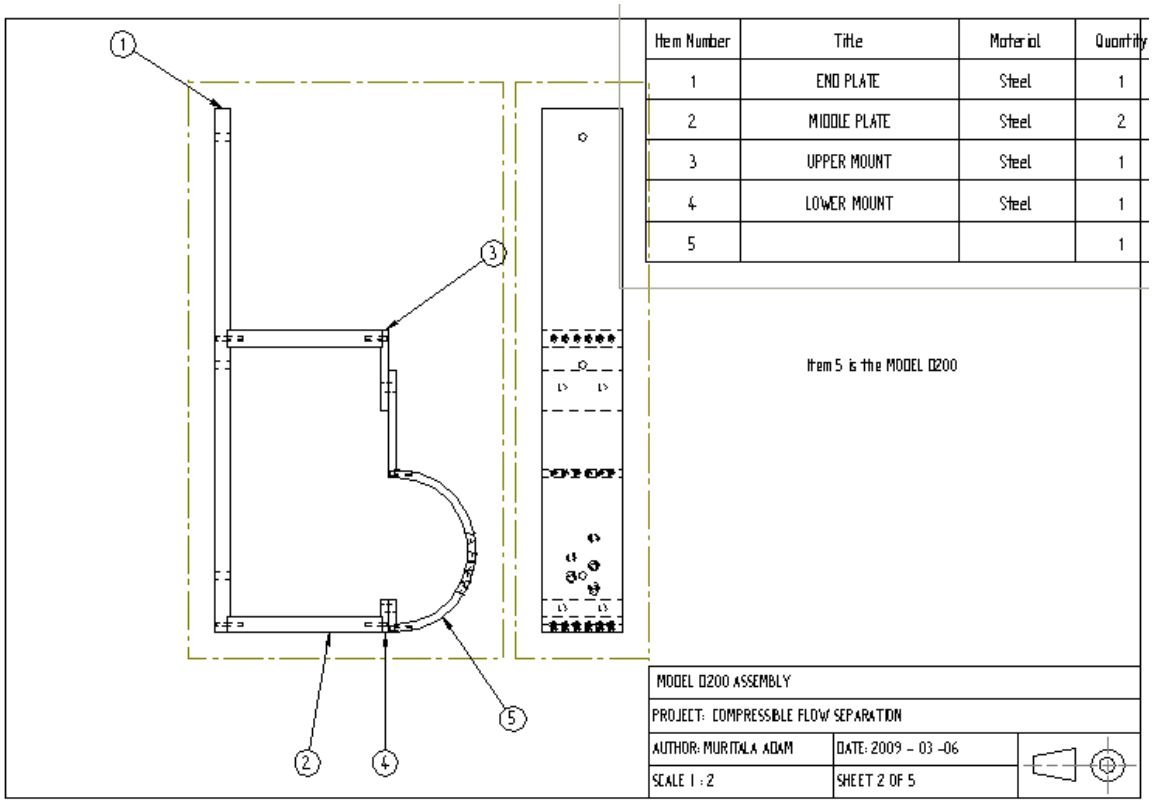

PLATE A14: The assembling of 200mm diameter wall with universal support

APPENDIX B: Experimental data for all the models

S/N	Driver Pressure (KPa)	Diaphragm Thickness (mm)	Operating Pressure (KPa)	Local Sound Speed (m/s)	Trigger Delay (□ s)	Shock Mach number (Mn)	Type of Model	Picture Number
1	**180**	**100**	**83.28**	**343.11**	**3000**	**1.350**	**C200**	**610**
2	**170**	**100**	**83.28**	**343.11**	**3200**	**1.350**	**C2000**	**611**
3	**280**	**125**	**83.28**	**343.11**	**3000**	**1.400**	**C200**	**631**
4	**280**	**125**	**83.28**	**343.11**	**3000**	**1.43**	**C200**	**612**
5	**360**	**125**	**83.28**	**343.11**	**2500**	**1.45**	**C200**	**613**
6	**360**	**150**	**83.34**	**343.58**	**2300**	**1.51**	**C200**	**629**
7	**400**	**150**	**82.6**	**344.16**	**700**	**1.537**	**C200**	**170**
8	**360**	**150**	**83.28**	**343.11**	**1800**	**1.55**	**C200**	**605**
9	**460**	**150**	**82.6**	**343.16**	**900**	**1.569**	**C200**	**175**
10	**400**	**150**	**83.28**	**343.11**	**1400**	**1.58**	**C200**	**602**
11	**480**	**150**	**82.6**	**343.52**	**900**	**1.586**	**C200**	**176**
12	**500**	**175**	**82.6**	**344.52**	**900**	**1.608**	**C200**	**177**
13	**500**	**175**	**83.28**	**343.11**	**2000**	**1.616**	**C200**	**616**
14	**480**	**175**	**83.28**	**343.11**	**2000**	**1.617**	**C200**	**609**
15	**340**	**150**	**82.80**	**342.82**	**750**	**1.50**	**C200**	**157**
16	**340**	**150**	**82.80**	**342.82**	**750**	**1.50**	**C200**	**158**
17	**340**	**150**	**82.80**	**342.82**	**750**	**1.50**	**C200**	**161**
18	**340**	**150**	**82.80**	**342.82**	**700**	**1.50**	**C200**	**162**
19	**340**	**150**	**82.80**	**345.45**	**700**	**1.49**	**C200**	**163**
20	**340**	**150**	**82.80**	**345.45**	**800**	**1.49**	**C200**	**164**
21	**340**	**150**	**82.80**	**345.45**	**900**	**1.49**	**C200**	**165**
22	**340**	**150**	**82.80**	**345.45**	**1050**	**1.50**	**C200**	**166**
23	**340**	**150**	**82.80**	**345.45**	**700**	**1.52**	**C200**	**167**
24	**340**	**150**	**82.80**	**345.45**	**800**	**1.52**	**C200**	**168**

25	**160**	**100**	**82.77**	**344.87**	**800**	**1.28**	**P30**	**210**
27	**400**	**150**	**82.6**	**344.16**	**800**	**1.54**	**C200**	**170**
28	**400**	**150**	**82.6**	**344.16**	**950**	**1.54**	**C200**	**171**
29	**400**	**150**	**82.6**	**344.16**	**1000**	**1.54**	**C200**	**172**
30	**420**	**150**	**82.6**	**344.16**	**700**	**1.55**	**C200**	**173**
31	**440**	**150**	**82.6**	**344.52**	**900**	**1.55**	**C200**	**174**
32	**460**	**150**	**82.6**	**344.52**	**900**	**1.57**	**C200**	**175**
33	**480**	**150**	**82.6**	**344.52**	**900**	**1.59**	**C200**	**-**
34	**480**	**175**	**82.6**	**344.52**	**900**	**1.59**	**C200**	**-**
35	**480**	**175**	**82.6**	**344.52**	**900**	**1.59**	**C200**	**176**
36	**500**	**175**	**82.6**	**344.52**	**900**	**1.61**	**C200**	**-**
37	**500**	**175**	**82.6**	**344.52**	**900**	**1.61**	**C200**	**177**
38	**500**	**175**	**82.6**	**344.52**	**900**	**1.61**	**C200**	**182**
39	**460**	**175**	**82.48**	**344.57**	**900**	**1.54**	**C200**	**-**
40	**500**	**175**	**82.48**	**344.57**	**900**	**1.61**	**C200**	**-**
41	**300**	**150**	**82.40**	**345.74**	**900**	**1.43**	**C200**	**-**
42	**280**	**100**	**82.40**	**345.74**	**1000**	**1.45**	**P30**	**195**
43	**270**	**100**	**82.50**	**344.98**	**1000**	**1.43**	**P30**	**196**
44	**260**	**100**	**82.50**	**344.98**	**600**	**1.43**	**P30**	**197**
45	**260**	**100**	**82.50**	**344.98**	**500**	**1.42**	**P30**	**199**
46	**230**	**100**	**82.50**	**344.98**	**600**	**1.39**	**P30**	**200**
47	**200**	**100**	**82.5**	**344.98**	**700**	**1.36**	**P30**	**201**
48	**180**	**100**	**82.5**	**344.98**	**700**	**1.35**	**P30**	**202**
49	**160**	**100**	**82.5**	**344.98**	**700**	**1.30**	**P30**	**203**
50	**340**	**150**	**83.1**	**346.32**	**900**	**1.50**	**C200**	**300**
51	**340**	**150**	**83.1**	**346.32**	**1500**	**1.50**	**C200**	**301**
52	**150**	**100**	**82.77**	**344.87**	**700**	**1.31**	**P30**	**207**
53	**160**	**100**	**82.77**	**344.87**	**800**	**1.28**	**P30**	**208**
54	**160**	**100**	**82.77**	**344.87**	**600**	**1.266**	**P30**	**209**
55	**180**	**100**	**82.83**	**344.98**	**700**	**1.36**	**P30**	**227**
56	**350**	**150**	**82.83**	**346.00**	**450**	**1.45**	**P30**	**230**
57	**180**	**100**	**82.83**	**345.74**	**600**	**1.25**	**P30**	**232**
58	**200**	**100**	**82.83**	**345.74**	**900**	**1.34**	**P30**	**233**
59	**200**	**100**	**82.83**	**345.74**	**700**	**1.34**	**P30**	**234**
60	**180**	**100**	**82.95**	**344.28**	**700**	**1.30**	**P30**	**231**
61	**180**	**100**	**82.95**	**344.28**	**550**	**1.32**	**P30**	**235**

62	**190**	**100**	**82.95**	**344.28**	**1090**	**1.30**	**P30**	**236**
63	**190**	**100**	**82.95**	**344.28**	**900**	**1.38**	**P30**	**237**
64	**190**	**100**	**82.95**	**344.28**	**1440**	**1.32**	**P30**	**238**
65	**190**	**100**	**82.95**	**344.28**	**980**	**1.32**	**P30**	**239**
66	**190**	**100**	**82.95**	**344.28**	**500**	**1.32**	**P30**	**240**
67	**190**	**100**	**82.95**	**344.28**	**400**	**1.32**	**P30**	**241**
68	**190**	**100**	**82.95**	**345.28**	**700**	**1.29**	**P30**	**242**
69	**190**	**100**	**82.95**	**345.28**	**900**	**1.31**	**P30**	**243**
70	**190**	**100**	**82.95**	**345.28**	**1188**	**1.31**	**P30**	**244**
71	**190**	**100**	**82.95**	**345.28**	**1050**	**1.30**	**P30**	**245**
72	**190**	**100**	**83.13**	**344.75**	**1200**	**1.32**	**P30**	**248**
73	**190**	**100**	**83.13**	**344.75**	**1300**	**1.32**	**P30**	**249**
74	**190**	**100**	**83.13**	**344.75**	**1100**	**1.32**	**P30**	**251**
75	**190**	**100**	**83.13**	**344.98**	**950**	**1.32**	**P30**	**252**
76	**190**	**100**	**83.13**	**344.98**	**900**	**1.32**	**P30**	**253**
77	**190**	**100**	**83.13**	**344.98**	**920**	**1.32**	**P30**	**254**
78	**340**	**150**	**83.13**	**345.45**	**750**	**1.51**	**P30**	**257**
79	**360**	**150**	**83.13**	**345.45**	**1000**	**1.51**	**P30**	**258**
80	**360**	**150**	**83.13**	**345.45**	**900**	**1.51**	**P30**	**259**
81	**360**	**150**	**83.13**	**345.45**	**1100**	**1.51**	**P30**	**260**

S/N	**Driver Pressure (KPa)**	**Diaphragm Thickness (mm)**	**Operating Pressure (KPa)**	**Local Sound Speed (m/s)**	**Trigger Delay (□ s)**	**Shock Mach number (Mn)**	**Type of Model**	**Picture Number**
82	**360**	**150**	**83.13**	**344.75**	**1200**	**1.51**	**P30**	**-**
83	**190**	**100**	**83.42**	**344.87**	**900**	**1.34**	**P30**	**266**
84	**190**	**100**	**83.42**	**344.87**	**1080**	**1.34**	**P30**	**267**
85	**190**	**100**	**83.42**	**344.87**	**1296**	**1.34**	**P30**	**268**
86	**190**	**100**	**83.42**	**344.87**	**1400**	**1.34**	**P30**	**269**
87	**190**	**100**	**83.42**	**344.87**	**2000**	**1.34**	**P30**	**270**
88	**190**	**100**	**83.42**	**344.87**	**972**	**1.34**	**P30**	**271**
89	**190**	**100**	**83.42**	**344.87**	**950**	**1.34**	**P30**	**272**
90	**190**	**100**	**83.42**	**344.87**	**920**	**1.34**	**P30**	**273**
91	**190**	**100**	**83.42**	**344.87**	**900**	**1.34**	**P30**	**274**
92	**190**	**100**	**83.42**	**344.87**	**1000**	**1.34**	**P30**	**275**
93	**190**	**100**	**83.42**	**344.87**	**900**	**1.34**	**P30**	**276**

94	**340**	**150**	**83.42**	**346.03**	**900**	**1.50**	**P30**	**277**
95	**340**	**150**	**83.42**	**346.03**	**1100**	**1.50**	**P30**	**278**
96	**340**	**150**	**83.42**	**346.03**	**1300**	**1.50**	**P30**	**279**
97	**190**	**100**	**83.30**	**345.33**	**1500**	**1.34**	**P30**	**283**
98	**340**	**150**	**83.30**	**345.33**	**1300**	**1.52**	**P30**	**284**
99	**190**	**100**	**83.30**	**345.33**	**1300**	**1.33**	**P30**	**285**
100	**190**	**100**	**83.30**	**345.33**	**1600**	**1.33**	**P30**	**286**
101	**340**	**150**	**83.30**	**345.33**	**1300**	**1.51**	**P30**	**287**
102	**340**	**150**	**83.30**	**345.33**	**1100**	**1.51**	**P30**	**288**
103	**340**	**150**	**83.19**	**344.98**	**2000**	**1.51**	**P30**	**293**
104	**340**	**150**	**83.19**	**344.98**	**2400**	**1.51**	**P30**	**295**
105	**340**	**150**	**83.19**	**344.98**	**3000**	**1.51**	**P30**	**-**
106	**340**	**150**	**83.19**	**344.98**	**2300**	**1.51**	**P30**	**-**

S/N	**Driver Pressure (KPa)**	**Diaphragm Thickness (mm)**	**Operating Pressure (KPa)**	**Local Sound Speed (m/s)**	**Trigger Delay (□ s)**	**Shock Mach number (Mn)**	**Type of Model**	**Picture Number**
107	**340**	**150**	**83.10**	**346.32**	**1000**	**1.44**	**C200**	**305**
108	**340**	**150**	**83.10**	**346.32**	**1200**	**1.50**	**C200**	**306**
109	**340**	**150**	**83.10**	**346.72**	**1400**	**1.50**	**C200**	**307**
110	**340**	**150**	**83.10**	**346.72**	**1600**	**1.50**	**C200**	**308**
111	**340**	**150**	**82.88**	**345.80**	**1500**	**1.50**	**C200**	**310**
112	**340**	**150**	**82.88**	**345.80**	**500**	**1.50**	**C200**	**311**
113	**340**	**150**	**82.88**	**345.80**	**800**	**1.50**	**C200**	**312**
114	**340**	**150**	**82.88**	**345.80**	**650**	**1.50**	**C200**	**313**
115	**340**	**150**	**82.80**	**342.82**	**750**	**1.50**	**C200**	**157**
116	**340**	**150**	**82.8**	**342.82**	**750**	**1.50**	**C200**	**158**
117	**340**	**150**	**82.80**	**342.82**	**750**	**1.50**	**C200**	**161**
118	**340**	**150**	**82.80**	**342.82**	**700**	**1.50**	**C200**	**162**
119	**340**	**150**	**82.80**	**345.45**	**700**	**1.49**	**C200**	**163**
120	**340**	**150**	**82.80**	**345.45**	**800**	**1.49**	**C200**	**164**
121	**340**	**150**	**82.80**	**345.45**	**900**	**1.49**	**C200**	**165**
122	**345**	**150**	**82.80**	**345.45**	**1050**	**1.50**	**C200**	**166**
123	**360**	**150**	**82.80**	**345.45**	**700**	**1.52**	**C200**	**167**
124	**360**	**150**	**82.80**	**345.45**	**800**	**1.52**	**C200**	**168**
125	**340**	**150**	**82.87**	**345.45**	**1300**	**1.50**	**C200**	**317**

126	**340**	**150**	**82.87**	**345.45**	**1300**	**1.50**	**C200**	**318**
127	**340**	**150**	**82.87**	**345.45**	**300**	**1.50**	**C200**	**319**
128	**340**	**150**	**82.87**	**345.45**	**400**	**1.50**	**C200**	**320**
129	**340**	**150**	**82.87**	**345.45**	**800**	**1.50**	**C200**	**321**
130	**340**	**150**	**82.87**	**345.45**	**1500**	**1.50**	**C200**	**322**
131	**340**	**150**	**82.87**	**345.45**	**1600**	**1.50**	**C200**	**323**

S/N	**Driver Pressure (KPa)**	**Diaphragm Thickness (mm)**	**Operating Pressure (KPa)**	**Local Sound Speed (m/s)**	**Trigger Delay (□ s)**	**Shock Mach number (Mn)**	**Type of Model**	**Picture Number**
132	**340**	**150**	**82.87**	**345.45**	**1400**	**1.50**	**C200**	**324**
133	**340**	**150**	**82.87**	**345.45**	**1300**	**1.50**	**C200**	**325**
134	**340**	**150**	**82.87**	**345.45**	**1200**	**1.50**	**C200**	**326**
135	**340**	**150**	**82.87**	**345.45**	**1100**	**1.50**	**C200**	**327**
136	**340**	**150**	**82.87**	**345.45**	**1000**	**1.50**	**C200**	**328**
137	**340**	**150**	**82.87**	**345.45**	**900**	**1.50**	**C200**	**329**
138	**360**	**150**	**82.87**	**346.03**	**1200**	**1.51**	**C200**	**330**
139	**290**	**100**	**83.30**	**345.45**	**1200**	**-**		
140	**360**	**150**	**83.30**	**345.45**	**1200**	**1.48**	**C400**	**367**
141	**370**	**150**	**83.30**	**345.45**	**1400**	**1.51**	**C400**	**368**
142	**370**	**150**	**83.30**	**345.45**	**1600**	**1.51**	**C400**	**369**
143	**370**	**150**	**83.30**	**345.45**	**1800**	**1.51**	**C400**	**370**
144	**480**	**175**	**83.30**	**345.45**	**1200**	**1.57**	**C400**	**372**
145	**480**	**175**	**83.30**	**345.45**	**1400**	**1.61**	**C400**	**373**
146	**480**	**175**	**83.30**	**345.45**	**1600**	**1.61**	**C400**	**374**
147	**480**	**175**	**83.30**	**345.45**	**2000**	**1.61**	**C400**	**376**
148	**480**	**175**	**83.30**	**345.45**	**1800**	**1.61**	**C400**	**377**
149	**480**	**175**	**83.39**	**344.57**	**1450**	**1.58**	**C400**	**378**
150	**480**	**175**	**83.39**	**344.57**	**1550**	**1.61**	**C400**	**379**
151	**480**	**175**	**83.39**	**344.57**	**1750**	**1.61**	**C400**	**380**
152	**340**	**150**	**83.58**	**344.87**	**1200**	**1.48**	**P30**	**383**
153	**340**	**150**	**83.58**	**344.87**	**1400**	**1.48**	**P30**	**389**
154	**340**	**150**	**83.58**	**344.87**	**1100**	**1.48**	**P30**	**390**
155	**340**	**150**	**83.58**	**344.87**	**1000**	**1.48**	**P30**	**391**
156	**360**	**150**	**83.00**	**345.33**	**1400**	**1.48**	**P30**	**396**

S/N	Driver Pressure (KPa)	Diaphragm Thickness (mm)	Operating Pressure (KPa)	Local Sound Speed (m/s)	Trigger Delay (□ s)	Shock Mach number (Mn)	Type of Model	Picture Number
157	**480**	**175**	**82.8**	**345.33**	**900**	**1.645**	**C200**	**333**
158	**480**	**175**	**82.8**	**345.33**	**1300**	**1.645**	**C200**	**334**
159	**480**	**175**	**82.8**	**345.33**	**1500**	**1.645**	**C200**	**335**
160	**480**	**175**	**82.8**	**345.33**	**1600**	**1.609**	**C200**	**336**
161	**480**	**175**	**82.8**	**345.33**	**1800**	**1.609**	**C200**	**337**
162	**480**	**175**	**82.8**	**345.33**	**2000**	**1.609**	**C200**	**338**
163	**480**	**175**	**82.8**	**345.33**	**600**	**1.609**	**C200**	**339**
164	**480**	**175**	**82.8**	**345.33**	**1000**	**1.609**	**C200**	**340**
165	**480**	**175**	**82.8**	**345.33**	**2000**	**1.609**	**C200**	**341**
166	**480**	**175**	**82.8**	**345.33**	**1500**	**1.609**	**C200**	**342**
167	**280**	**100**	**83.42**	**345.33**	**1100**	**1.45**	**C200**	**345**
168	**270**	**100**	**83.42**	**345.33**	**1700**	**1.39**	**C200**	**346**
169	**280**	**100**	**83.42**	**345.33**	**2000**	**1.42**	**C200**	**347**
170	**280**	**100**	**83.42**	**345.33**	**2200**	**1.42**	**C200**	**348**
171	**280**	**100**	**83.42**	**345.33**	**2500**	**1.42**	**C200**	**349**
172	**280**	**100**	**83.42**	**345.33**	**2700**	**1.42**	**C200**	**350**
173	**280**	**100**	**83.42**	**345.33**	**1400**	**1.42**	**C200**	**351**
174	**280**	**100**	**83.42**	**345.33**	**1550**	**1.42**	**C200**	**352**
175	**360**	**150**	**83.00**	**345.33**	**1400**	**1.48**	**P30**	**396**
176	**370**	**150**	**83.00**	**345.33**	**1400**	**150**	**P30**	**353-**
177	**370**	**150**	**83.00**	**345.33**	**1200**	**1.51**	**P30**	**404**
178	**380**	**150**	**83.00**	**345.33**	**1300**	**1.48**	**P30**	**405**
179	**380**	**150**	**83.00**	**345.33**	**1000**	**1.48**	**P30**	**406**
180	**380**	**150**	**83.00**	**345.33**	**1400**	**1.48**	**P30**	**407**
181	**380**	**150**	**83.04**	**345.45**	**1300**	**1.51**	**P30**	**409**

S/N	Driver Pressure (KPa)	Diaphragm Thickness (mm)	Operating Pressure (KPa)	Local Sound Speed (m/s)	Trigger Delay (□ s)	Shock Mach number (Mn)	Type of Model	Picture Number
182	**380**	**150**	**82.76**	**345.74**	**1300**	**1.51**	**P90**	**448**
183	**380**	**150**	**82.76**	**345.74**	**1100**	**1.51**	**P90**	**449**
184	**380**	**150**	**82.76**	**345.74**	**900**	**1.51**	**P90**	**450**
185	**380**	**150**	**82.76**	**345.74**	**1600**	**1.51**	**P90**	**451**

186	**280**	**100**	**82.76**	**345.74**	**1600**	**1.39**	**P90**	**452**
187	**280**	**100**	**82.76**	**345.74**	**1300**	**1.39**	**P90**	**453**
188	**280**	**100**	**82.76**	**345.74**	**900**	**1.39**	**P90**	**454**
189	**160**	**100**	**82.76**	**345.74**	**1600**	**1.31**	**P90**	**455**
190	**500**	**175**	**82.95**	**344.28**	**1000**	**1.58**	**P90**	**460**
191	**500**	**175**	**82.95**	**344.28**	**1300**	**1.60**	**P90**	**461**
192	**505**	**175**	**82.95**	**344.28**	**1200**	**161**	**P90**	**462**
193	**505**	**175**	**82.95**	**344.28**	**1400**	**1.61**	**P90**	**463**
194	**500**	**175**	**82.95**	**344.28**	**1300**	**1.61**	**P90**	**464**
195	**380**	**150**	**83.22**	**344.28**	**1400**	**1.48**	**P90**	**467**
196	**400**	**150**	**83.22**	**344.28**	**1300**	**1.51**	**P90**	**470**
197	**400**	**150**	**83.22**	**344.28**	**1200**	**1.51**	**P90**	**479**
198	**500**	**175**	**83.22**	**344.28**	**1300**	**1.60**	**P90**	**480**
199	**500**	**175**	**83.22**	**344.28**	**1600**	**1.60**	**P90**	**481**
200	**400**	**150**	**83.22**	**344.28**	**1300**	**1.51**	**P90**	**495**
201	**400**	**150**	**83.22**	**344.28**	**1100**	**1.51**	**P90**	**496**
202	**400**	**150**	**83.22**	**344.28**	**1500**	**1.51**	**P90**	**497**
203	**400**	**150**	**83.22**	**344.28**	**1700**	**1.51**	**P90**	**498**
204	**400**	**150**	**83.22**	**344.28**	**1000**	**1.51**	**P90**	**499**
205	**400**	**150**	**83.22**	**344.28**	**1200**	**1.51**	**P90**	**500**
206	**400**	**150**	**83.22**	**344.28**	**1400**	**1.51**	**P90**	**501**

S/N	**Driver Pressure (KPa)**	**Diaphragm Thickness (mm)**	**Operating Pressure (KPa)**	**Local Sound Speed (m/s)**	**Trigger Delay (□ s)**	**Shock Mach number (Mn)**	**Type of Model**	**Picture Number**
207	**400**	**150**	**83.44**	**344.63**	**1300**	**1.51**	**P90**	**505**
208	**400**	**150**	**83.44**	**344.63**	**1200**	**1.51**	**P90**	**508**
209	**400**	**150**	**83.44**	**344.63**	**1400**	**1.51**	**P90**	**531**
210	**400**	**150**	**83.44**	**344.63**	**1100**	**1.51**	**P90**	**532**
211	**400**	**150**	**83.44**	**344.63**	**1000**	**1.51**	**P90**	**533**
212	**400**	**150**	**83.44**	**344.63**	**1200**	**1.51**	**P90**	**534**
213	**400**	**150**	**83.44**	**344.63**	**1300**	**1.51**	**P90**	**535**
214	**400**	**150**	**83.44**	**344.63**	**1500**	**1.51**	**P90**	**536**
215	**400**	**150**	**83.44**	**344.63**	**1600**	**1.51**	**P90**	**537**
216	**400**	**150**	**83.44**	**344.63**	**1700**	**1.51**	**P90**	**538**
217	**400**	**150**	**83.44**	**344.63**	**1800**	**1.51**	**P90**	**539**

218	**400**	**150**	**83.42**	**344.52**	**1800**	**1.51**	**P90**	**545**
219	**400**	**150**	**83.42**	**344.52**	**1900**	**1.51**	**P90**	**547**
220	**200**	**150**	**83.42**	**344.52**	**1000**	**1.42**	**P90**	**550**
221	**280**	**150**	**83.42**	**344.52**	**1700**	**1.42**	**P90**	**551**
222	**260**	**125**	**83.42**	**344.74**	**1400**	**1.40**	**P90**	**552**
223	**240**	**100**	**83.42**	**344.74**	**1400**	**1.40**	**P90**	**553**
224	**200**	**100**	**83.42**	**344.74**	**1400**	**1.34**	**P90**	**554**
225	**220**	**100**	**83.42**	**344.74**	**1800**	**1.34**	**P90**	**555**
226	**170**	**100**	**83.42**	**344.74**	**1400**	**1.27**	**P90**	**556**
227	**150**	**100**	**83.42**	**344.74**	**3000**	**1.27**	**P90**	**557**
228	**140**	**100**	**83.42**	**344.86**	**3200**	**1.21**	**P90**	**559**
229	**260**	**150**	**83.42**	**344.86**	**2200**	**1.37**	**P90**	**564**
230	**100**	**75**	**83.42**	**344.86**	**3600**	**1.19**	**P90**	**560**
231	**280**	**150**	**83.42**	**344.86**	**3600**	**1.37**	**P90**	**568**
232	**280**	**150**	**83.42**	**344.86**	**3400**	**1.36**	**P90**	**570**
233	**290**	**150**	**83.42**	**344.86**	**2800**	**1.40**	**P90**	**572**

APPENDIX C: Experimental pictures for 30Degree Model

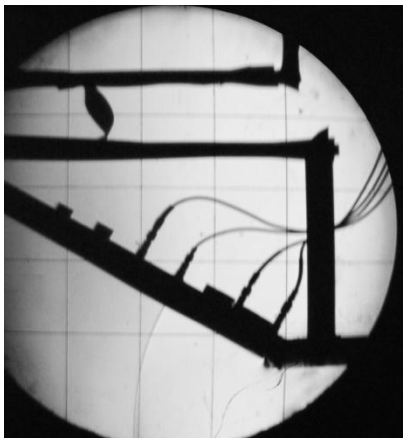

207

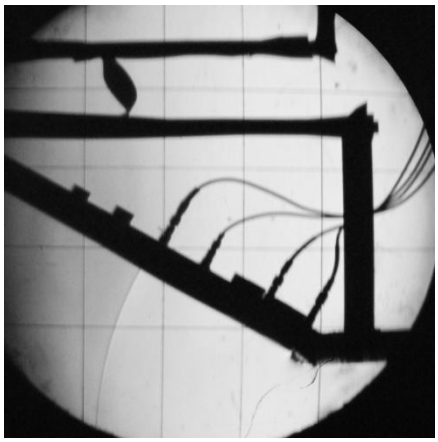

208

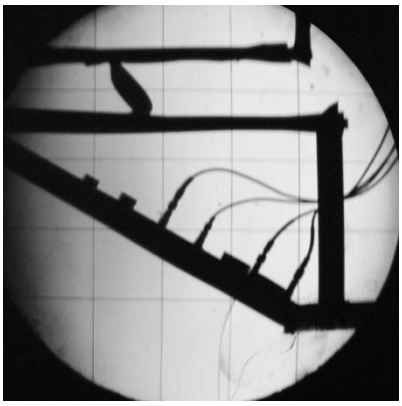

209

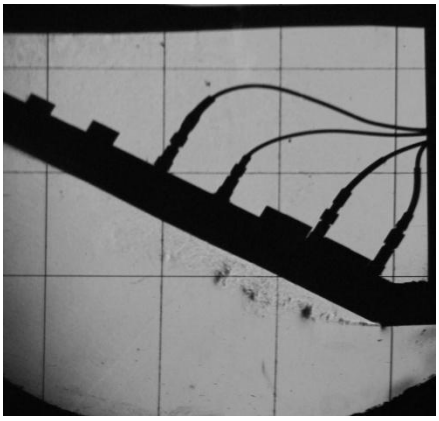

210

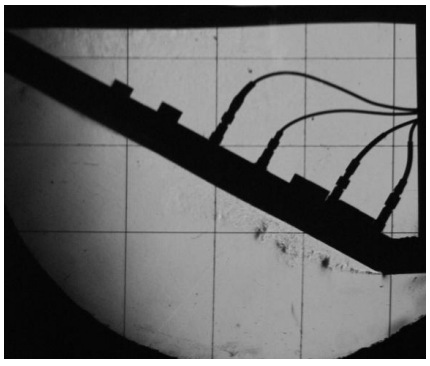

235

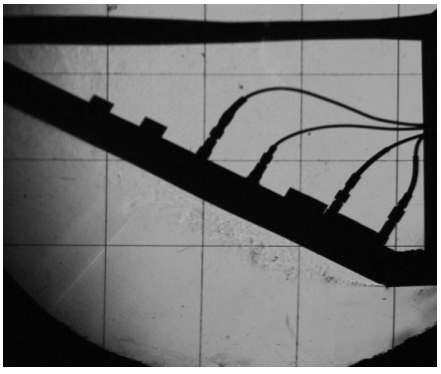

236

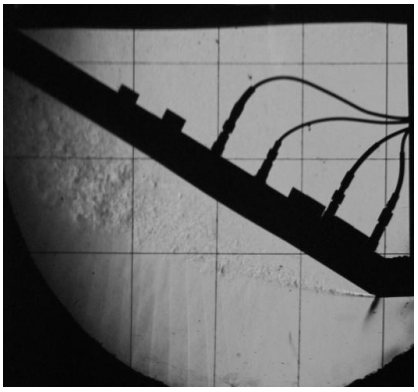

237

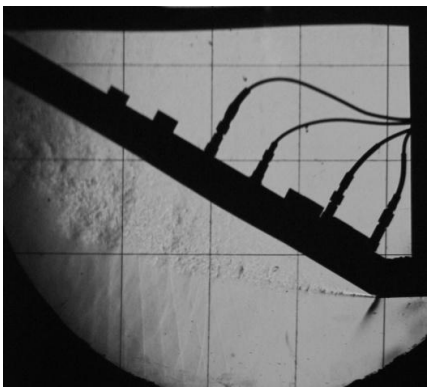

238

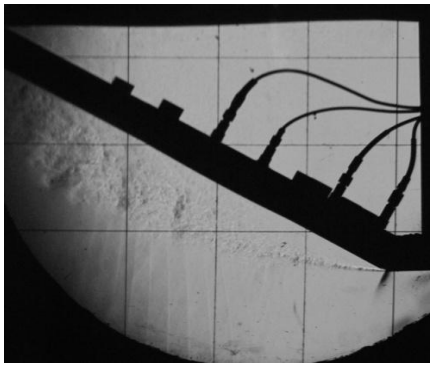

239

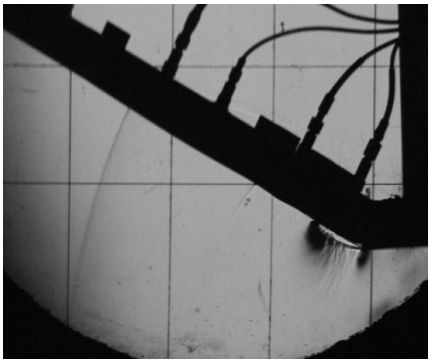

257

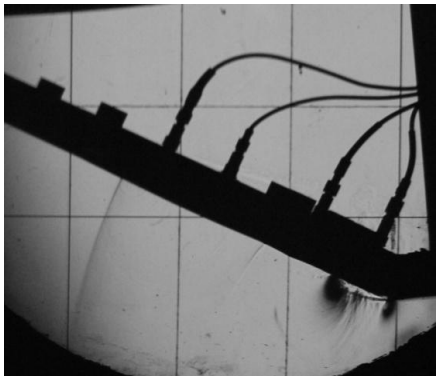

258

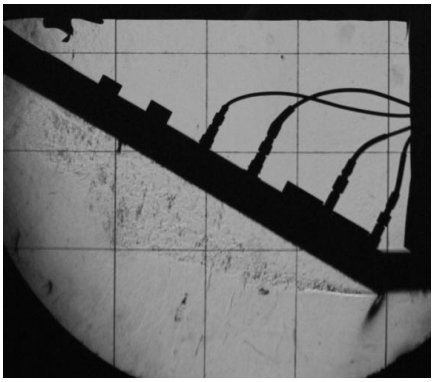

259

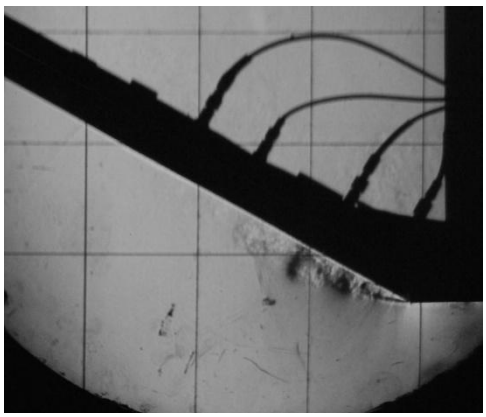

270

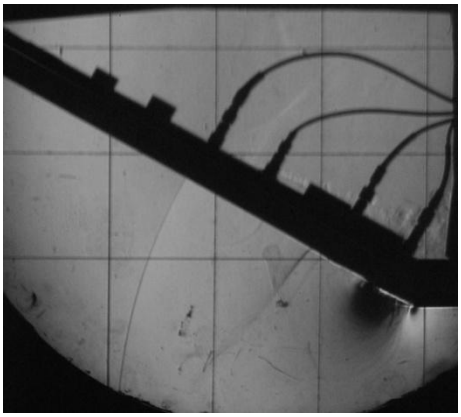

277

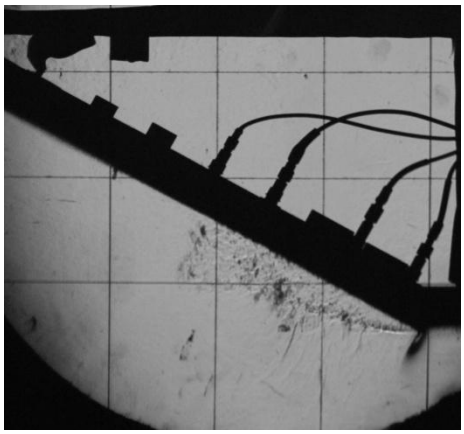

293

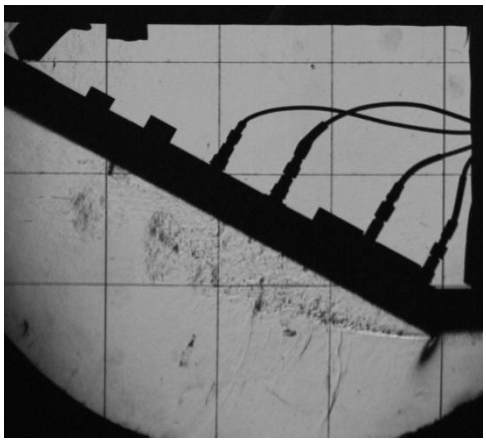

295

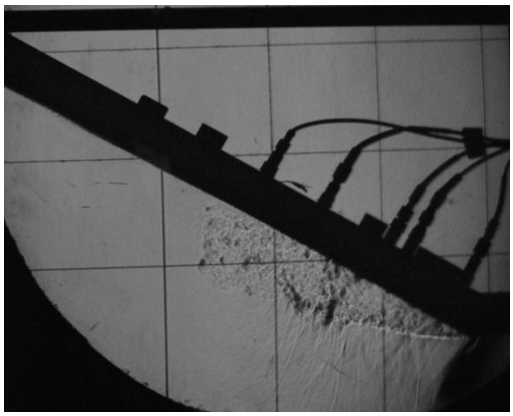

425

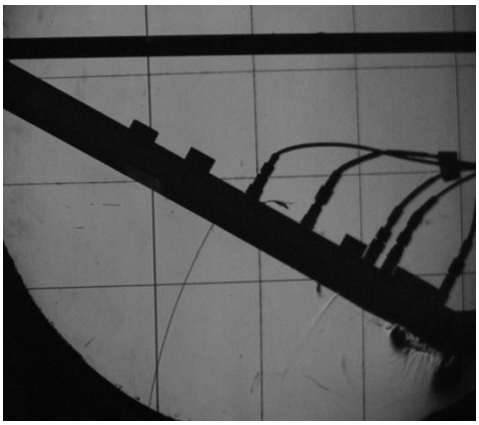

422

APPENDIX D: Experimental pictures for 90°corner wall

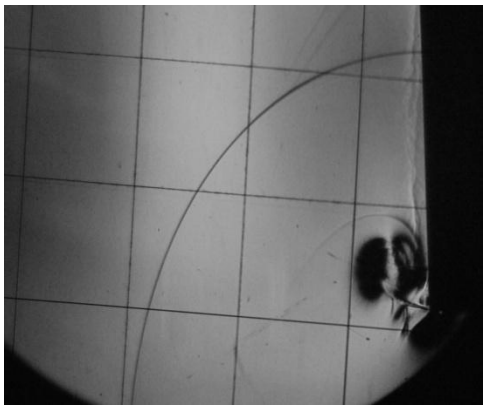

495

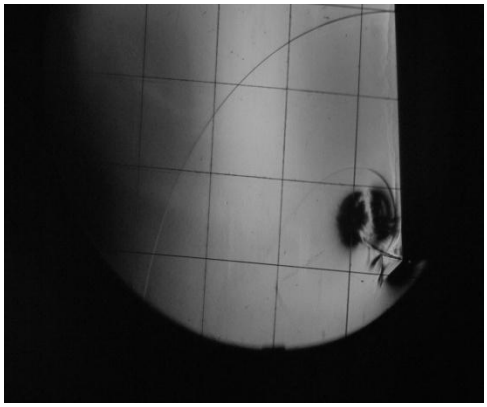

496

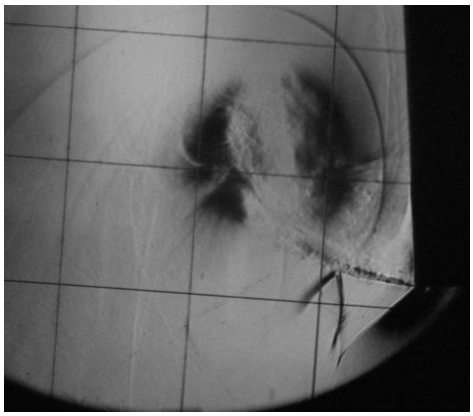

497

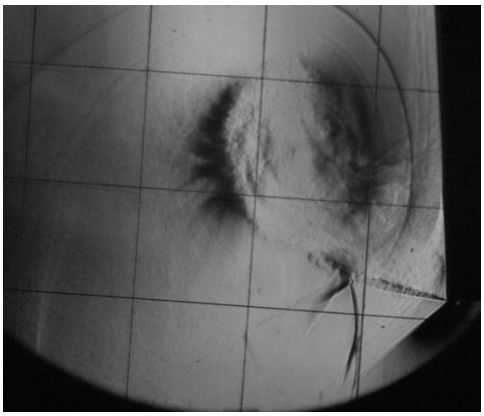

498

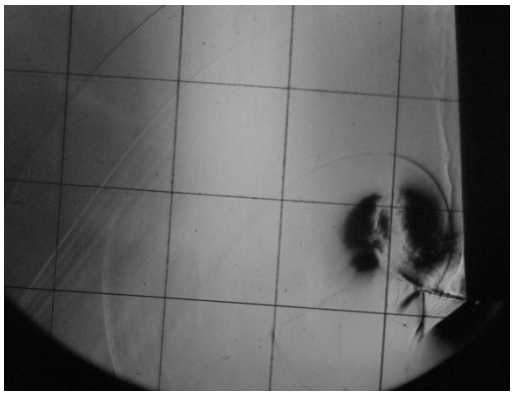

500

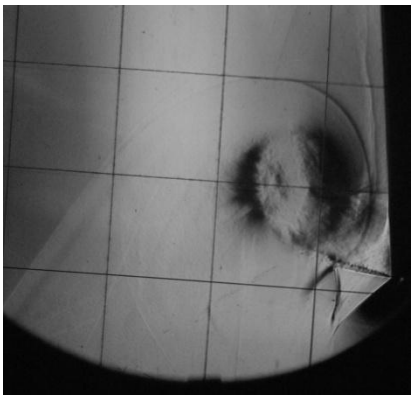

501

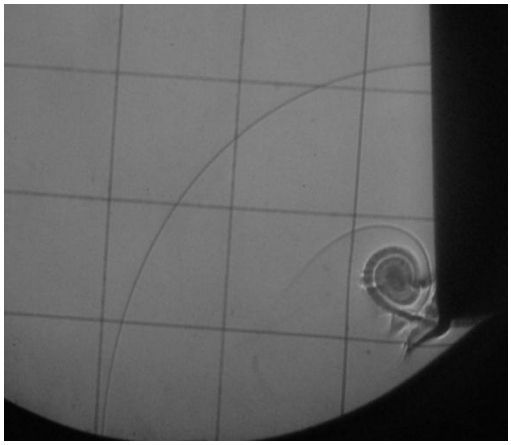

531

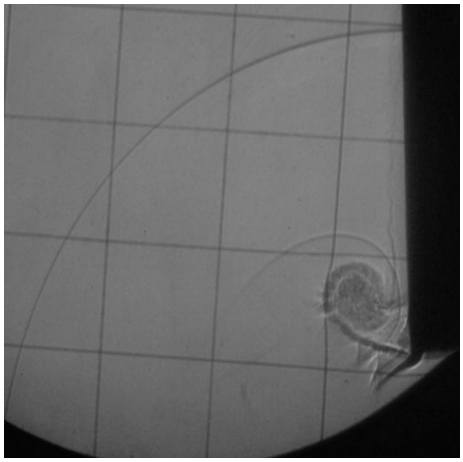

532

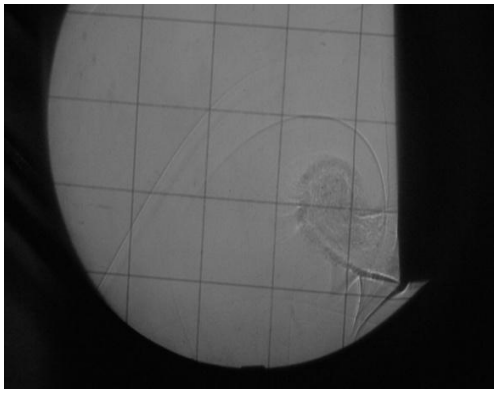

533

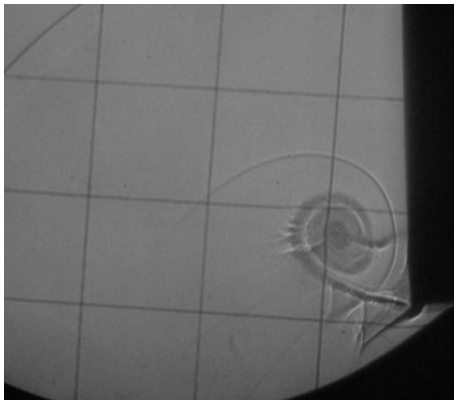

534

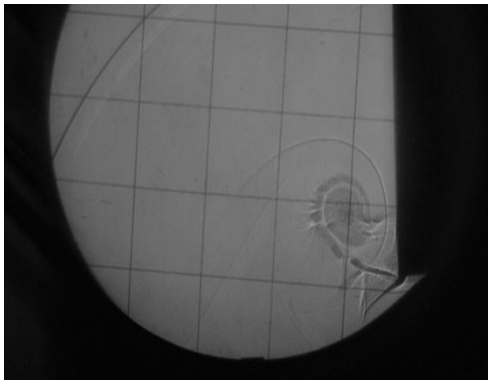

535

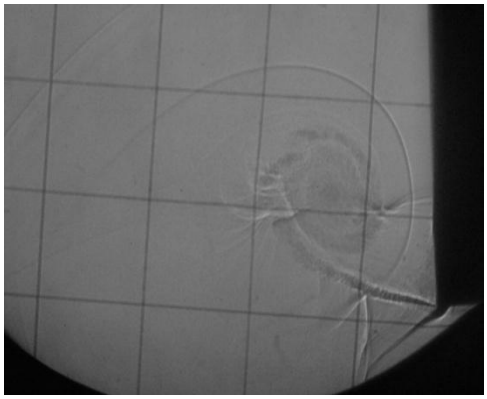

536

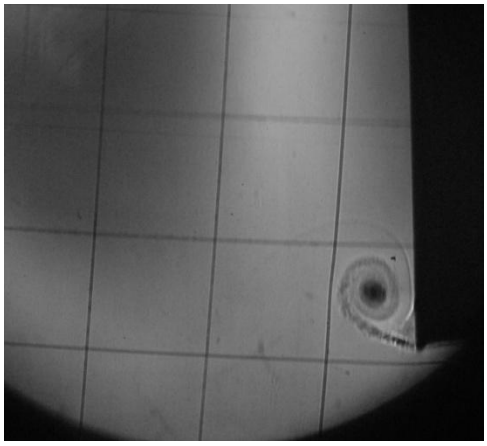

556

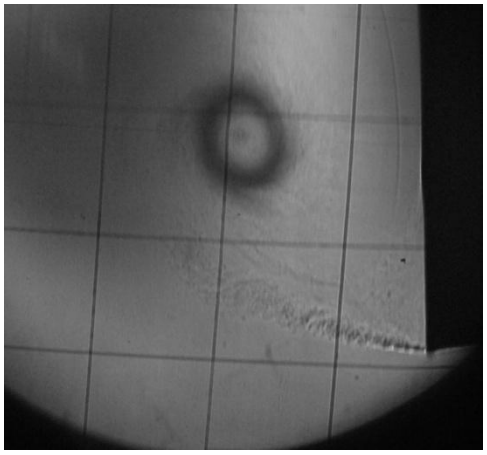

557

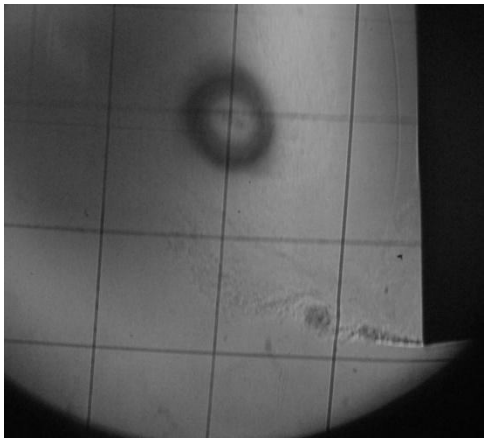

559

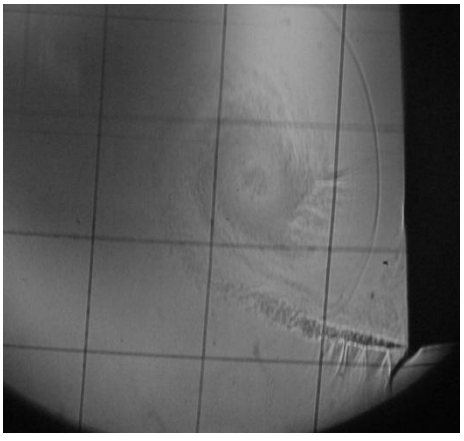

560

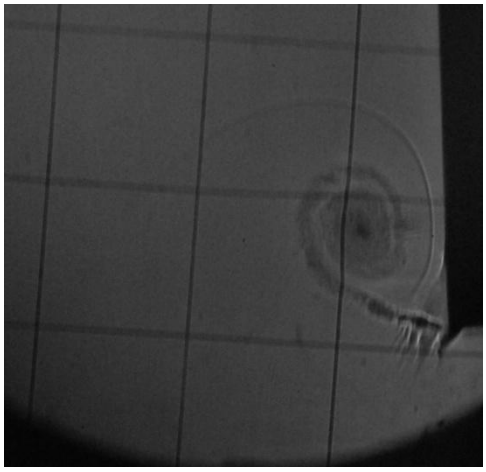

564

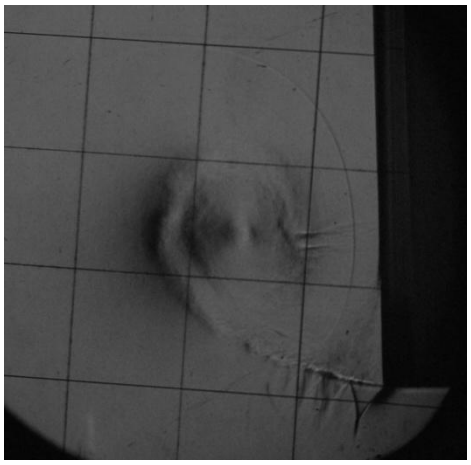

568

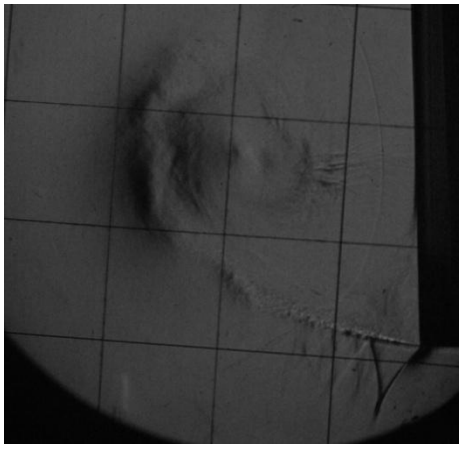

570

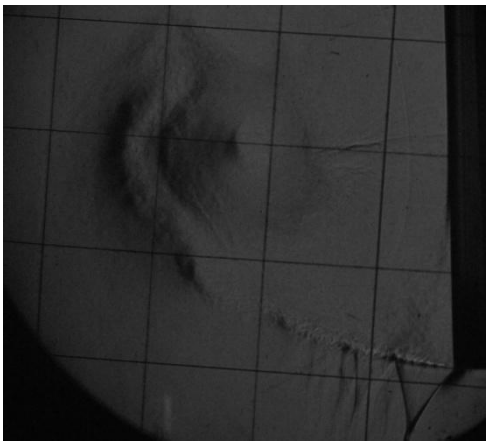

572

APPENDIX E: Experimental pictures for 200mm Diameter wall

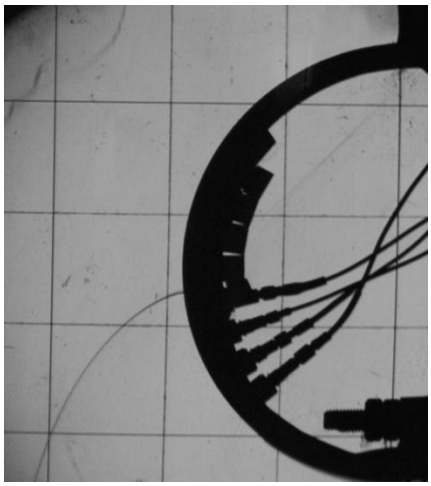

306

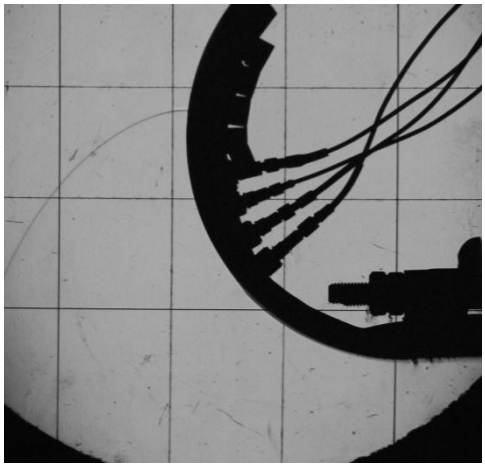

307

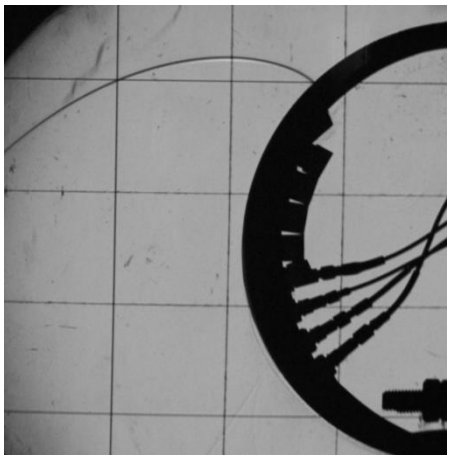

310

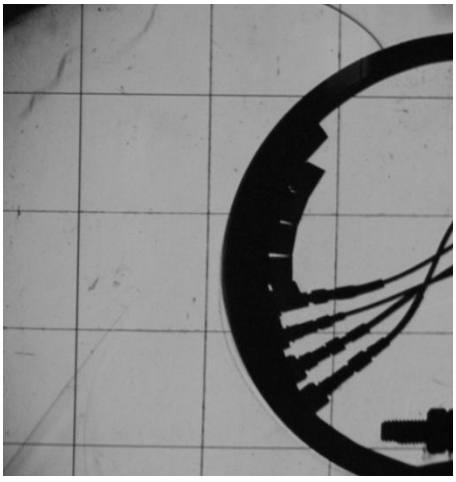

320

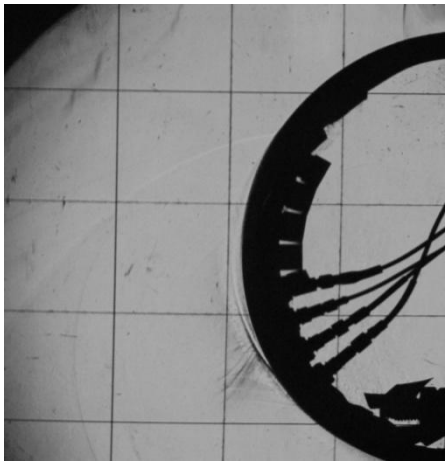

336

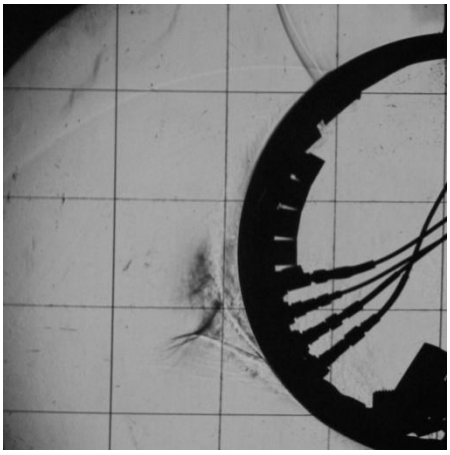

337

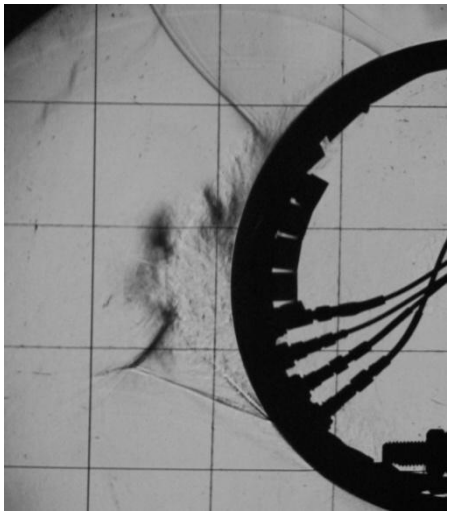

338

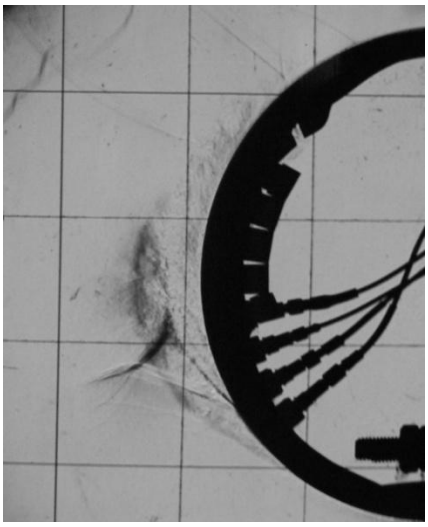

339

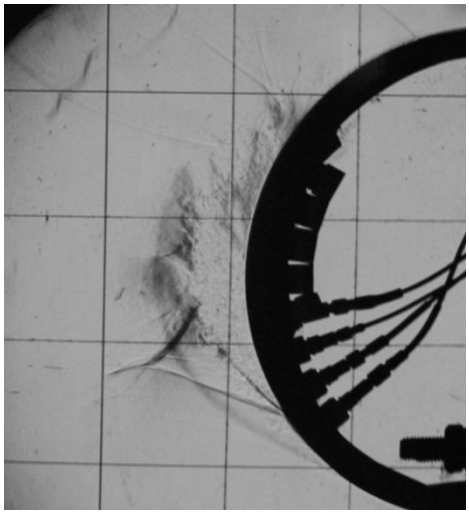

340

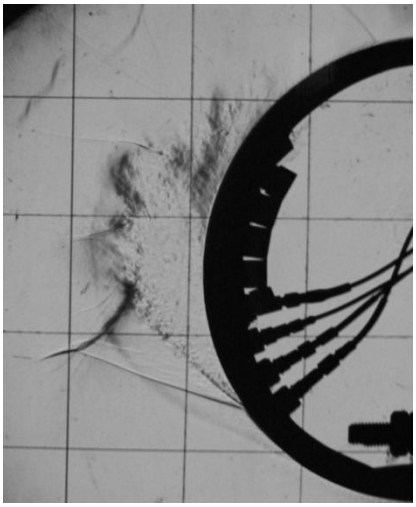

341

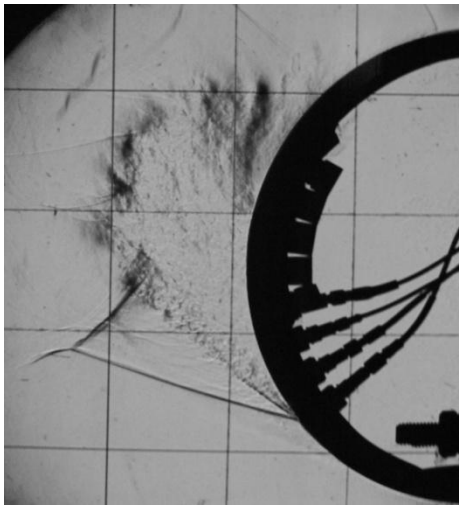

342

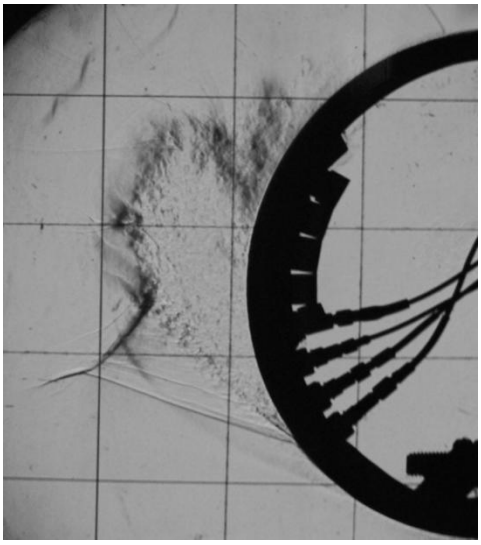

345

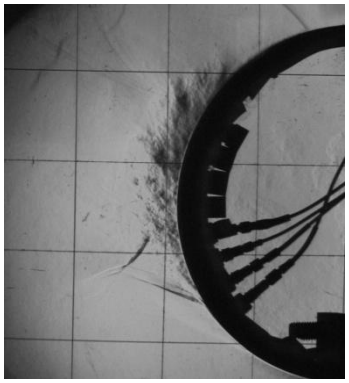

350

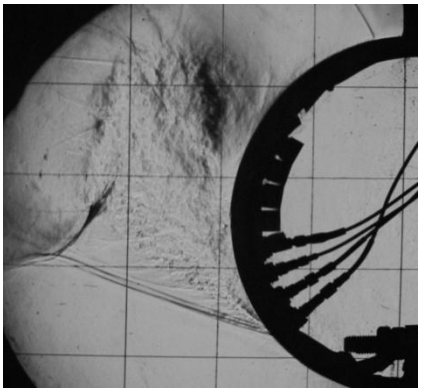

351

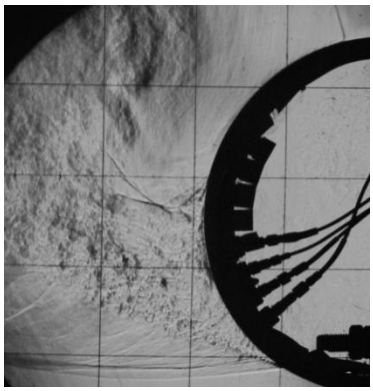

352

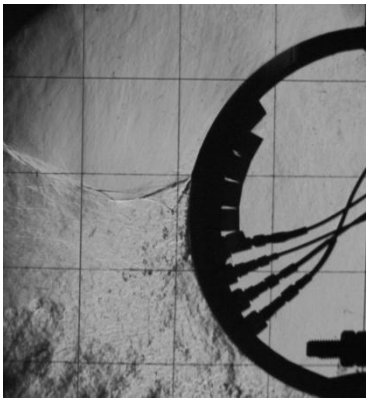

353

Experimental pictures for 400mm diameter wall

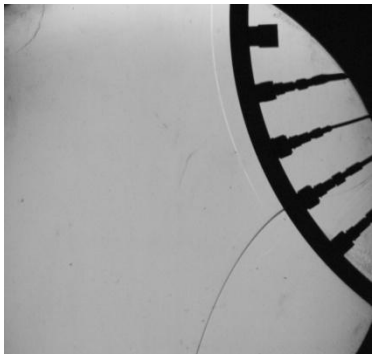

372

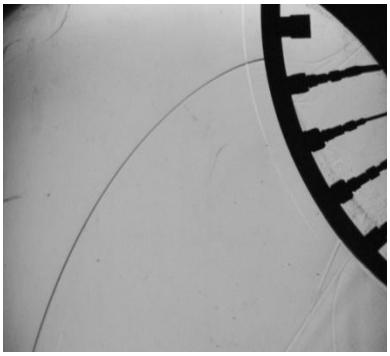

373



374

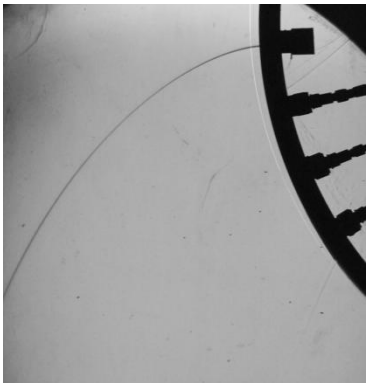

376

APPENDIX F: PRESSURE TRACE

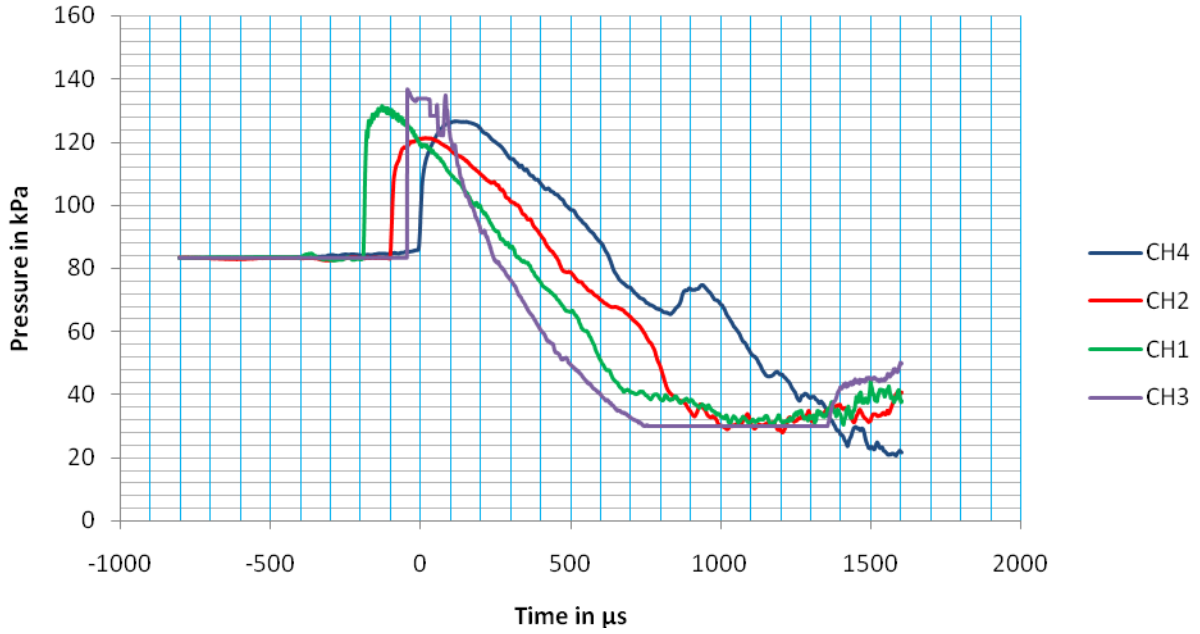

M_s = 1.49

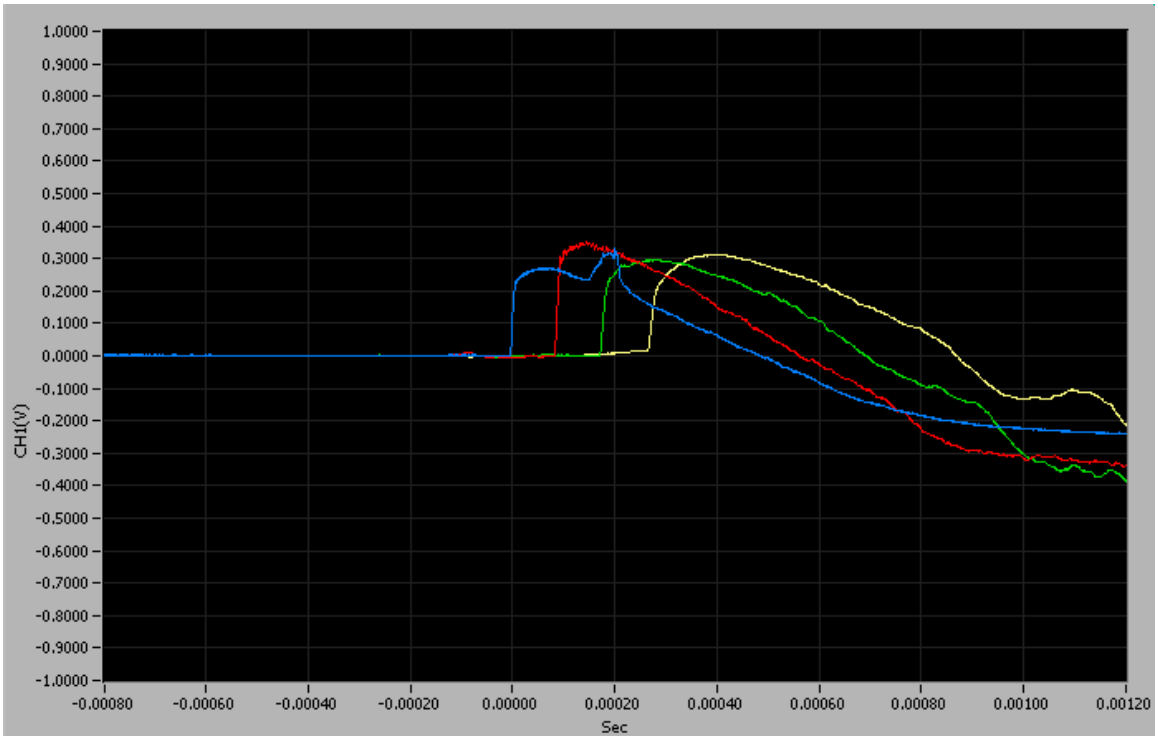

Ms = 1.51

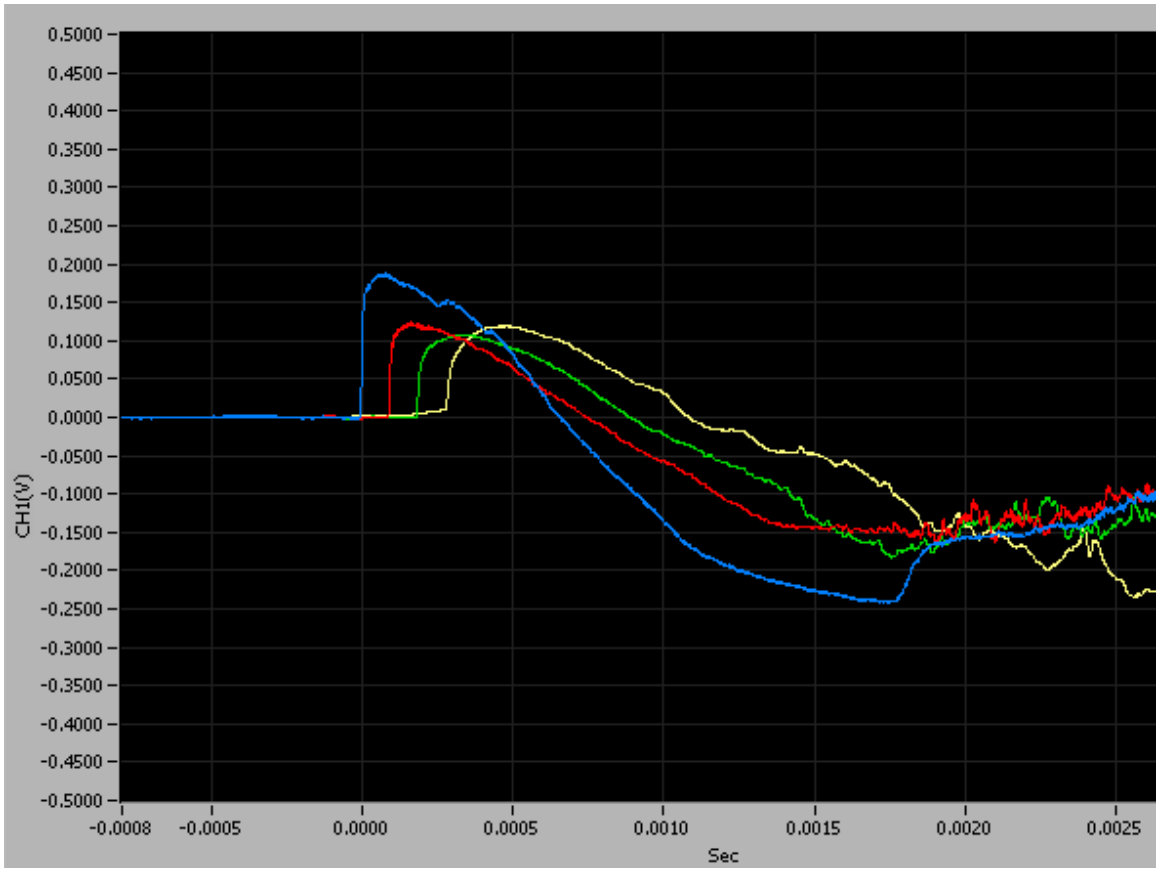
0.5000
0.4500
0.4000
0.3500
0.3000
0.2500
0.2000
0.1500
0.1000
0.0500
0.0000
-0.0500
-0.1000
-0.1500
-0.2000
-0.2500
-0.3000
-0.3500
-0.4000
-0.4500
-0.5000
CH1(V)
-0.0008
-0.0005
0.0000
0.0005
0.0010
0.0015
0.0020
0.0025
Sec

M_s = 1.44

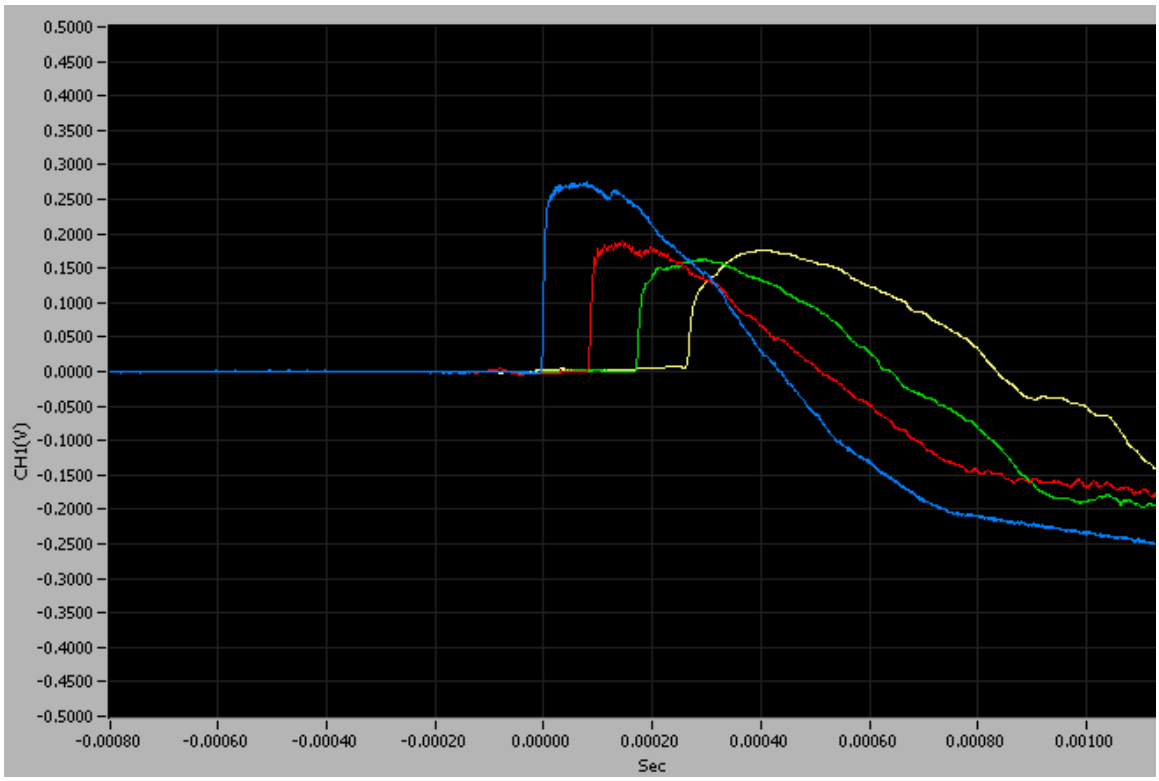
0.5000
0.4500
0.4000
0.3500
0.3000
0.2500
0.2000
0.1500
0.1000
0.0500
0.0000
-0.0500
-0.1000
-0.1500
-0.2000
-0.2500
-0.3000
-0.3500
-0.4000
-0.4500
-0.5000
CH1(V)
-0.00080
-0.00060
-0.00040
-0.00020
0.00000
0.00020
0.00040
0.00060
0.00080
0.00100
Sec

M_s = 1.57

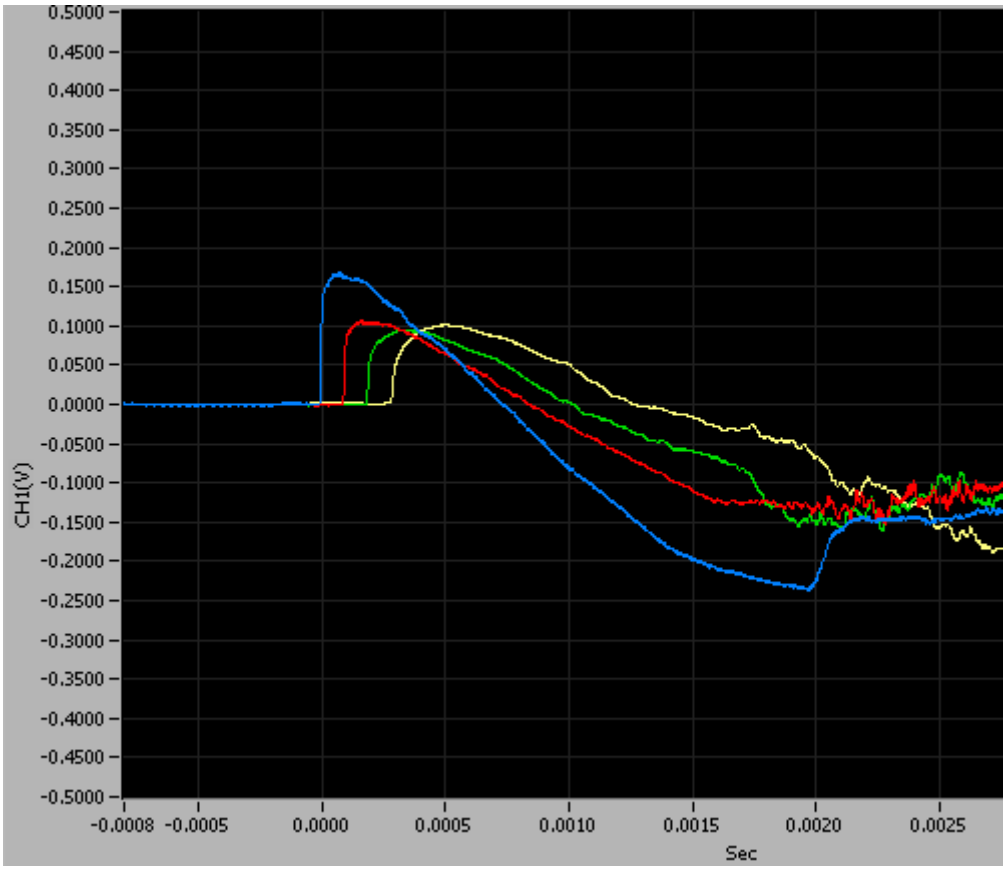
0.5000
0.4500
0.4000
0.3500
0.3000
0.2500
0.2000
0.1500
0.1000
0.0500
0.0000
-0.0500
-0.1000
-0.1500
-0.2000
-0.2500
-0.3000
-0.3500
-0.4000
-0.4500
-0.5000
CH1(V)
-0.0008
-0.0005
0.0000
0.0005
0.0010
0.0015
0.0020
0.0025
Sec

M_s = 1.35